Mineralogical study of Li pegmatite from Nagatare, Fukuoka Prefecture, Japan : microtextures formed by exsolution and hydrothermal alteration

白勢, 洋平

https://doi.org/10.15017/1654660

出版情報：九州大学, 2015, 博士（理学）, 課程博士
バージョン：

Mineralogical study of Li pegmatite from Nagatare, Fukuoka Prefecture, Japan: microtextures formed by exsolution and hydrothermal alteration

福岡県長垂 Li ペグマタイトの鉱物学的研究

-離溶反応と交代変質作用による微細組織の形成-

YOHEI SHIROSE

白勢　洋平

Department of Earth and Planetary Sciences, Kyushu University

2016 March

ABSTRACT

Pegmatites have internal zone structure, whose core to intermediate zone are enriched in rare elements such as Li, Cs, Ta, and REE. The enrichment of rare elements in core to intermediate zone is derived from a distribution of incompatible components to residual melts with flux components (London 2014). Flux rich melts develop a formation of rare elements minerals and exsolution of water fluids. The fluids make druses in pegmatite or alterations of primary minerals with internal microtextures. In pegmatite, subsolidus reactions including the hydrothermal alterations are expected; however, their process has not been obvious. In this thesis, microtextures in primary minerals from pegmatite and the altered products were investigated. The montebrasite-amblygonite series, K-feldspar, petalite, and Li tourmaline from the Nagatare Li pegmatite, Fukuoka Prefecture, Japan, had complex internal textures. The exsolution process of the montebrasite-amblygonite series and the alteration process of above minerals were mainly discussed.

The montebrasite–amblygonite series has long been known as primary phosphates occurring from Li pegmatites and topaz-bearing granites. In this thesis, the montebrasite–amblygonite series and lacroixite from the Nagatare Li pegmatite were investigated by X-ray diffraction (XRD) experiments, electron microprobe analyser (EPMA) analyses and transmission electron microscope and scanning transmission electron microscope (TEM/STEM) observations. EPMA analyses show scattered patch or lamella of lacroixite in montebrasite and amblygonite like “natromontebrasite” in all specimens. TEM/STEM observation revealed that the patch texture was composed of lacroixite and low fluorine contents montebrasite. The crystal orientations of patch and host montebrasite crystal were exactly similar, and the boundaries were well developed {110} planes. In XRD experiments at high temperature,

increasing temperature changes unit cell parameters of amblygonite, which close in value to monoclinic structure like lacroixite. These results suggest that scattered patch or lamella of lacroixite is an exsolution texture from high-temperature phase. The montebrasite and amblygonite specimens from other localities were also investigated in this thesis, and they have various textures corresponding to their occurrence. The montebrasite–amblygonite series from high temperature Li pegmatite with only petalite as Li-aluminosilicate phase had low to high lacroixite contents, and the montebrasite–amblygonite from lower temperature Li pegmatite with spodumene had no or low lacroixite contents. Gem-quality montebrasite from drusy vugs formed at low temperature had no exsolution texture or lacroixite. Investigating fine textures of the montebrasite–amblygonite series provides information of thermal changes and chemical environments at pegmatite formation.

We also investigated the alteration textures of K-feldspar, petalite, Li tourmaline, and the montebrasite-amblygonite series from the Nagatare Li pegmatite by XRD experiments, EPMA analyses, and TEM/STEM observations, and discussed the alteration processes. K-feldspar was altered to cookeite + quartz, muscovite + quartz, Li tosudite + quartz, or K beidellite + quartz. Petalite was mainly altered to beidellite or/and montmorillonite + quartz. Li tourmaline was mainly altered to muscovite. XRD experiments revealed the polytypes of muscovite after Li tourmaline to be the combinations of $2M_1$, $2M_1 + 1M$, or $2M_1 + 1M + 3T$, varied with part and specimens. The montebrasite-amblygonite series was partially altered to various phosphates and muscovite. The chemical compositions of beidellite-montmorillonite were plotted in the smectite group occurred from bentonite of acidic precursors. With decreasing temperature, Li chloritization, sericitization, and smectitization had occurred in the Li rich part of the Nagatare Li pegmatite. In weakly acidic condition, K-feldspar had breakdown, forming cookeite + quartz with releasing K^+ to a hydrothermal fluid. As a result of the change from

weakly acidic to neutral condition, Li tourmaline had breakdown, and suffered sericitization. It is estimated that Li and B escaped from pegmatite body with reaction fluids at last, while a part of released Li was precipitated as lithiophorite on the surface of pegmatite minerals. In Li pegmatites, residual fluids containing Li react with primary minerals in subsolidus conditions, and they make cation exchanges between fluids and solids. The changes of fluid compositions with non-equilibrium reactions and a decrease of temperature controlled hydrothermal alterations. Li pegmatites with no druse as the Nagatare Li pegmatite have similarity of clay minerals to Li pegmatites with druse except for alteration of primary minerals.

CONTENTS

1 INTRODUCTION

1.1 Pegmatite and the mineralogy

Pegmatite is igneous rock composed of coarse grained minerals and generally associated with granites, whose texture and composition are fractionated from normal igneous rocks. Though the majority of pegmatites have similar chemical composition as granite, some pegmatites contain abundant rare elements minerals. In particular, Li pegmatite is characterized by containing rare elements such as Li, Cs, and Ta (e.g., Černý & Ercit 2005). For internal zonation of pegmatite, they are represented as border zone, wall zone, intermediate zone, and core by mineral paragenesis and internal textures (Fig. 1). Border zone and wall zone are mainly composed of feldspar and quartz with minor mica similar as granite. The border zone corresponds to a chilled margin, while the bulk composition is not represented in. The wall zone often has graphic texture, which is evidence of undercooling condition with high viscosity of melt (e.g., London 2008). The minerals containing rare elements ordinarily occur from intermediate zone to core, represented by lepidolite, Li tourmaline, spodumene, petalite, and the montebrasite-amblygonite series.

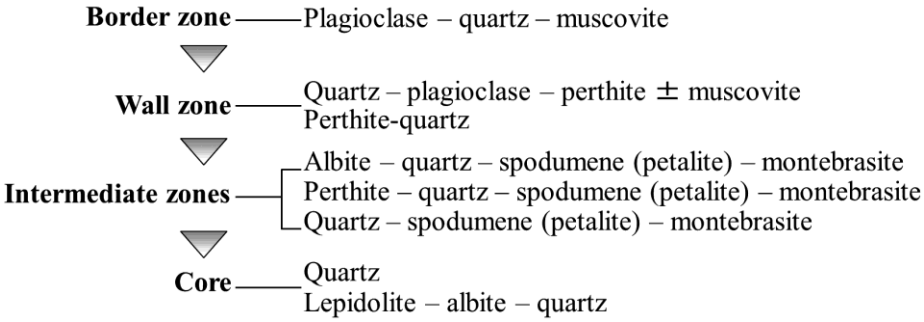

Fig. 1 General sequence of pegmatite zone and the component minerals in Li pegmatite (*e.g.*, Cameron *et al*. 1949, Norton 1983). From outer to inner zone of the pegmatite body, they are represented as border zone, wall zone, intermediate zones, and core. Large single crystals with uniorientation occur in wall zone and intermediate zone.

These textures are observed in Li pegmatite regardless of their scale of rock bodies, while the distribution of internal zone is more complex for large pegmatite body (Figs. 2, 3). In addition to symmetry zonation of upper and foot zone, the vein has asymmetry features such as aplite and additional zonation derived from a gravity (Fig. 2). Large pegmatite bodies often intrude to host rock such as metamorphic rock, and elongate in meter to kilometer (Fig. 3). They sometimes lack the original pluton on surface of the ground.

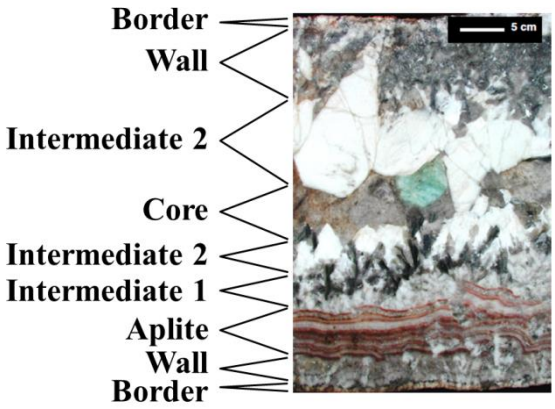

Fig. 2 Pegmatite section and the zoning texture, showing zone texture in pegmatite dyke, located near Palomar Mountain, San Diego County, California, U.S.A. (modified after London 2008, 2014). Beryl occurs as rare elements mineral in core.

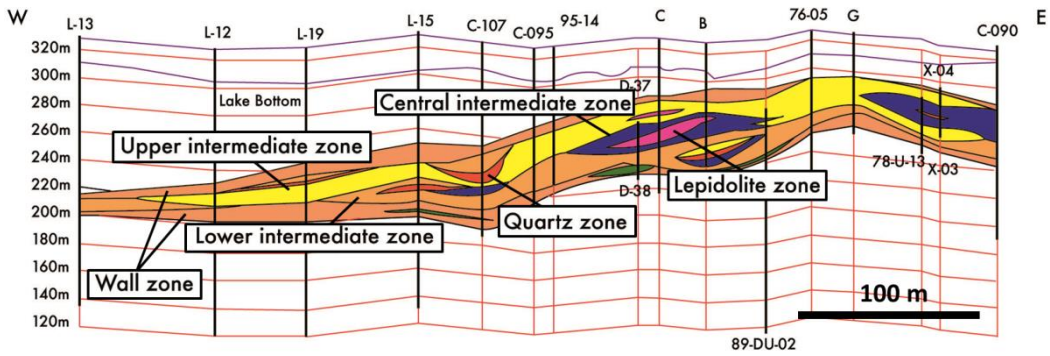

Fig. 3 Cross section of Tanco pegmatite (modified after London 2008, Stilling *et al*. 2006). Tanco pegmatite, Manitoba, Canada, is one of huge pegmatite bodies, and notable as rare elements mine.

1.2 Pegmatite formation processes

Traditional models to explain internal evolution of pegmatite are that the formation of zone texture and enrichment of rare elements derive from magmatic crystal fractionation and redistribution of elements by water fluids (e.g., Cameron *et al*. 1949, Jahns & Burnham 1969). They are based on abundant field description of pegmatites and synthesis experimental studies. In their models, incompatible elements and volatile components are distributed to melt, and this hydrosilicate melt crystalizes at the last stage of pegmatite formation (Fig. 4). Therefore, the minerals enriched in incompatible elements, Li, Be, Cs, Nb, and Ta occur from intermediate zone and core.

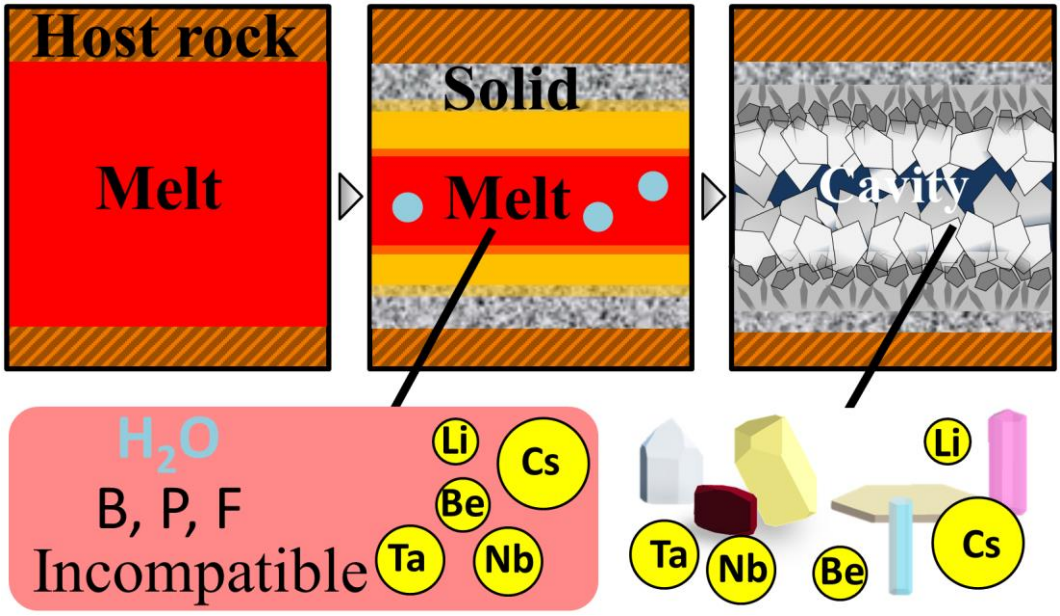

Fig. 4 Traditional Li pegmatite formation model, showing enrichment of incompatible components in melt and formation of rare element rich part with cavity (*e.g.*, Cameron *et al*. 1949, Jahns & Burnham 1969).

In recent model, their concepts are developed, and flux rich boundary layer has important role for giant crystal formation and rare elements enrichment in pegmatite (London 2008, 2014). In this case, "flux" means that components decrease liquidus temperature and viscosity of silicate melt, which simultaneously increase the solubility of incompatible elements. When pegmatite melts crystalize and develop crystal front, fluxed boundary layer, composed of flux and rare elements rich melts, is formed between crystal front and bulk melt in the model (Fig. 5). Fluxed boundary layer encourages a formation of pure and big silicate crystals and enrichment of rare elements in melt. At last, flux rich melt exists in the core, and the stage transits from magmatic to hydrothermal stage. When incompatible elements and flux components reach the saturation, flux rich melts develop a formation of rare elements minerals and exsolution of water fluids. In the result, the fluids form cavities or clay filled cavities (Foord *et al.* 1986). London (2014) suggested that "dry" (open-space) cavities were originally filled by dense clays than water fluids, final products after the flux-rich hydrosilicate liquids. In the other

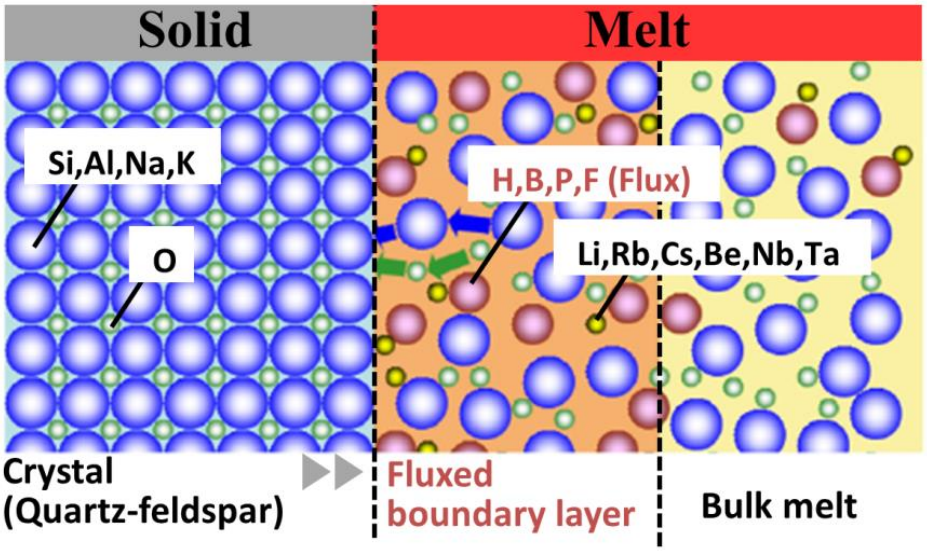

Fig. 5 Fluxed boundary model (modified after London 2008, 2014). Fluxed layer exists in the boundary of crystal front and silicate melt, enriched in rare elements.

case, occurrences of hydrothermal alteration with primary minerals replacement are expected as the result of the exsolution of water fluids. Primary Li-aluminosilicates, such as spodumene and petalite, are often altered to fine grained eucryptite, albite, and muscovite, caused by hydrothermal alterations at a late stage of Li pegmatite forming process (*e.g.*, London & Burt 1982). These subsolidus reactions, including hydrothermal alteration, exsolution, and diffusion, are inseparable process of pegmatite formation.

1.3 Purpose of this study

In pegmatite, subsolidus reactions are expected; however, their process has not been obvious. For example, an alteration of pink Li tourmaline, generally occurring from Li pegmatites, has not been studied in detail. In addition, the description of clay minerals, occurred as final products in pegmatite, is insufficient. Subsolidus reactions, including hydrothermal alteration, exsolution, and diffusion, are reflected to complex microtextures in minerals. In this study, the purpose is to clarify the stability of primary minerals and the behavior of elements and residual fluids in pegmatite, investigating the detailed process of subsolidus reactions. A transmission electron microscope (TEM) is effective for analyzing these microtextures derived from subsolidus reactions. Two main topics of microtextures in pegmatite mineral were discussed in this thesis.

Firstly, the microtexture of the montebrasite–amblygonite series with lacroixite from an Li pegmatite in Nagatare, Fukuoka Prefecture, Japan, was investigated (Section 5). It was examined with X-ray powder diffraction (XRD) experiments at room temperature and high temperatures, electron microprobe analyser (EPMA) analyses and TEM observations. We describe the crystallographic relationship between the montebrasite–amblygonite series and lacroixite, and discuss the formation processes of their intergrowth textures. Furthermore, we compared their paragenesis and textures with the specimens from other pegmatites formed in different conditions, showing their relationships and environmental restrictions.

Secondary, hydrothermal alterations in the Nagatare Li pegmatite were investigated (Section 6). Primary K-feldspar, petalite, Li tourmaline, and the montebrasite–amblygonite series with various alteration grades from the Nagatare Li pegmatite were examined by XRD experiments, EPMA analyses and TEM observations. The microtextures derived from

hydrothermal alteration in Li pegmatite were observed in these minerals, and their forming processes with hydrothermal fluids were discussed.

2 GEOLOGICAL BACKGROUND

2.1 Li pegmatite distributions in Japan

In Japan arc, abundant granitic rocks are distributed, and they are divided to inner zone of Southwest Japan, outer zone of Southwest Japan and Northeast Japan (Fig. 6). Inner zone of Southwest Japan is formed in late Cretaceous, whose North part is composed of magnetite series granites and South part are composed of ilmenite series granites (Ishihara, 1977). The Nagatare pegmatite and the Myokenzan pegmatite are well known as large Li pegmatite body in Japan, which have various Li minerals. The Li pegmatites distributed in Cretaceous granites have vein textures, while Li pegmatites formed with Tertiary granites in outer zone of Southwest Japan are miarolitic type pegmatite. They have younger formation age than other famous Li pegmatite such as the Tanco pegmatite, Canada. In this study, the mineralogy of the Nagatare pegmatite was mainly investigated, while the montebrasite-amblygonite series from the Myokenzan pegmatite and famous pegmatites such as the Tanco pegmatite, Minas Gerais, the Havey pegmatite, the Varuträsk pegmatite were also investigated.

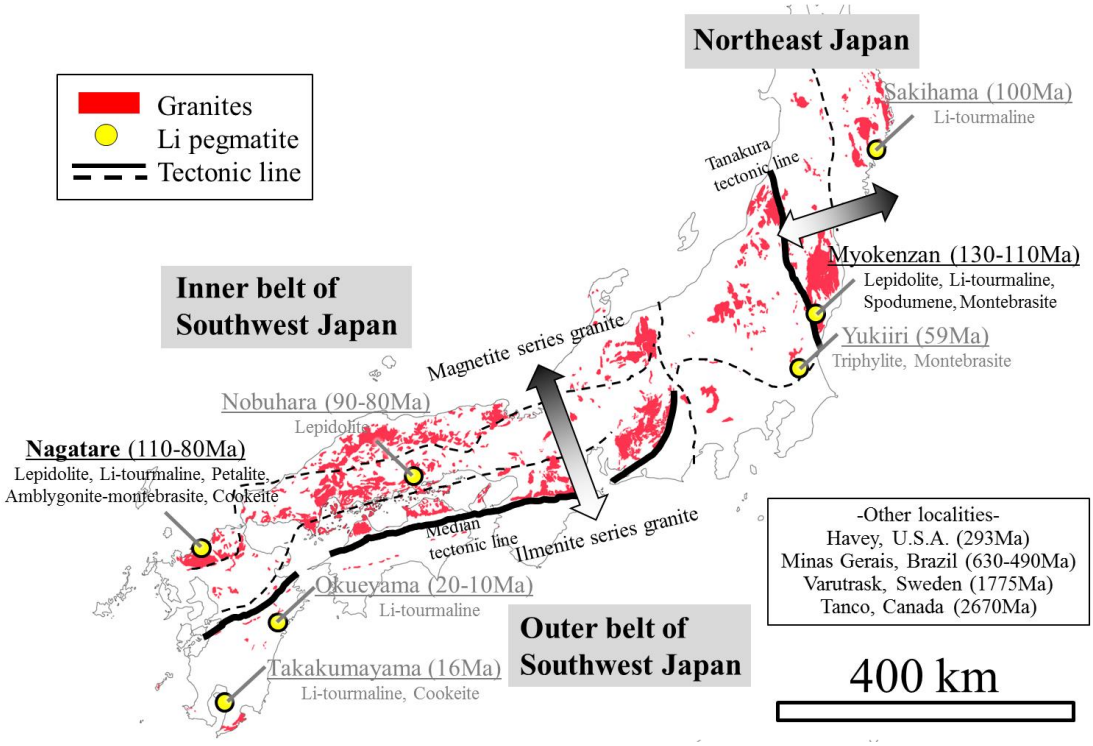

Fig. 6 Distribution map of Li pegmatite and granite in Japan. The distribution of granitic rocks was modified after radiometric age map (Geological survey of Japan 1977). (Ishihara 1977, Nagashima & Nagashima 1960, Matsuyama & Kobayashi 1995, Shirose & Uehara 2012, Matsubara & Kato 1980).

2.2 Geological background of the Nagatare pegmatite

In North part of Kyushu region, Japan, Cretaceous granitoids are widely exposed, intruding into Sangun metamorphic rocks. They are divided into tonalite-granodiorite series and granite series, and finely divided into 15 types (*e.g.*, Karakida 1985). The Sangun metamorphic rocks were formed under high-pressure and low-temperature conditions in the Late Paleozoic to Early Mesozoic, and divided into Renge Belt and Suo Belt (Nishimura 1998). The Nagatare pegmatite is located at Nagatare, in the western area of Fukuoka City, Fukuoka Prefecture (Fig. 7). The pegmatite is derived from the Sawara granite (100–80 Ma) that intruded into the Itoshima granodiorite (115–70 Ma) (Karakida *et al*. 1994) (Fig. 8). The pegmatite also intruded into the Sangun metamorphic rocks. There are outcrops of barren pegmatite and beryl-containing pegmatite found from the coast to Mt. Nagatare. Li mineral deficient pegmatites often occurred with aplites, with a dyke-shape body, 5-20 m in width and elongating along N20ºW, which is concordant with lamination structures of Sawara granite. There are differences for each dyke on constituent minerals and internal textures. Li enriched pegmatite is only one dyke located in Mt. Nagatare, and many of the dykes are simple pegmatites, bearing a common granite composition. The Li-enriched pegmatite of Mt. Nagatare was mined for Li ore in the middle of the 20th century. The ore body contained rare element minerals such as lepidolite (polylithionite–trilithionite), Li tourmaline, petalite, montebrasite, amblygonite, and pollucite. The descriptive mineralogical studies were reported before closing the mine (*e.g.*, Koh 1933, Takimoro 1937, Okamoto 1944), and the occurrences of rare element minerals were also reported after closing the mine (*e.g.*, Sakurai *et al*. 1972, Sakurai *et al*. 1973, Banno *et al*. 2001). We have been reinvestigating the minerals of the Nagatare pegmatite including lepidolite (Kataoka & Uehara 2000), tourmaline (Shirose & Uehara 2013), the montebrasite–amblygonite series (Shirose &

Uehara 2014) and other rare minerals, such as Bi minerals (Uehara & Shirose, 2013). In this study, specimens collected from this Li ore body were mainly used, and specimens from other localities were also analysed for the montebrasite-amblygonite series.

The Li pegmatite body was classified to several zones by mineral paragenesis and inner texture. K-feldspar, petalite, Li tourmaline, and the montebrasite-amblygonite series from intermediate zone to core corresponding to Li rich part have complex inner texture in their crystals.

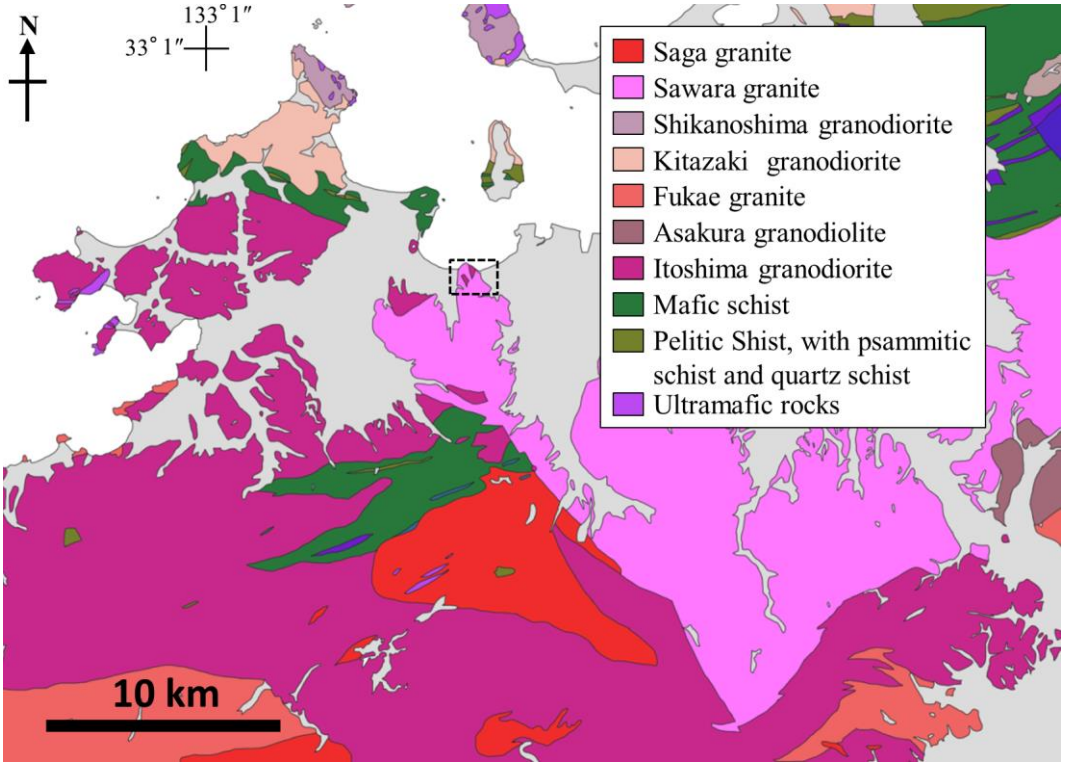

Fig. 7 Geological map of Fukuoka area for plutonic rocks and metamorphic rocks, modified after 1: 200,000 geological map Fukuoka (Kubo *et al.* 1993). Dashed box shows the Nagatare pegmatite area of Figure 8.

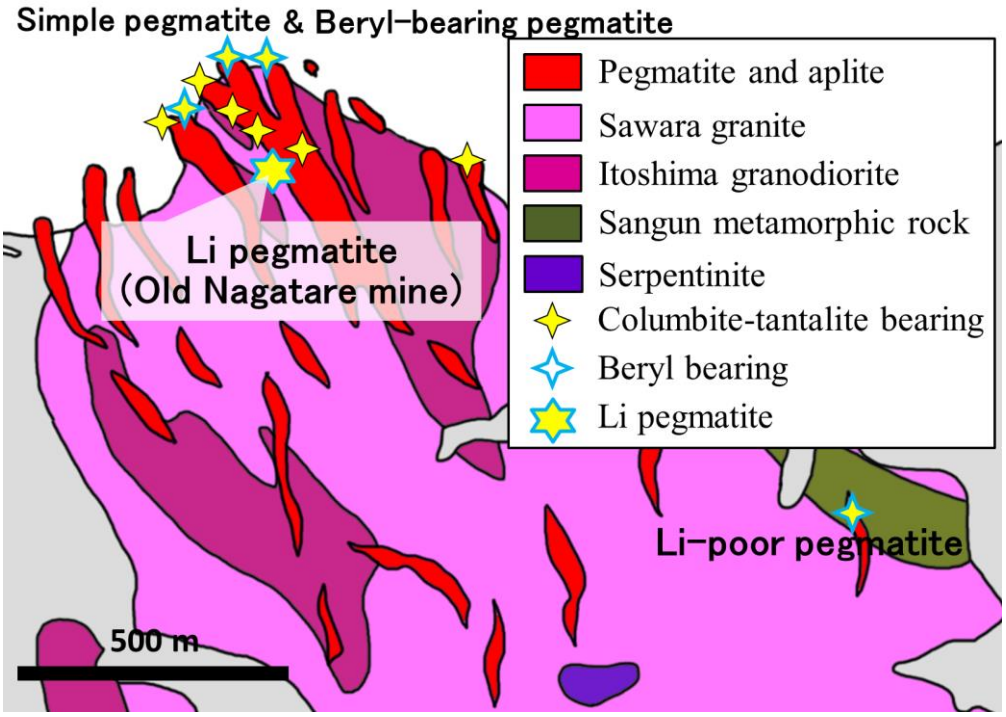

Fig. 8 Geological map around the Nagatare pegmatite (modified after Takimoto 1937 and Karakida *et al.* 1994). Light blue lined stars show beryl bearing pegmatite.

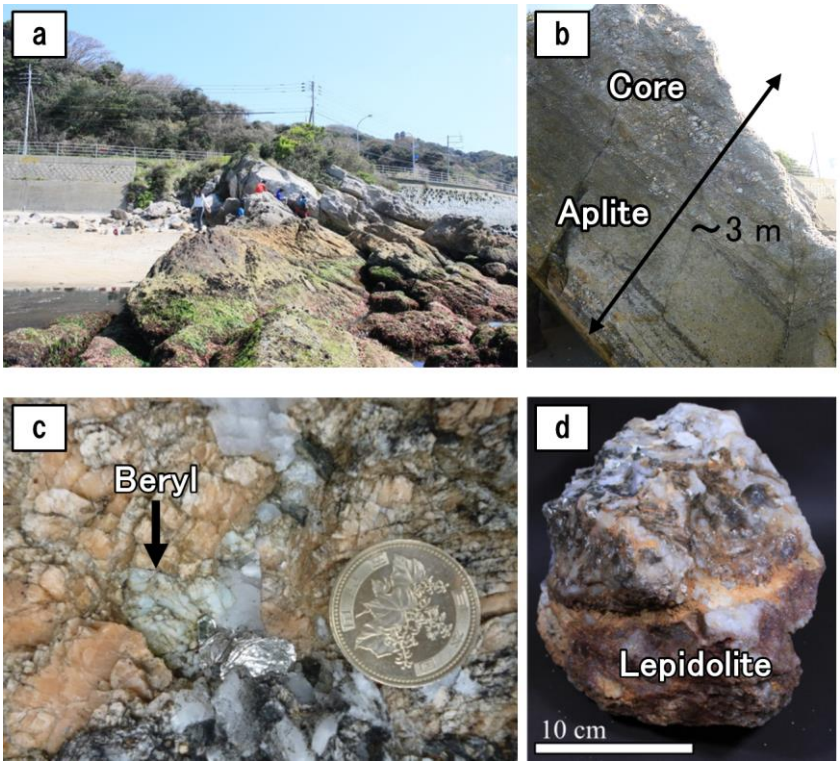

Fig. 9 Photographs of the Nagatare pegmatite. (a) The view from coast to Mt. Nagatare and pegmatite dyke, 10 m in width and elongating along N20ºW. (b) The texture of pegmatite dyke in Figure 9a. (c) Beryl occurrence in pegmatite dyke. (d) Li rich ore from Li rich part in the Nagatare pegmatite.

3 ANALYTICAL METHODS

Powder XRD data at room temperature were collected using a Bruker AXS M18XHF22-SRA diffractometer utilizing monochromatized Cu*K*α radiation generated at 40 kV and 50 mA. For clay minerals, powder XRD patterns were also obtained from samples oriented after elutriation and treated with ethylene glycol. Fluorine contents for the montebrasite–amblygonite series were estimated from bulk powder XRD patterns for all specimens using Kallio's method (1978). The XRD patterns of the montebrasite-amblygonite series from 50 to 700 ºC were performed by a RIGAKU Ultima IV diffractometer with measurements *in situ*. XRD data of fine part were collected on crystal fragments using a Rigaku RINT RAPID II curved imaging plate microdiffractometer that used monochromatized Cu*K*α radiation generated at 40 kV and 30 mA. The fragments were randomized using a Gandolfi–like motion about two axes (oscillation on ω and rotation on φ), and the polytypes of clay minerals were determined.

Chemical analyses were performed on a JEOL JXA8530F EPMA equipped with a wavelength dispersive X-ray spectrometer (WDS) for carbon coated thin sections. The standard materials were fluorphlogopite (for F*K*α), albite (for Na*K*α), olivine (for Mg*K*α), spodumene (for Al*K*α), diopside (for Si*K*α and Ca*K*α), $KTiOPO_4$ (for K*K*α and P*K*α), diopside (Ca*K*α), rhodonite (for Mn*K*α), and almandine (for Fe*K*α). Quantitative analyses for the montebrasite-amblygonite series were performed at an accelerating voltage of 15 kV, beam current of 2 nA, and probe diameter of 15 μm, and that for clays were at an accelerating voltage of 15 kV, beam current of 6 nA, and probe diameter of 10 μm. The ZAF method was used for data correction. Chemical analyses and morphological observations were also investigated by JEOL JSM5800LV scanning electron microscope (SEM) and JEOL JSM-7001 FE-SEM.

For TEM samples, the thin sections of specimens on the single hole sheet mesh were

ion-milled with Ar^+ ions by GATAN PIPS model 691 and FISCHIONE TEM MILL model 1050 ion milling apparatus. An FEI Quanta 200 3D focused ion beam (FIB) with micro-sampling system was also used, and the ion milling apparatus was performed for polishing the surface. Transmission electron microscope and scanning transmission electron microscope (TEM/STEM) observations of the specimens were carried out with a JEOL JEM-ARM200F scanning/transmission electron microscopy with spherical aberration corrector at 200 kV. X-ray mapping images and chemical analyses were taken by a JEOL JED-2300T energy dispersive X-ray spectrometer with 100 mm^2 silicon drift detector. A thin-film approximation method was used for the measurements of elements. These apparatuses are installed at the Ultramicroscopy Research Center in Kyushu University.

4 MINERALOGICAL ASSOCIATIONS OF THE NAGATARE PEGMATITE

The simple pegmatites in Nagatare are mainly consisted of quartz, K-feldspar, albite and muscovite, showing simple pegmatite compositions close to the chemical composition of granite. However, some pegmatites contain rare elements minerals such as beryl and columbite, indicating the concentration of rare elements including Be, Nb, and Ta. In addition, they often contain spessartine-almandine garnet and gahnite, generally occurring in a peraluminous granite melts. Spessartine-almandine garnet and beryl also occur from a pegmatite dyke intruding metamorphic rocks, and tourmaline is contained as accessary mineral in the pegmatite dyke. The pegmatite dyke intruding metamorphic rocks is chemically fractionated from other simple pegmatite dykes.

A chemically and structurally most fractionated pegmatite in Nagatare is emplaced as large pegmatite dyke in Mt. Nagatare, which was mined for Li ore as already mentioned in Section 2. The representative mineral paragenesis of Li pegmatite is shown in Figure 10. The mineral association of border to wall zone is similar to simple pegmatite, mainly composed of quartz, K-feldspar, albite, and muscovite with beryl, columbite, garnet, and gahnite. For intermediate zone of Li pegmatite, in addition to the minerals above, there are Fe-bearing Li tourmaline, white lepidolite, and triplite, which indicate depletion of mafic components and enrichment of rare elements and flux components. Li-rich part of Li pegmatite as intermediate zone to core has Li tourmaline, lepidolite, the montebrasite-amblygonite series, petalite, and pollucite, containing no mafic minerals such as garnet, gahnite, triplite and Fe tourmaline. In core to intermediate zone, mineral assemblage of lepidolite, albite, and quartz fills some parts and replaces primary minerals such as K-feldspar. A formation of this assemblage indicates a transition from magmatic to hydrothermal stage.

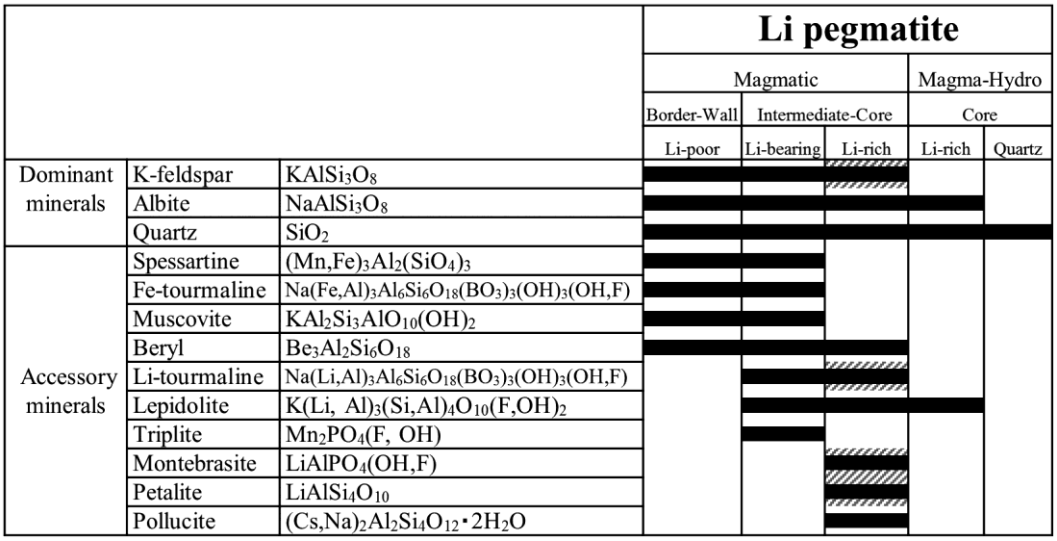

Fig. 10 Representative mineral paragenesis of the Nagatare Li pegmatite, and the zone sequence related to formation environment. Grey slashed areas show alteration of primary minerals.

Various chemical trends shown in such as tourmaline solid solutions give an information of their environmental conditions. As for chemical compositions of tourmaline from the Nagatare pegmatite, Fe and Mg were dominant with low F contents in the tourmaline from the pegmatite intruding metamorphic rocks, while the tourmaline from Li pegmatite show fractionated trends from Fe-Li to Li-Al dominant chemical compositions with F enrichment (Shirose & Uehara 2013). F contents of the montebrasite-amblygonite series from the Nagatare Li pegmatite show a high F concentration at the central part of Li pegmatite, 1.4-2.0 wt% F contents, using the partition coefficient to melt estimated by London *et al*. (2001). Columbite group minerals [$(Fe,Mn)(Nb,Ta)_2O_6$] are common accessary minerals in the Nagatare pegmatite, and chemical trends of columbite group minerals are related to F contents of melt (Wise *et al*. 2012). In the Nagatare pegmatite, the chemical trends are Mn/(Mn+Fe) = 0.3-0.6 with Nb enrichment in the simple pegmatites, and Mn/(Mn+Fe) = 0.4-1.0 with Nb to Ta enrichment on Mn endmember in the Li pegmatite (Shirose *et al*. 2015). Their chemical trends coincide with that of columbite group minerals reported by Wise *et al.* (2012). The fluorine enrichment in the

Li pegmatite, confirmed in these trends and occurrence of abundant lepidolite, also affects a late hydrothermal alteration stage. A formation of fluorine rich minerals such as topaz and fluorapatite as alteration products show that the fluorine enrichment is retained in the hydrothermal alteration stage.

It is notable that complex internal textures are confirmed in primary minerals such as K-feldspar, Li tourmaline, the montebrasite-amblygonite series, and petalite in the Li pegmatite from Nagatare. They have undergone alteration to clay minerals such as mica. The montebrasite-amblygonite series is altered into various secondary phosphates and muscovite (Shirose & Uehara 2014). These reactions are hydrothermal replacement caused by H_2O rich residual fluids in the late stages of pegmatite forming process, and that is suggested as a characteristic reaction in Li pegmatites with abundant H_2O. In addition to the alteration textures, exsolution texture of the montebrasite-amblygonite series and lacroixite was described in this study.

5 EXSOLUTION TEXTURES OF THE MONTEBRASITE-AMBLYGONITE SERIES

5.1 The montebrasite-amblygonite series

The montebrasite–amblygonite series have long been known as primary phosphates occurring from Li pegmatites and topaz-bearing granites. The chemical compositions are shown as solid solution of $LiAlPO_4(OH)$–$LiAlPO_4F$ with triclinic ($C\bar{1}$). The changes of mineralogical properties corresponding to the value of F/(F+OH) have been studied; indirectly quantitative determinations of F/(F+OH) also have been approached by mineralogical properties, such as optical properties, X-ray diffraction patterns, unit cell parameters and Raman spectra and so on (*e.g.*, Černá *et al*. 1973, Kallio 1978, Greiner & Bloss 1987, Groat *et al*. 1990, 2003, Rondeau *et al*. 2006). Despite a complete solid solution, amblygonite end member has not been reported, and the montebrasite–amblygonite series from pegmatites generally contains the middle amount of fluorine. This is restricted by the fluorine contents of pegmatite forming melts, according to the partitioning of between the montebrasite–amblygonite series and melt (London *et al*. 2001).

Hydrothermal alteration of the primary montebrasite–amblygonite series to various secondary phosphates during the late stages of pegmatite formation has been reported (*e.g.*, London & Burt 1982, Baldwin *et al*. 2000, Galliski *et al*. 2012, Shirose & Uehara 2014). London & Burt (1982) indicated that even secondary montebrasite was produced along the fractures and cleavages in primary montebrasite. Secondary montebrasite has lower fluorine contents and higher interference-color under the polarized microscope than primary montebrasite.

The montebrasite–amblygonite series often has fine textures with lacroixite, $NaAlPO_4F$ with monoclinic ($C2/c$). The species reported as “natromontebrasite”,

(Na,Li)$AlPO_4$(OH,F), was discredited, and indicated that it was mixture with lacroixite (Fransolet 1989, Fransolet *et al*. 2007). The crystal structure of the montebrasite–amblygonite series was refined using *C*-centered cell by Groat *et al*. (1990), and the pseudomonoclinic structure is topologically identical to the monoclinic structure of titanite group minerals involving lacroixite. They have also pointed out that the montebrasite–amblygonite series could not be substituted by Na or Ca due to the crystal restriction. In many cases, the montebrasite–amblygonite series crystals contain Na components in the form of the fine lacroixite intergrowth. However, the formation process of the montebrasite–amblygonite series with patchy lacroixite is not clear. Though there are possibilities of exsolution or hydrothermal alteration textures, more detailed studies are required for crystallographic and high temperature phase relations of the montebrasite–amblygonite series and lacroixite.

In this study, the montebrasite–amblygonite series with lacroixite from a Li pegmatite in Nagatare, Fukuoka Prefecture, Japan, were examined with X-ray powder diffraction experiments at room temperature and high temperatures, electron microprobe analyses and transmission electron microscope observations. We describe the crystallographic relationship between the montebrasite–amblygonite series and lacroixite, and discuss the formation processes of their intergrowth textures. Furthermore, we compared their occurrences and textures with the specimens from other localities.

5.2 Mineralogical properties of the montebrasite-amblygonite series from the Nagatare pegmatite

Eleven specimens of the montebrasite–amblygonite series used in this study were collected from this old ore deposit (Table 1). The sample numbers are listed with the analysis results in Table 1. The montebrasite and amblygonite from the Nagatare pegmatite occur as large subhedral to euhedral crystals with lepidolite, Li tourmaline and petalite in quartz, and albite (Figs. 11a, b, c). Small dendritic crystals of montebrasite are contained within K-feldspar (Fig. 11d). The crystals are colorless, milky–white color, or light–salmon color, and have a vitreous luster. There are white veins parallel to cleavage planes in the cross sections. Under the polarizing microscope, montebrasite and amblygonite were mostly cloudy caused by very fine inclusions, and polysynthetic twins were observed (Figs. 11e, f). Manganotantalite, microlite, and minor bismuth were also observed as inclusions within montebrasite and amblygonite. In addition, specimens for comparison from other localities, five localities including 8 specimens, are also listed with the analysis results in Table 1.

Table 1. Specimen list with associated minerals and mineralogical properties of montebrasite and amblygonite (Shirose & Uehara, in press).

Sample no.	Size (cm)	Form	Color	Associated minerals*	F contents (*apfu*)			Lacroixite contents (wt%)
					XRD**	EPMA		
						Av.	Range	
Nagatare pegmatite, Japan								
XN162	6	Block	LS-CL-MW	Qtz, Lpd, Ab	0.58	0.38	0.26-0.51	5.8 (7)
XN165	2	Block	LS-MW	Ab, Qtz	0.55	0.23	0.08-0.42	2.7 (5)
XN163	4	Block	CL-LS-MW	Qtz	0.54	0.47	0.39-0.50	4.8 (5)
XN160	4	Block	CL-MW	(Qtz, Lpd, Ab)	0.53	0.50	0.46-0.56	4.8 (11)
XN168	0.5	Dendritic	LS-CL-MW	Kfs, Qtz, Lpd, Ab, (Tur	0.49	0.34	0.20-0.40	2.2 (3)
XN167	0.3	Block	CL-MW	Qtz, Lpd, Ab, Kfs, Tur	0.47	0.42	0.28-0.52	1.9 (2)
Ng104	0.5	Dendritic	CL-MW	Kfs, Qtz, Lpd, (Ab, Tur	0.47	0.40	0.32-0.45	0.3 (2)
XN169	1	Block	LS-MW	Ab, (Qtz, Lpd)	0.46	0.39	0.22-0.51	3.8 (3)
Ng107	4	Block	MW	(Qtz, Lpd)	0.44	0.20	0.17-0.23	3.3 (11)
XN164	2	Block	LS-MW	Ab, Ptl, (Lpd)	0.40	0.41	0.26-0.60	3.6 (7)
XN166	2	Block	MW	Qtz, Lpd-Ms, (Ab)	0.40	0.30	0.27-0.32	0.5 (2)
Myokenzan pegmatite, Japan								
MY14	0.6	Block	MW-CL	Lpd, Qtz, Ab	0.42	0.40	0.33-0.48	0.0***
MY13	1	Block	LS-MW	Ab, (Tur, Qtz, Lpd)	0.36	0.24	0.14-0.38	0.0***
MY12	10	Block	CL-MW	Qtz	0.25	0.18	0.14-0.23	N.D.
MY11	10	Block	CL-MW	Ab, Qtz	0.18	0.15	0.10-0.17	N.D.
Other localities								
XS109	6	Block	MW	-	0.49	0.35	0.12-0.40	0.0***
XS113	12	Block	CL-MW	-	0.40	0.37	0.27-0.42	1.1 (3)
XS112	12	Block	MW	Ab, Qtz	0.29	0.31	0.16-0.39	6.0 (3)
XS110	2	Block	CY	-	0.13	0.14	0.12-0.17	N.D.

* Slightly associated minerals are noted in brackets.

** F contents were estimated from bulk powder XRD patterns for all specimens using Kallio's (1978) method.

*** Lacroixite was not detected by XRD pattern, and marginally confirmed by EPMA observation.

LS: light–salmon color, CL: colorless, MW: milky–white color, CY: clear yellow color. Qtz: quartz, Lpd: lepidolite, Ab: albite, Kfs: K-feldspar, Tur: Li tourmaline, Ptl: petalite, Ms: muscovite. N.D.: not detected.

The used specimens from the Nagatare pegmatite (XN, Ng) are same as Shirose & Uehara (2014). Other used specimens are as below. Myokenzan pegmatite, Ibaraki Prefecture, Japan (MY), Tanco pegmatite, Manitoba, Canada (XS109), Minas Gerais, Brazil (XS110), Havey pegmatite, Maine, U.S.A. (XS112), Varuträsk pegmatite, Västerbotten, Sweden (XS113).

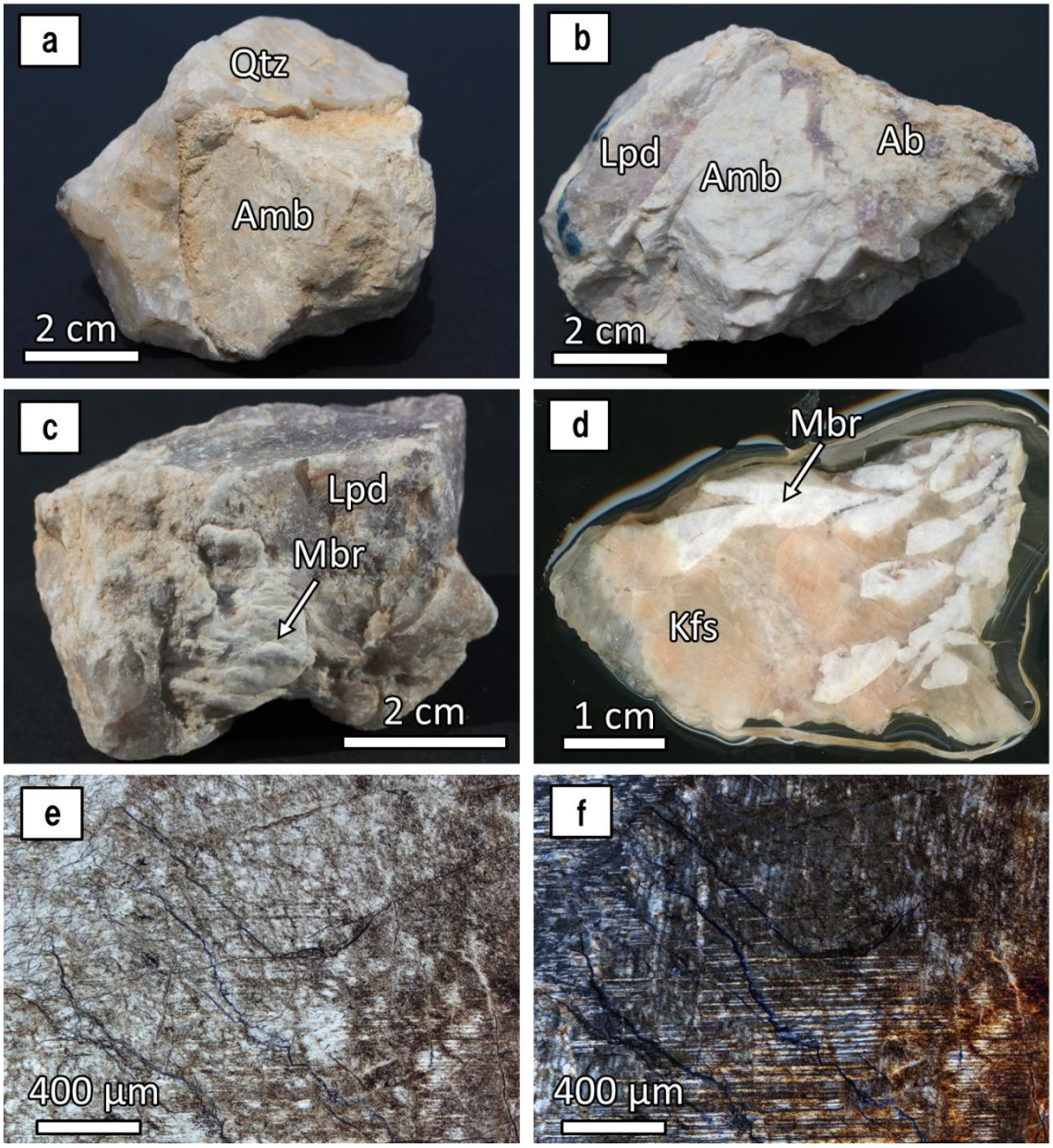

Fig. 11 Appearance and optical photo micrograph of montebrasite and amblygonite from the Nagatare pegmatite (Shirose & Uehara, in press). (a) and (b) Photographs of subhedral amblygonite (XN163 and XN162). (c) Photographs of subhedral montebrasite with microcrystalline lepidolite aggregates (XN166) (d) Photograph of dendritic montebrasite in K-feldspar (Ng104). (e) Plane-polarized optical photomicrographs of montebrasite, showing the cloudy parts and developed cracks (XN164). (f) Cross-polarized optical photomicrographs of montebrasite, showing the lattice-shaped polysynthetic twins of montebrasite (XN164). Amb: amblygonite, Qtz: quartz, Ab: albite, Lpd: lepidolite, Mbr: montebrasite, kfs: K-feldspar.

5.2.1 X-ray diffraction experiments at room temperature

Powder XRD data at room temperature were collected using a Bruker AXS M18XHF22-SRA. Fluorine contents for the montebrasite–amblygonite series were estimated from bulk powder XRD patterns for all specimens using Kallio's method (1978), whose method based on peak shifts corresponding to fluorine contents of the montebrasite–amblygonite series. The fluorine contents of the montebrasite–amblygonite series from the Nagatare pegmatite were F/(F+OH) = 0.40–0.59 (Table 1), consistent with a common value of the montebrasite–amblygonite series in natural occurrences. Lacroixite contents of the montebrasite–amblygonite series crystals from the Nagatare pegmatite were estimated from powder XRD patterns, and their values were 0.3–5.8 wt%.

5.2.2 Chemical analyses and microtextures

The fluorine contents in the montebrasite–amblygonite series measured by EPMA-WDS were inhomogeneous, and lower than the value estimated by XRD in some parts (Tables 1, 2, 3). In particular, secondary veined montebrasite, showing higher interference color under the polarization microscope, had extremely low fluorine contents. Na, Ca and Fe were not detected in montebrasite and amblygonite, except in the case of fine lacroixite contamination for a few analysis spots. The Li_2O and H_2O contents were estimated by stoichiometry.

In EPMA observation of textures, montebrasite and amblygonite were partially replaced by various secondary phosphates (Figs. 12a, b), crandallite, goyazite, fluorapatite, wardite, morinite, viitaniemiite, and so on, having a veined texture composed of acicular or platy fine crystals (Shirose & Uehara, 2014). However, lacroixite had different textures, whose patch or lamellae up to 10 μm were scattered and directionally arranged in montebrasite and amblygonite (Figs. 12c, d). In addition, lacroixite were contained in all specimens from the Nagatare pegmatite, differing from other Na-phosphates. Secondary veins of low fluorine contents montebrasite had no lacroixite inside (Figs. 12e, f). The chemical composition of lacroixite, having analytical difficulty for fineness and weakness for the beam damage, was shown in Table 2 and enriched in Na and F.

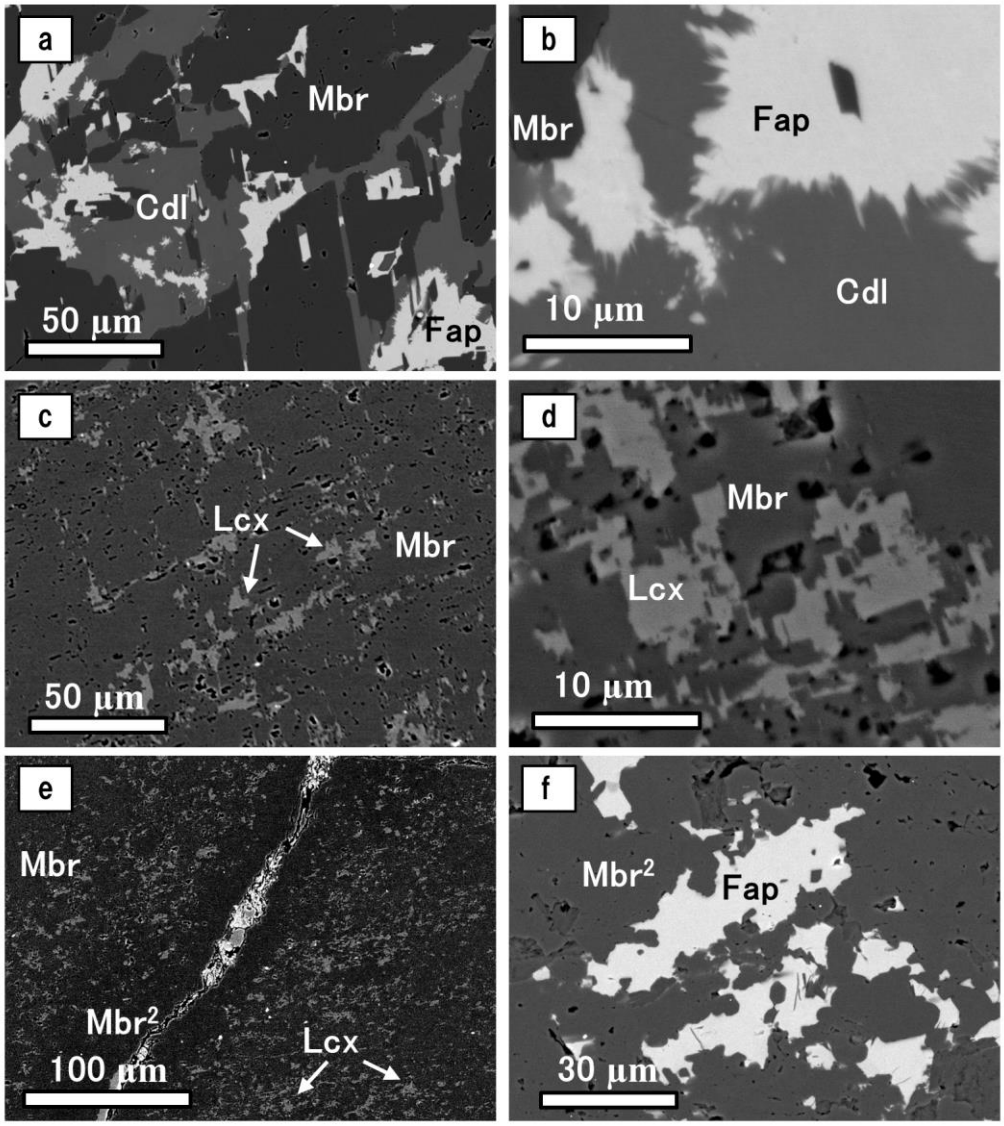

Fig. 12 BSE images of the internal textures in the montebrasite and amblygonite (Shirose & Uehara, in press). (a) Secondary phosphate veinlets composed of crandallite and fluorapatite along cleavages and composition planes of polysynthetic twins in montebrasite (Ng107). (b) Enlargement of Figure 12a. Fine grained acicular fluorapatite and platy crandallite with random orientation forms the aggregates. (c) Scattered lacroixite embedded in montebrasite (Ng107). (d) Enlargement of Figure 12c. Lacroixite had a patchy form. (e) Secondary low fluorine contents montebrasite along fracture with no lacroixite inside (XN164). (f) Fine grained low fluorine contents montebrasite formed secondary with fluorapatite had no lacroixite inside (XN165). Mbr: montebrasite, Cdl: crandallite, Fap: fluorapatite, Lcx: lacroixite, Mbr^2: secondary montebrasite.

Table 2. Representative chemical composition of the amblygonite, montebrasite, and secondary low fluorine contents montebrasite from the Nagatare pegmatite by EPMA analyses (Shirose & Uehara, in press).

Species	Amblygonite	Montebrasite	Low-F montebrasite	Lacroixite (n = 2)	
Sample no.	XN160	XN166	XN165	XN163	
P_2O_5	47.72	48.33	48.16	45.53	(2)
Al_2O_3	34.53	34.61	35.04	29.42	(0)
CaO	0.00	0.02	0.03	0.38	(3)
FeO	0.01	0.00	0.00		
Li_2O*	10.07	10.16	10.19		
Na_2O	0.00	0.00	0.01	16.76	(3)
F	7.12	3.84	1.36	10.38	(3)
H_2O*	2.70	4.31	5.50	0.58	
O=F	3.00	1.62	0.57	4.37	
Total	99.15	99.64	99.71	98.68	
		O = 4.5			
P	1.00	1.00	0.99	1.05	(0)
Al	1.00	1.00	1.01	0.95	(1)
Ca	0.00	0.00	0.00	0.01	(1)
Fe	0.00	0.00	0.00		
Li	1.00	1.00	1.00		
Na	0.00	0.00	0.00	0.89	(1)
F	0.56	0.30	0.10	0.90	(2)
OH	0.44	0.70	0.90	0.10	(2)
Cation sum	3.00	3.00	3.00	2.89	

* Li_2O and H_2O contents were calculated by stoichiometry.

Table 3. Average chemical composition of the montebrasite-amblygonite series specimens from the Nagatare pegmatite by EPMA analyses.

Sample no.	XN162	XN165	XN163	XN160	XN168	XN167
n	25	22	12	14	21	19
P_2O_5	48.62 (38)	48.13 (47)	48.01 (53)	48.00 (65)	48.78 (33)	48.46 (42)
Al_2O_3	35.12 (57)	34.84 (32)	35.00 (29)	34.90 (49)	35.14 (40)	35.59 (31)
CaO	0.02 (2)	0.02 (2)	0.02 (2)	0.01 (2)	0.03 (3)	0.02 (2)
FeO	0.02 (2)	0.01 (2)	0.01 (1)	0.01 (3)	0.02 (2)	0.01 (2)
Li_2O*	10.26 (9)	10.17 (7)	10.17 (9)	10.15 (10)	10.29 (6)	10.29 (6)
Na_2O	0.02 (5)	0.05 (10)	0.03 (3)	0.02 (5)	0.07 (8)	0.02 (3)
F	5.01 (120)	2.96 (127)	6.02 (38)	6.49 (37)	4.47 (75)	5.45 (85)
H_2O*	3.81 (54)	4.73 (60)	3.28 (19)	3.04 (20)	4.08 (35)	3.62 (39)
O=F	2.11 (50)	1.25 (53)	2.53 (16)	2.73 (16)	1.88 (31)	2.30 (36)
Total	100.77	99.65	100.01	99.90	100.99	101.18
P	1.00 (1)	1.00 (1)	0.99 (0)	1.00 (1)	1.00 (0)	0.99 (1)
Al	1.00 (1)	1.00 (1)	1.01 (1)	1.01 (1)	1.00 (1)	1.01 (1)
Ca	0.00 (0)	0.00 (0)	0.00 (0)	0.00 (0)	0.00 (0)	0.00 (0)
Fe	0.00 (0)	0.00 (0)	0.00 (0)	0.00 (0)	0.00 (0)	0.00 (0)
Li	1.00	1.00	1.00	1.00	1.00	1.00
Na	0.00 (0)	0.00 (0)	0.00 (0)	0.00 (0)	0.00 (0)	0.00 (0)
F	0.38 (9)	0.23 (10)	0.47 (3)	0.50 (3)	0.34 (6)	0.42 (6)
OH	0.62 (9)	0.77 (10)	0.53 (3)	0.50 (3)	0.66 (6)	0.58 (6)
Cation sum	3.00	3.00	3.01	3.00	3.00	3.01

* Li_2O and H_2O contents were calculated by stoichiometry.

Table 3 (continued).

Sample no.	Ng104	XN169	Ng107	XN164	XN166
n	19	16	14	23	13
P_2O_5	48.62 (38)	48.11 (45)	48.09 (41)	48.55 (40)	48.21 (27)
Al_2O_3	35.12 (46)	35.35 (41)	34.99 (42)	35.17 (31)	34.90 (28)
CaO	0.01 (2)	0.01 (2)	0.02 (2)	0.02 (2)	0.02 (2)
FeO	0.01 (2)	0.00 (1)	0.02 (2)	0.02 (2)	0.01 (1)
Li_2O*	10.26 (8)	10.22 (9)	10.17 (8)	10.26 (7)	10.18 (6)
Na_2O	0.01 (2)	0.03 (4)	0.00 (0)	0.09 (12)	0.01 (1)
F	5.27 (39)	5.12 (93)	2.64 (21)	5.36 (147)	3.82 (17)
H_2O*	3.69 (19)	3.74 (44)	4.88 (11)	3.64 (69)	4.33 (8)
O=F	2.22 (17)	2.15 (39)	1.11 (9)	2.26 (62)	1.61 (7)
Total	100.77	100.43	99.70	100.86	99.87
P	1.00 (1)	0.99 (0)	0.99 (1)	1.00 (0)	1.00 (0)
Al	1.00 (1)	1.01 (1)	1.01 (1)	1.00 (1)	1.00 (0)
Ca	0.00 (0)	0.00 (0)	0.00 (0)	0.00 (0)	0.00 (0)
Fe	0.00 (0)	0.00 (0)	0.00 (0)	0.00 (0)	0.00 (0)
Li	1.00	1.00	1.00	1.00	1.00
Na	0.00 (0)	0.00 (0)	0.00 (0)	0.00 (1)	0.00 (0)
F	0.40 (3)	0.39 (7)	0.20 (2)	0.41 (11)	0.30 (1)
OH	0.60 (3)	0.61 (7)	0.80 (2)	0.59 (11)	0.70 (1)
Cation sum	3.00	3.01	3.00	3.01	3.00

5.2.3 TEM/STEM observations for the microtexture of lacroixite and montebrasite

Ion-milled specimens of montebrasite with lacroixite were used for TEM/STEM observations. Lacroixite was observed in montebrasite, and it had bidirectionally developed patch texture, with flat planes on the boundary with montebrasite. Furthermore, lacroixite was associated with low fluorine contents montebrasite, which also formed nanoscale lamellae within the patch (Figs. 13a, b). Their selected area electron diffraction (SAED) patterns overlapped each other, though they appeared as the split of the spots due to the difference of unit cell parameters (Figs. 13c, d). It indicates that the crystal orientations of lacroixite and host montebrasite were exactly similar, and low fluorine contents montebrasite was also similar.

X-ray mapping images were shown in Figure 14. Though there were three mineral areas, montebrasite, low fluorine contents montebrasite and lacroixite, their chemical compositions were homogeneous in their grains. The grain boundaries were consisted of (1−10) and (110) planes. The former were developed between the patch and host montebrasite, while the latter were developed between lacroixite and low fluorine contents montebrasite (Fig. 15).

Figure 16 show high resolution image of lacroixite from [001] direction and crystal structures of montebrasite and lacroixite. Both planes are composed of arranged AlO_6 polyhedral chains along the *c* axis, and are cleavage planes.

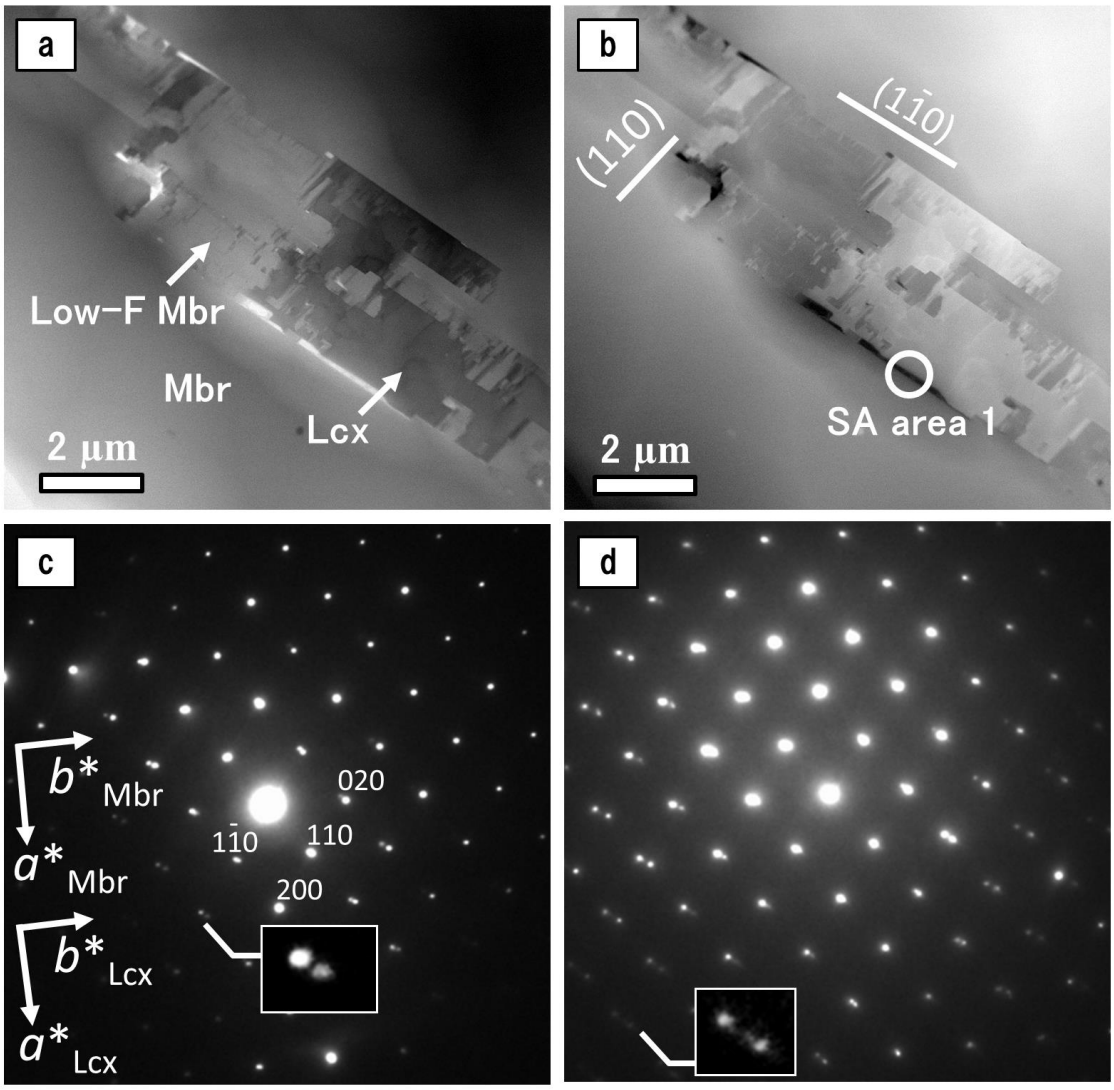

Fig. 13 STEM bright field/high angle annular dark field (BF/HAADF) images of lacroixite patch, and selected area electron diffraction patterns (Ng104) (Shirose & Uehara, in press). (a) STEM BF image from $[001]_{Mbr}$. (b) STEM HAADF image of same area as Figure 13a. Lacroixite had bidirectionally developed patch texture with flat planes on the boundary with montebrasite, and lacroixite was associated with low fluorine contents montebrasite. Boundary planes were composed of (110) and highly developed (1−10) planes. (c) Selected area electron diffraction (SAED) patterns from the circle area in Figure 13b. Patch lacroixite and host montebrasite had exactly similar crystal orientation. The enlarged image shows the split of the spots due to the difference of unit cell parameters. (d) SAED patterns of lacroixite, low fluorine contents montebrasite and host montebrasite. The enlarged image shows the triple spots. Mbr: montebrasite, Lcx: lacroixite, Low-F Mbr: low fluorine contents montebrasite.

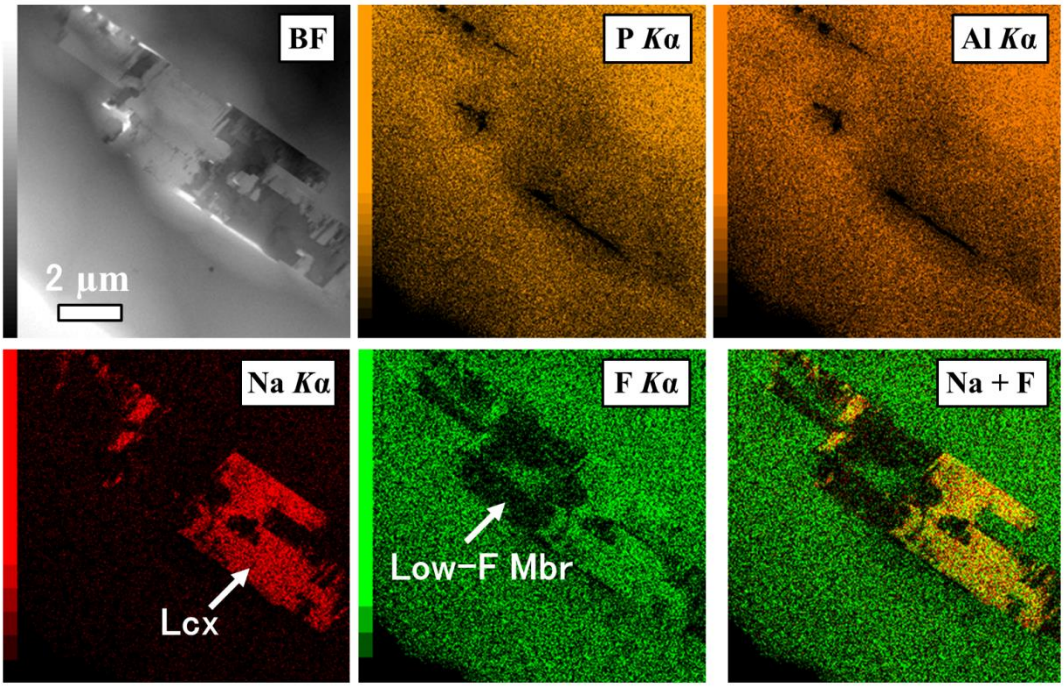

Fig. 14 X–ray images of elements distribution map (BF image, P*K*α, Al*K*α, Na*K*α, F*K*α, and overlay image of Na*K*α and F*K*α) (Shirose & Uehara, in press).

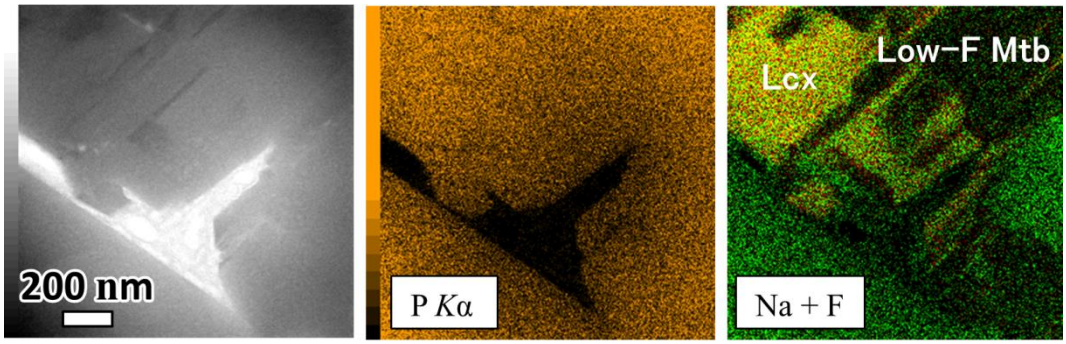

Fig. 15 X–ray images of elements distribution map in enlarged are of Figure 14 (BF image, P*K*α, and overlay image of Na*K*α and F*K*α).

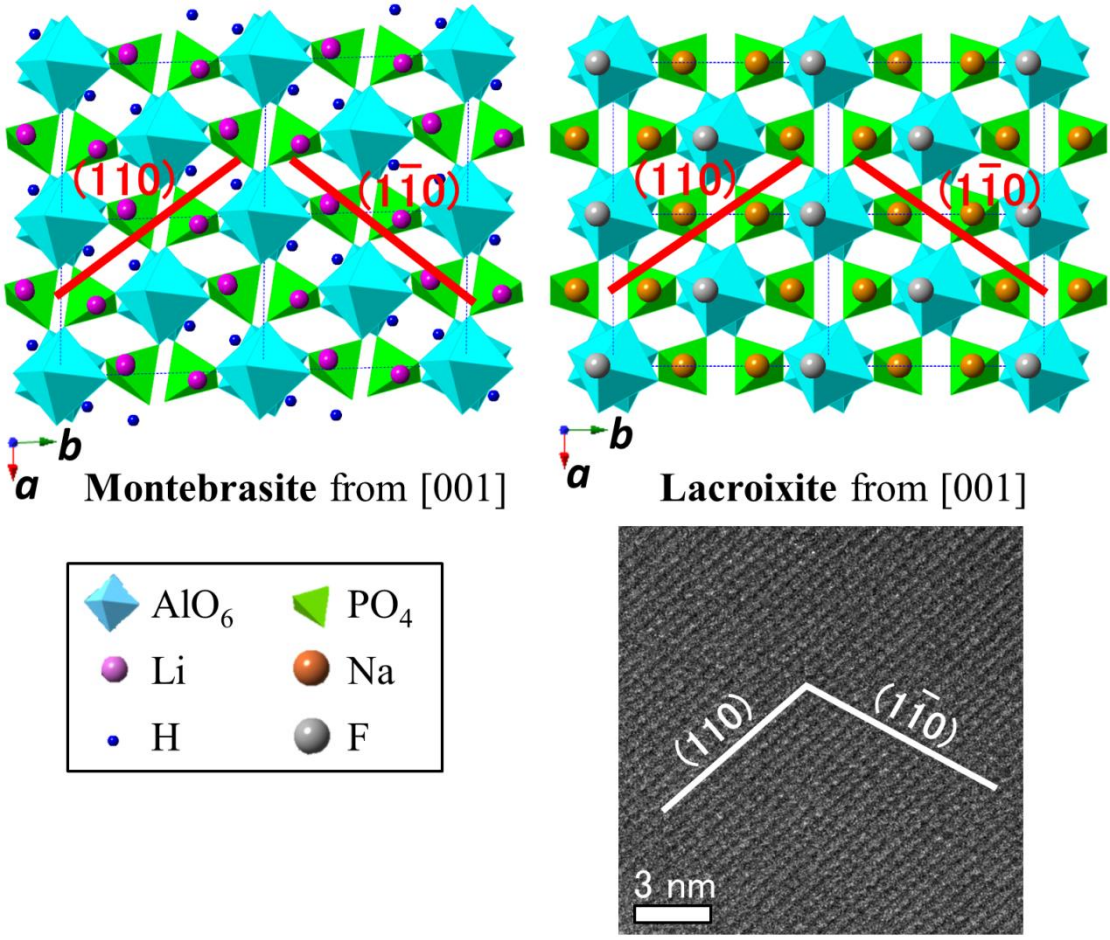

Fig. 16 Crystal structures of montebrasite and lacroixite from [001] direction and high resolution TEM (HRTEM) image of lacroixite from [001] direction (Shirose & Uehara, in press). Crystal structure data were referenced from Groat *et al*. (2003) and Pajunen & Lathi (1985). The montebrasite–amblygonite series is topologically identical to the lacroixite structure. (110) and (1−10) planes are composed of arranged AlO_6 polyhedral chains along *c* axis, and they are cleavage planes.

5.2.4 X-ray diffraction experiments at high temperature

The amblygonite specimen, having internal chemical composition in the montebrasite–amblygonite series, was heated from 50 to 700 °C and the XRD patterns were measured *in situ*. The experiments were performed by RIGAKU Ultima IV diffractometer. Heating condition was set at 10 °C/min by thermocouple under vacuum, and they were measured after holding at the target temperature for 10 minutes. In results, changes of unit cell parameters on amblygonite were confirmed. However, amblygonite was partially broken down at 600 °C and anhydrous phosphates were formed (Fig. 17).

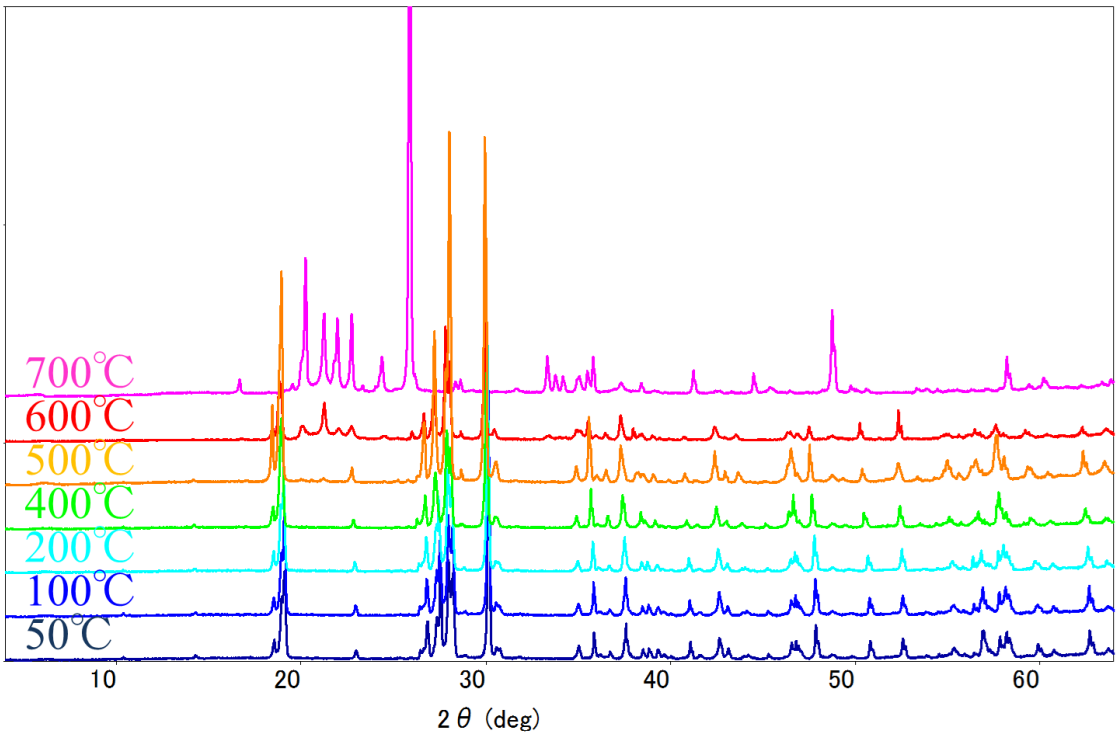

Fig. 17 X-ray diffraction patterns of amblygonite (F = 0.54, XN163) from 50 to 700 ºC.

With increasing temperature, *b* axis quite increases than *a* and *c* axes, and *α*, *β*, and *γ* decrease (Fig. 18). At 700 °C, amblygonite was completely broken down and berlinite was formed. The changes of unit cell parameters for the montebrasite-amblygonite series at high temperature is consistent with the behavior at low temperature, were examined by Groat *et al*. (2003). Increasing temperature make the montebrasite–amblygonite series closing to the monoclinic structure like lacroixite. Easy breakdown of amblygonite with increasing temperature is caused by anhydration in vacuum condition.

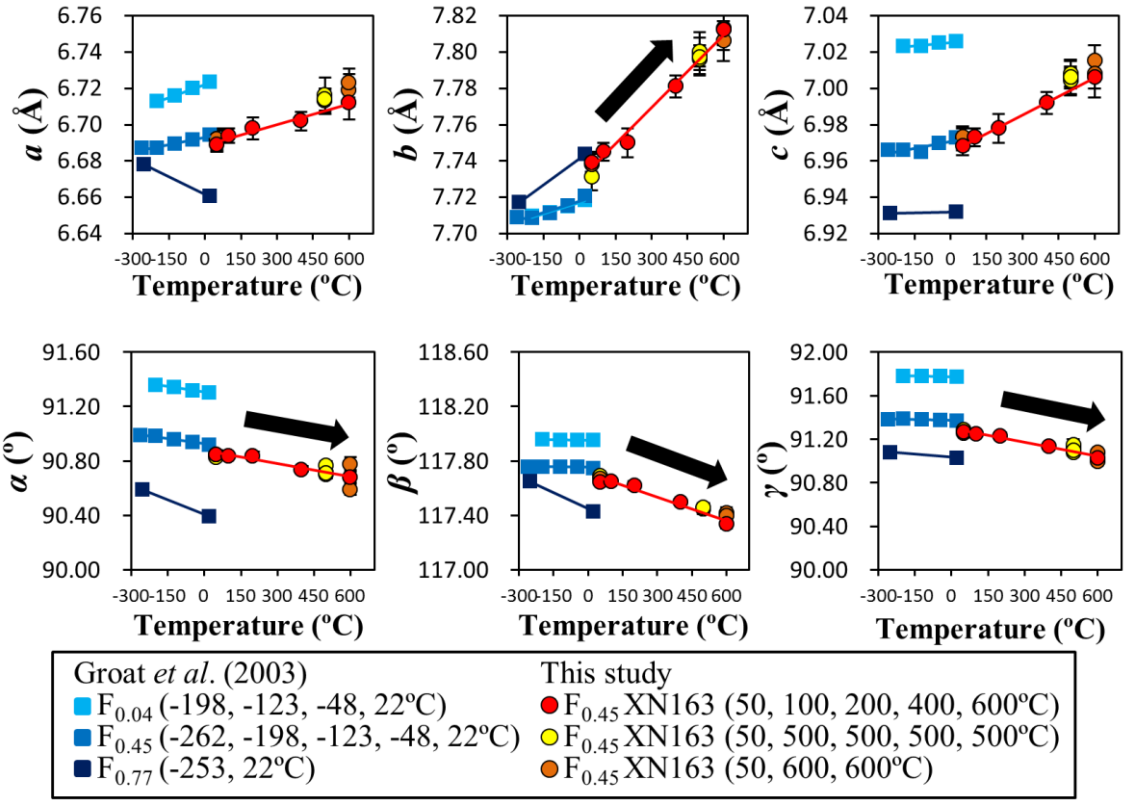

Fig. 18 Changes of unit cell parameters of the montebrasite–amblygonite series (Shirose & Uehara, in press). Amblygonite specimen was heated from 50 to 700 °C and the XRD patterns were measured in situ (XN163). Data at low temperatures are from Groat *et al*. (2003). The bars indicate standard deviations.

5.3 Exsolution process of the montebrasite-amblygonite series and lacroixite

Lacroixite was found in all specimens from the Nagatare pegmatite as scattered patch or lamella embedded in montebrasite and amblygonite, unlike other secondary phosphates. It indicates that the formation process is different from hydrothermal alteration as in other secondary phosphates. The fact that secondary montebrasite veins contain no lacroixite, generally contained in surrounding the montebrasite–amblygonite series, also supports the possibility. The scattered lacroixite texture is similar to "natromontebrasite", a discredited species that was determined to be a mixture of an OH-rich amblygonite and lacroixite (Fransolet 1989, Fransolet *et al*. 2007).

TEM/STEM analyses show that lacroixite forms patches with same crystal orientation as host montebrasite, associated with low fluorine contents montebrasite; they have a crystallographic relationship. Thus, it is estimated that the microtexture of the montebrasite–amblygonite series and lacroixite is formed as below. First, a high temperature phase, (Li,Na)$AlPO_4$(OH,F) with *C*2/*c* including high Li contents, is formed, and then with decreasing temperature, the phase is exsolved into high montebrasite–amblygonite, $LiAlPO_4$(OH,F) with *C*2/*c*, and lamella of a middle temperature phase, (Li,Na)$AlPO_4$(OH,F) with *C*2/*c* containing approximately same amount of Li and Na (Fig. 19). Host phase subsequently transform to the montebrasite–amblygonite series, $LiAlPO_4$(OH,F) with *C*−1, and polysynthetic twins are formed in the montebrasite–amblygonite series during this transition. Finally, the lamella of middle temperature phase is exsolved into low fluorine contents montebrasite, $LiAlPO_4$(OH) with *C*−1, and lacroixite, $NaAlPO_4F$ with *C*2/*c*. As a result, the montebrasite–amblygonite series has the patch or lamella texture shown in EPMA and TEM/STEM observation.

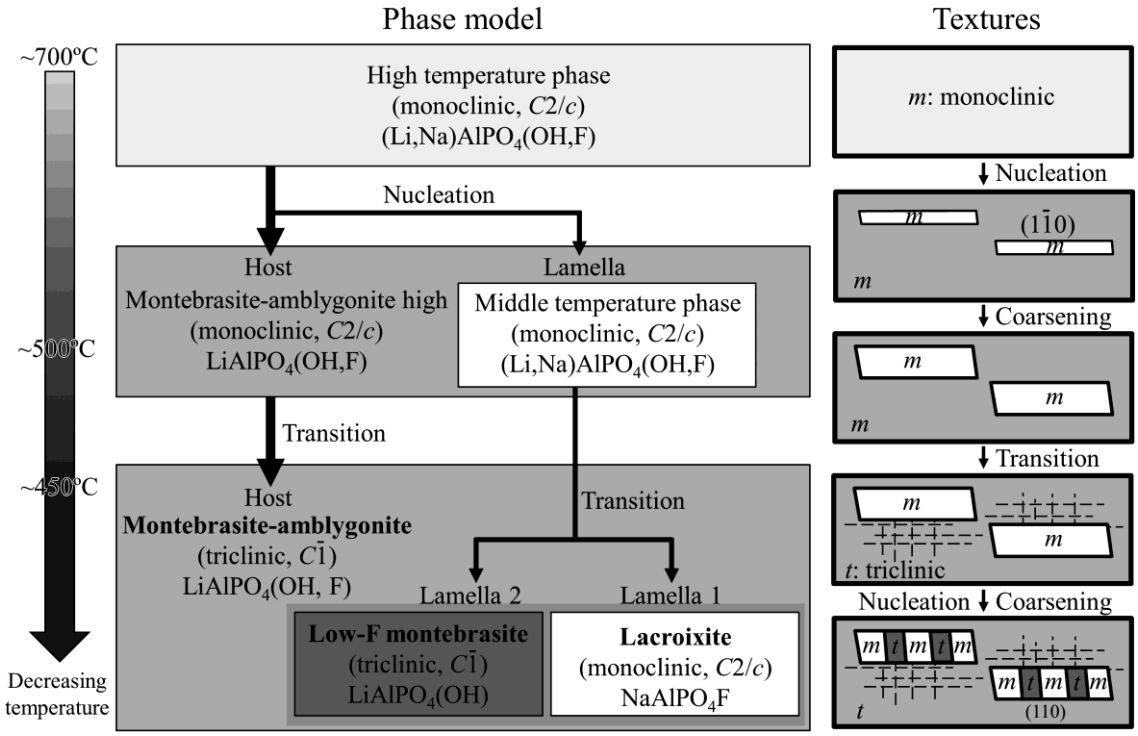

Fig. 19 Schematic diagram of exsolution process model in the montebrasite–amblygonite series (Shirose & Uehara, in press). The right column shows the change of textures. Dashed lines in the texture models represent the formation of polysynthetic twins.

The montebrasite–amblygonite series is topologically identical to the lacroixite structure, while Na could not substitute Li in the montebrasite–amblygonite series structure (Groat *et al*. 1990). However, there is a possibility of making a solid solution at high temperature, and the lower temperature it gets, the larger the miscibility gap between lacroixite and the montebrasite–amblygonite series is. This is caused by the difference of ion radius between Li^+ and Na^+, and it is an analogue of the exsolution process on alkali feldspar like perthite. Fransolet (1989) reported that lacroixite could contain minor Li^+ and OH^- with changes of the unit cell parameters. The change is noticeable for *b* axis, similar to that of the montebrasite–amblygonite series under the heating conditions in this paper. The lamellae in TEM/STEM observations are composed of low fluorine contents montebrasite and fluorine rich lacroixite, which indicates that OH^- is suitable for triclinic structure with Li^+, while F^- is for

monoclinic structure with Na^+ at low temperature. The reason for low fluorine contents of secondary montebrasite formed by a hydrothermal alteration is a crystallographic restriction in addition to the formation at a low fluorine environment. This is supported by association of low fluorine contents montebrasite and fluorapatite or the formation of fluorine rich minerals such as morinite and viitaniemiite by the hydrothermal alteration.

5.4 Exsolution texture and occurrence condition

The observation of the montebrasite–amblygonite series from the Nagatare pegmatite provided the formation process of patch or lamella texture in the montebrasite–amblygonite series caused by the change of crystallographic properties with decreasing temperature. The lacroixite contents of montebrasite-amblygonite series estimated by XRD patterns is correlated to fluorine contents of montebrasite-amblygonite series. The lacroixite contents are subdivided to three series, high, middle, and low lacroixite series (Fig. 20), and they are corresponding to large, middle, and fine grained montebrasite-amblygonite series. In particular, low lacroixite contents montebrasite has dendritic and fine textures, which indicates that lower temperature environments with rapid growth under the supercool conditions form low lacroixite contents montebrasite-amblygonite series. High lacroixite contents series with large grain size are formed under the small undercool and higher temperature conditions.

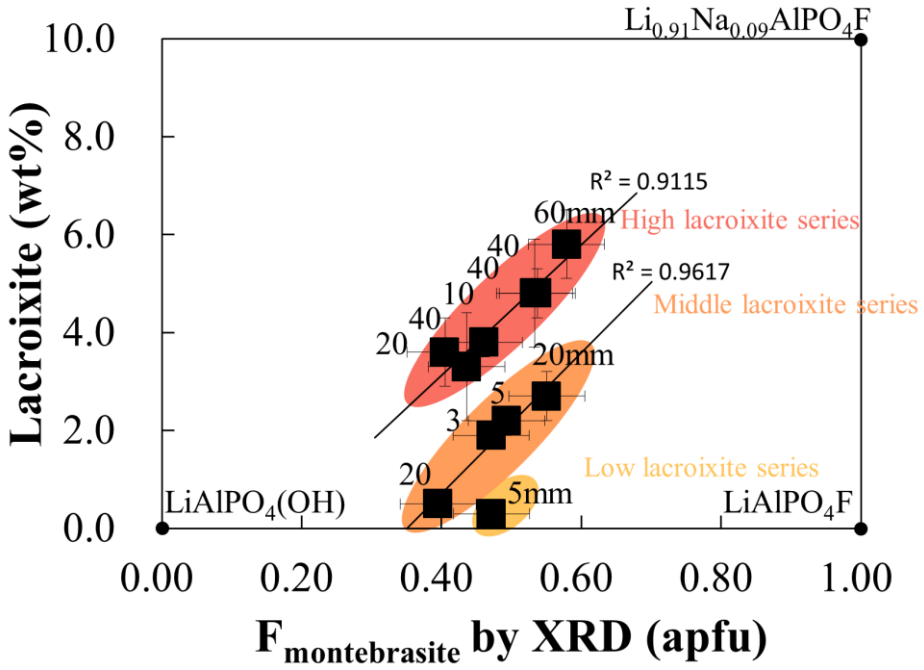

Fig. 20 Fluorine contents (*apfu*) versus lacroixite contents (wt%) of montebrasite and amblygonite from Nagatare Li pegmatite, estimated by XRD patterns (Shirose & Uehara, in press). The values on symbols indicate grain size. The bars indicate standard deviations.

The lacroixite contents could be applied to the primary montebrasite–amblygonite series formed at high temperature from other localities. Furthermore, it is estimated that the exsolution texture and lacroixite are not present in the montebrasite–amblygonite series formed at low temperature. The montebrasite and amblygonite specimens from other localities, five localities including 8 specimens, were also investigated in this study (Tables 1, 4, 5). The four specimens from Myokenzan pegmatite, Japan and the specimen from Tanco pegmatite, Canada have polysynthetic twins under the polarized microscope; however, they have no lacroixite contents in XRD pattern. For middle fluorine contents specimens (MY13, MY14, XS109), lacroixite was marginally confirmed in EPMA observation. The specimens from Varuträsk pegmatite, Sweden, and Havey pegmatite, U.S.A. have polysynthetic twins and lacroixite patches as in the specimens from the Nagatare pegmatite. Characteristic property was confirmed for the specimen from Minas Gerais, Brazil, where the polysynthetic twins and lacroixite are not present in montebrasite (Fig. 21). This type of montebrasite corresponds to gem-quality montebrasite from drusy vugs formed at low temperature. Černá *et al*. (1973) and Rondeau *et al*. (2006) reported that water-clear gem-quality montebrasite have extremely low fluorine contents, and our specimen also has low fluorine contents.

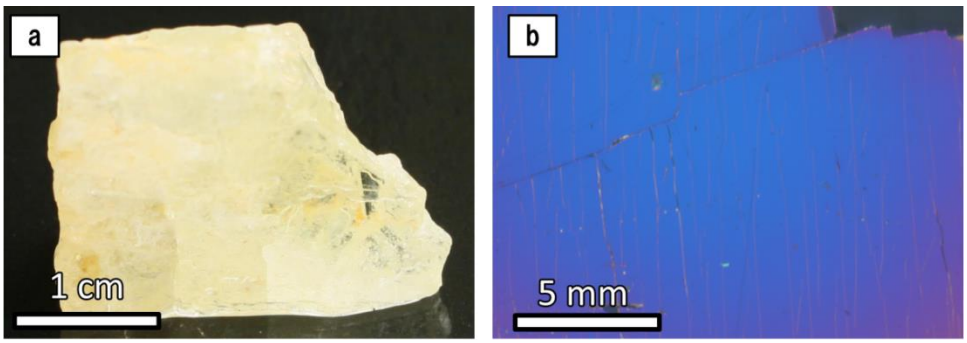

Fig. 21 Appearance of water clear montebrasite from Minas Gerais, Brazil. (a) Photograph of specimen. (b) Cross-polarized optical photomicrographs of montebrasite, showing that it has not polysynthetic twins and cloudy part.

Table 4. Average chemical composition of the montebrasite-amblygonite series specimens from Myokenzan pegmatite by EPMA analyses.

Sample no.	MY14	MY13	MY12	MY11
n	22	22	19	11
P_2O_5	47.95 (47)	47.68 (39)	48.78 (50)	48.63 (36)
Al_2O_3	33.83 (31)	33.60 (36)	34.63 (57)	34.75 (36)
CaO	0.02 (3)	0.03 (3)	0.02 (2)	0.02 (2)
FeO	0.02 (2)	0.02 (3)	0.02 (2)	0.01 (2)
Li_2O*	10.03 (8)	9.97 (7)	10.23 (12)	10.22 (7)
Na_2O	0.01 (4)	0.00 (0)	0.00 (0)	0.00 (1)
F	5.06 (41)	3.08 (92)	2.38 (32)	1.94 (27)
H_2O*	3.65 (21)	4.55 (44)	5.04 (16)	5.24 (13)
O=F	2.13 (17)	1.30 (39)	1.00 (13)	0.82 (11)
Total	98.45 73	97.63	100.09	100.00
P	1.01 (0)	1.01 (0)	1.00 (0)	1.00 (0)
Al	0.99 (1)	0.99 (1)	0.99 (1)	1.00 (1)
Ca	0.00 (0)	0.00 (0)	0.00 (0)	0.00 (0)
Fe	0.00 (0)	0.00 (0)	0.00 (0)	0.00 (0)
Li	1.00	1.00	1.00	1.00
Na	0.00 (0)	0.00 (0)	0.00 (0)	0.00 (0)
F	0.40 (3)	0.24 (7)	0.18 (2)	0.15 (2)
OH	0.60 (3)	0.76 (7)	0.82 (2)	0.85 (2)
Cation sum	3.00	3.00	3.00	3.00

* Li_2O and H_2O contents were calculated by stoichiometry.

Table 5. Average chemical composition of the montebrasite-amblygonite series specimens from the various pegmatites by EPMA analyses.

Sample no.	XS109	XS113	XS112	XS110	XS114
n	16	31	15	14	17
P_2O_5	48.23 (39)	48.52 (58)	48.52 (44)	48.02 (35)	48.88 (43)
Al_2O_3	34.83 (42)	34.50 (40)	34.47 (48)	34.97 (38)	34.38 (27)
CaO	0.01 (2)	0.02 (2)	0.03 (3)	0.01 (2)	0.03 (3)
FeO	0.02 (2)	0.01 (2)	0.03 (3)	0.03 (3)	0.02 (3)
Li_2O*	10.17 (8)	10.18 (9)	10.18 (8)	10.16 (7)	10.21 (6)
Na_2O	0.00 (0)	0.05 (24)	0.02 (3)	0.00 (1)	0.01 (2)
F	4.53 (81)	4.75 (101)	4.01 (90)	1.86 (18)	1.07 (57)
H_2O*	3.99 (37)	3.89 (48)	4.23 (40)	5.25 (8)	5.65 (28)
O=F	1.91 (34)	2.00 (43)	1.69 (38)	0.78 (7)	0.45 (24)
Total	99.87	99.92	99.79	99.53	99.80
P	1.00 (0)	1.00 (1)	1.00 (1)	0.99 (0)	1.01 (0)
Al	1.00 (1)	0.99 (1)	0.99 (1)	1.01 (1)	0.99 (1)
Ca	0.00 (0)	0.00 (0)	0.00 (0)	0.00 (0)	0.00 (0)
Fe	0.00 (0)	0.00 (0)	0.00 (0)	0.00 (0)	0.00 (0)
Li	1.00	1.00	1.00	1.00	1.00
Na	0.00 (0)	0.00 (1)	0.00 (0)	0.00 (0)	0.00 (0)
F	0.35 (6)	0.37 (8)	0.31 (7)	0.14 (1)	0.08 (4)
OH	0.65 (6)	0.63 (8)	0.69 (7)	0.86 (1)	0.92 (4)
Cation sum	3.00	3.00	3.00	3.00	3.00

* Li_2O and H_2O contents were calculated by stoichiometry.

Černá *et al*. (1973) analysed montebrasite and amblygonite from various localities mainly including specimens from Tanco pegmatite by wet chemical analyses, and indicated that Na contents of the montebrasite–amblygonite series had positive correlation to F contents. However, the montebrasite–amblygonite series could not contain Na at room temperature, and the Na rich specimens (AF-1, AF-65) in Černá *et al*. (1973) were confirmed the contents of abundant lacroixite by Groat *et al*. (1990). Therefore, Na contents of montebrasite and amblygonite in Černá *et al*. (1973) could be converted to lacroixite contents (Fig. 22).

London *et al*. (2001) indicated that synthesized montebrasite and amblygonite in haplogranitic melt, at 585 °C and 200 MPa H_2O, had positive correlation of Na and F by EPMA analysis, though natural amblygonite had no Na contents. It is considered as fine lacroixite mixture or high temperature phase, and they could be converted to lacroixite contents as approximation. The converted data set are shown in Figure 23. For temperatures of their montebrasite and amblygonite from various localities, they are roughly estimated from Li-aluminosilicates phase diagram (London 1984). In the Nagatare pegmatite, petalite occurs without spodumene. In Myokenzan pegmatite, spodumene occurs without petalite, and in Tanco pegmatite, both minerals occur. These forming conditions are reflected to lacroixite contents; the montebrasite–amblygonite series from high temperature Li pegmatite with only petalite as Li-aluminosilicate phase has low to high lacroixite contents, and the montebrasite–amblygonite series from lower temperature Li pegmatite with spodumene has no or low lacroixite contents.

Though lacroixite contents are restricted by temperature, they are also reflected by the chemical environment secondly. The Na and F activity changes the quantity of lacroixite; in the Nagatare pegmatite, montebrasite in K-feldspar had relatively low lacroixite contents. The upper limit of lacroixite contents in the montebrasite–amblygonite series is correlated to F contents as shown in positive correlation of Na and F.

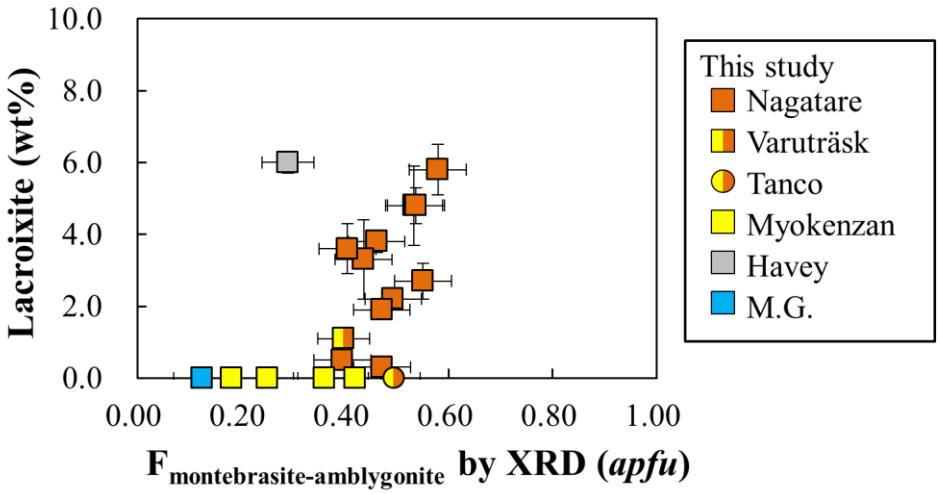

Fig. 22 Fluorine contents (*apfu*) versus lacroixite contents (wt%) of montebrasite and amblygonite estimated by XRD patterns in this thesis (Shirose & Uehara, in press). The detailed properties are listed in Table 1. The colors of symbols correspond to the formation environment; orange: petalite occurrence, bicolor: petalite and spodumene occurrence, yellow: spodumene occurrence, grey: no aluminosilicate or uncertain, light blue: in cavity. The bars indicate standard deviations.

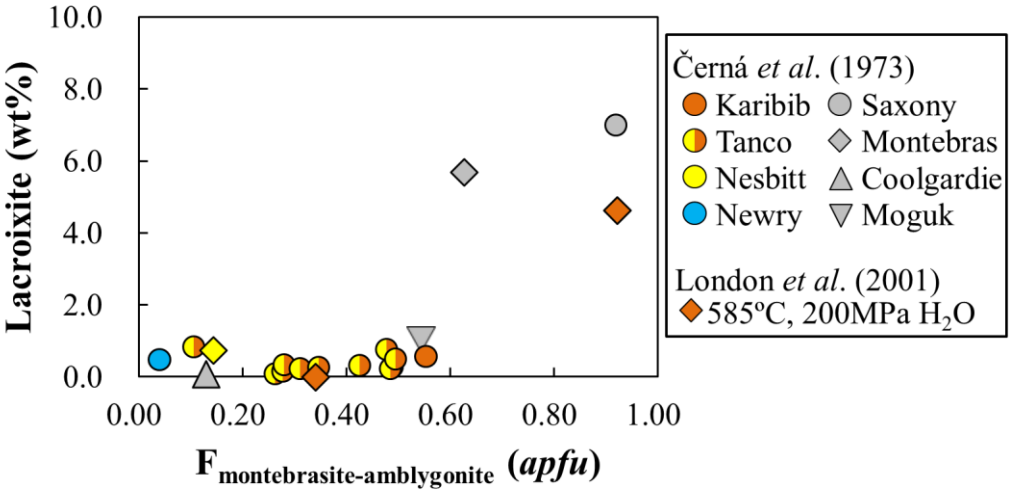

Fig. 23 Fluorine contents (*apfu*) versus lacroixite contents (wt%) of montebrasite and amblygonite in previous studies (Shirose & Uehara, in press). The lacroixite contents were converted from Na_2O contents of montebrasite and amblygonite. The data were referenced from chemical analyses of montebrasite and amblygonite from various localities (Černá *et al.* 1973) and synthesized montebrasite and amblygonite at 585 °C and 200 MPa H_2O (London *et al.* 2001). Colors of symbols are the same as Figure 22.

Amblygonite with high F contents from topaz-bearing granites of Western Europe contain abundant lacroixite (London *et al*. 2001, Groat *et al*. 1990). This limit may be related to the change of unit cell parameters getting close to monoclinic structure like lacroixite with increasing F contents. Low temperature montebrasite with gem-quality or secondary has no lacroixite contents and highly triclinic structure, and there is a possibility that these crystallographic properties connect to low fluorine contents.

Investigating fine structures of the montebrasite–amblygonite series provides information of thermal changes and chemical environments at pegmatite formation. For more quantitative restriction, synthetic experiments and the research on the effect of hydrothermal alterations are required.

6 HYDROTHERMAL ALTERATION

6.1 Hydrothermal alteration in Li pegmatite

Alterations to fine grained eucryptite, albite and muscovite from primary Li-aluminosilicates, such as spodumene and petalite, are often observed in Li pegmatite, and those are suggested as reactions caused by hydrothermal alterations at a late stage of Li pegmatite forming process (*e.g.*, London & Burt 1982). London & Burt (1982) described the alteration of spodumene, montebrasite, and lithiophilite from White Picacho District, Arizona, U.S.A. Bobos *et al*. (2009) studied cookeite alteration of spodumene, and revealed the *P-T* conditions. However, general sequence of hydrothermal alteration in Li pegmatite is not obvious, and the formed clay minerals have not been studied in detail. In addition, an alteration products of pink Li tourmaline are unclear, despite the general occurrences in Li pegmatites. Tourmaline group minerals from Li pegmatite occur with change in the chemical composition on various formation stages, and investigation of the alteration processes are valuable for discussing the behavior of residual fluids in Li pegmatite. Generally, these alteration products are fine grained, and bearing microtextures. For analyzing these micro alteration textures, transmission electron microscope is effective.

In this section, we describe the hydrothermal alterations and microtextures in K-feldspar, petalite, Li tourmaline, and the montebrasite-amblygonite series with various alteration grades from the Nagatare Li pegmatite. They were investigated by XRD, EPMA and TEM/STEM, and the alteration processes were discussed. Used specimens are shown in Table 6.

Table 6. Specimen list with associated minerals and mineralogical properties of clay minerals from the Nagatare Li pegmatite.

Specimen No.	Color	Form	Origin	Alteration products	Polytypes of muscovite	Associated minerals	Ltp
Ng10	Purple-white	Prismatic	Li-Tur(Eb)	Ms, Ms+Cok	$2M_1$, $2M_1$+1M	Ab, Qtz, Lpd	○
	White	Mass	Kfs	Ms+Qtz, Cok+Qtz	$2M_1$		
Ng17	Purple-White	Prismatic	Li-Tur(Feb)	Ms, (Cok)	$2M_1$, $2M_1$+1M	Ab, Lpd, Qtz, Kfs	
Ng14	Purple-white	Prismatic	Li-Tur?	Ms, (Cok)	$2M_1$	Lpd, Qtz, Ab, Kfs	○
Ng114	Purple	Prismatic	Li-Tur?	Ms	$2M_1$	-	
Ng116	Purple-green	Radial	Li-Tur?	Ms, (Cok)	$2M_1$, $2M_1$+1M , $2M_1$+1M +3T	Lpd, Ab	
Ng102	White	Mass	Kfs	Cok+Qtz		Lpd	○
Ng103	White	Mass	Kfs	Cok+Qtz		Lpd	○
Ng111	White	Mass	Kfs	Cok+Qtz		Lpd	○
Ng112	White	Mass	Kfs	Cok+Qtz		Ab	○
Ng132	Light pink	Mass	Kfs	Cok+Qtz		-	○
	Light pink	Powder	Kfs	Kbd+Ts+Cok+Qtz			
Ng139	White	Mass	Kfs	Cok+Qtz, Ts+Qtz		Ab, Qtz	○
Ng151	White-light pink	Mass	Kfs	Cok+Qtz		Lpd, Qtz, Ab	○
Ng134	Light blue	Powder	Kfs	Ts+Qtz		Qtz, Lpd	○
	White	Mass	Kfs	Cok+Qtz			
Ng136	Light blue	Powder	Kfs	Ts+Qtz		Ab, Qtz, Lpd	○
XN350	Red	Powder	Ptl	KBd+Cok+Qtz		Ptl, Qtz, Lpd	○
XN351	Pink	Powder	Ptl	KBd+CaBd+Qtz		Ptl. Qtz, Ab	○
Ng153	Pink-red	Powder	Ptl	CaBd+KBd+CaMnt+Cok+Qtz		Ptl, Ab, Qtz, Lpd	○
Ng146	Red-white	Powder	Ptl?	CaMnt+Qtz		-	○

Li-Tur: Li tourmaline, Eb: elbaite, Feb: fluor-elbaite, Kfs: K-feldspar, Ptl: petalite, Ms: muscovite, Cok: cookeite, Qtz: quartz, Ts: Li tosudite, KBd: K beidellite, Cabd: Ca beidellite, CaMnt: Ca montmorillonite, Ab: albite, Lpd: lepidolite. Ltp: lithiophorite association.

6.2 Hydrothermal alteration in the Nagatare pegmatite

Alterations of primary minerals are predominant for Li rich part of Li pegmatite. Especially, the alteration is significant for K-feldspar, petalite, pink Li tourmaline, and the montebrasite-amblygonite series. Some K-feldspar and petalite include macroscopically visible alteration part as clay like minerals. In previous studies, montmorillonite was reported from the Nagatare pegmatite as montmorillonite-beidellite series (*e.g.*, Takimoto 1937), which has red or light blue color and water swellable. Takimoto (1937) described that the red clays derived from albite. Clay like minerals occur with Li minerals, which is red, pink, light blue, and white color in a state of aggregate or powder. In Nagatare pegmatite, a white or light pink mass of cookeite and large quartz grain was reported as the first cookeite in Japan by Sakurai *et al*. (1973). We described some alterations that the montebrasite-amblygonite series has white altered veins inside (Shirose & Uehara 2014), and pink Li tourmaline is often altered to mica partially or perfectly with pseudomorph (Shirose & Uehara 2013).

6.2.1 Li chloritization

Li chloritization, an alteration to cookeite $[(LiAl_2)(OH)_6][Al_2(Si_3Al)O_{10}(OH)_2]$, is generally observed under the electron microscope in minerals from Li rich part of the Nagatare pegmatite. It is notable that Li chloritization of K-feldspar is significant and macroscopically visible (Figs. 24, 25). The cookeite and quartz pseudomorph occurs as large crystal (about 10 cm) with white, pale yellow, or pale pink color, and it has a trace of cleavage of K-feldspar. The aggregates were mainly composed of cookeite and quartz, with minor relicts of K-feldspar. Cookeite forms spherical shape of fine platy crystals, and quartz has subhedral to euhedral form (Figs. 25c, d).

While the aggregates of cookeite and quartz were very dense, they had druses after erosion of K-feldspar. The minor relicts of K-feldspar show the strong alteration to cookeite for comparison to other primary minerals The chemical compositions of cookeite are shown in Table 7, and accessary elements such as Fe, Mn, and Mg are negligible. Li chloritization of K-feldspar is described as follow reaction:

$5KAlSi_3O_8 + 4H^+ + Li^+ + 2H_2O \rightarrow [(LiAl_2)(OH)_6][Al_2(Si_3Al)O_{10}(OH)_2] + 12SiO_2 + 5K^+$

K-feldspar Cookeite Quartz

which explains that K-feldspar reacted with hydrothermal fluids that possess high Li^+ activity and weakly acidity at high temperature.

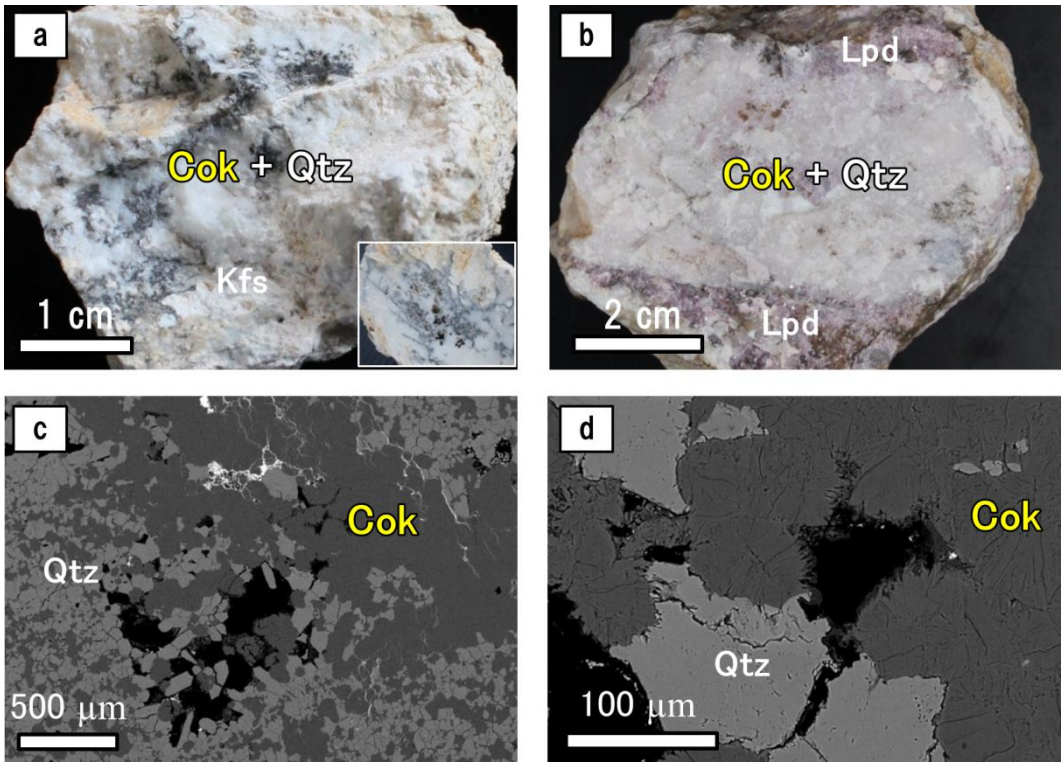

Fig. 24 Appearances and BSE images of aggregate composed of cookeite and quartz after K-feldspar. (a) Photograph of white aggregate after K-feldspar (Ng139). (b) Photograph of pale pink aggregate after K-feldspar (Ng151). (c) BSE image showing texture composed of cookeite and quartz with cavity (Ng139). (d) Enlargement of Figure 24c, showing that cookeite form spherical aggregate in diameter.

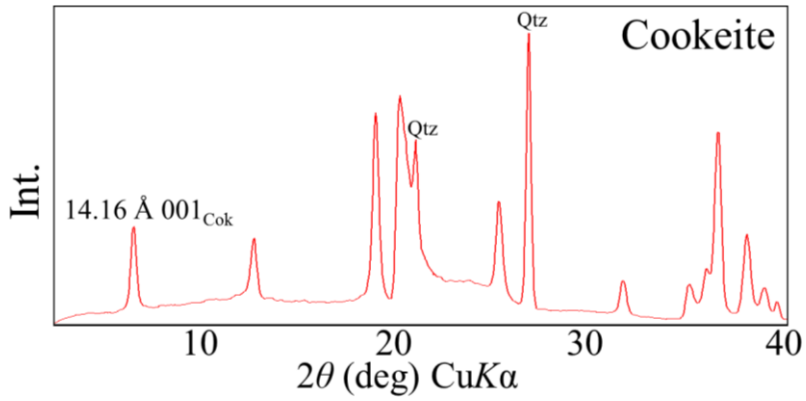

Fig. 25 XRD pattern of cookeite with random orientation, including quartz (Ng139).

Table 7 Average chemical composition of cookeite from the Nagatare pegmatite by EPMA analyses.

Species	Cookeite White	Cookeite White	Cookeite White	Cookeite White	Cookeite White-lightblue	Cookeite White-palepink	Cookeite Palepink	Cookeite Palepink
Sample no.	Ng112	Ng111	Ng102	Ng139	Ng134	Ng132	XN350	Ng153
n	3	4	4	7	7	12	1	1
SiO_2	35.77 (59)	37.11 (21)	36.74 (54)	37.55 (64)	37.39 (60)	36.38 (49)	37.31	39.04
Al_2O_3	44.50 (55)	43.21 (69)	43.34 (84)	46.01 (24)	44.44 (52)	44.53 (99)	42.13	41.49
MgO	N.D.	N.D.	N.D.	N.D.	N.D.	N.D.	N.D.	N.D.
CaO	0.04 (1)	0.05 (2)	0.03 (2)	0.07 (4)	0.09 (5)	0.03 (2)	0.04	0.05
MnO	0.04 (4)	0.05 (3)	0.05 (3)	0.02 (2)	0.04 (4)	0.04 (2)	0.10	0.26
FeO	N.D.	N.D.	N.D.	N.D.	N.D.	N.D.	N.D.	N.D.
Li_2O*	2.77 (1)	2.78 (2)	2.77 (1)	2.88 (3)	2.83 (2)	2.79 (2)	2.75	2.79
Na_2O	N.D.	N.D.	N.D.	N.D.	N.D.	N.D.	N.D.	N.D.
F	0.58 (31)	0.86 (17)	1.05 (22)	0.16 (2)	0.63 (23)	0.57 (21)	1.67	2.19
H_2O*	13.07 (13)	12.98 (15)	12.84 (15)	13.83 (13)	13.34 (20)	13.19 (18)	12.46	12.44
O=F	0.25	0.36	0.44	0.07	0.26	0.24	0.70	0.92
Total	96.53	96.67	96.36	100.45	98.48	97.30	95.77	97.34
Si	3.21 (5)	3.32 (4)	3.30 (6)	3.24 (3)	3.29 (4)	3.24 (6)	3.38	3.47
Al(IV)	0.79 (5)	0.68 (4)	0.70 (6)	0.76 (3)	0.71 (4)	0.76 (6)	0.62	0.53
Al(VIII)	2.00 (0)	2.00 (0)	2.00 (0)	2.00 (0)	2.00 (0)	2.00 (0)	1.99	1.98
Mn	0.00 (0)	0.00 (0)	0.00 (0)	0.00 (0)	0.00 (0)	0.00 (0)	0.01	0.02
Al(VIII)	1.93 (2)	1.89 (1)	1.90 (2)	1.92 (1)	1.90 (1)	1.92 (2)	1.87	1.85
Li	1.00	1.00	1.00	1.00	1.00	1.00	1.00	1.00
Ca	0.00 (0)	0.01 (0)	0.00 (0)	0.01 (0)	0.01 (0)	0.00 (0)	0.00	0.00
F	0.17 (9)	0.24 (5)	0.30 (6)	0.04 (0)	0.17 (7)	0.16 (6)	0.48	0.62
OH	7.83 (9)	7.76 (5)	7.70 (6)	7.96 (0)	7.83 (7)	7.84 (6)	7.52	7.38
Cation sum	8.93	8.89	8.90	8.92	8.91	8.92	8.88	8.85

* Li_2O and H_2O contents were calculated by stoichiometry.

6.2.2 Reactions related to Li chloritization

The montebrasite-amblygonite series from the Nagatare pegmatite contains various alteration minerals: fluorapatite, crandallite, goyazite, waylandite, wardite, viitaniemiite, morinite, muscovite, lepidolite, and cookeite. They are associated with lacroixite, quartz, and topaz. The secondary phosphates form fine veins along cleavages and composition planes of polysynthetic twins in the montebrasite-amblygonite series. There is secondary phosphates vein in the montebrasite-amblygonite series continuously from external cookeite vein (Fig. 26). It indicates that hydrothermal fluid forming cookeite reacted to the montebrasite-amblygonite series, and then formed various secondary phosphates. The detailed mineralogical properties were reported in Shirose & Uehara (2014) (Fig. 27).

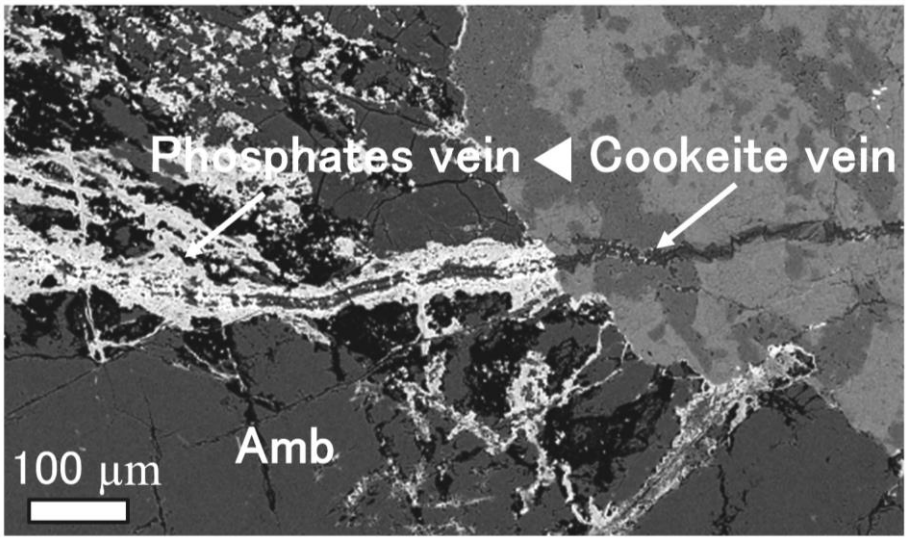

Fig. 26 BSE image of secondary phosphates vein in the montebrasite-amblygonite series (XN162).

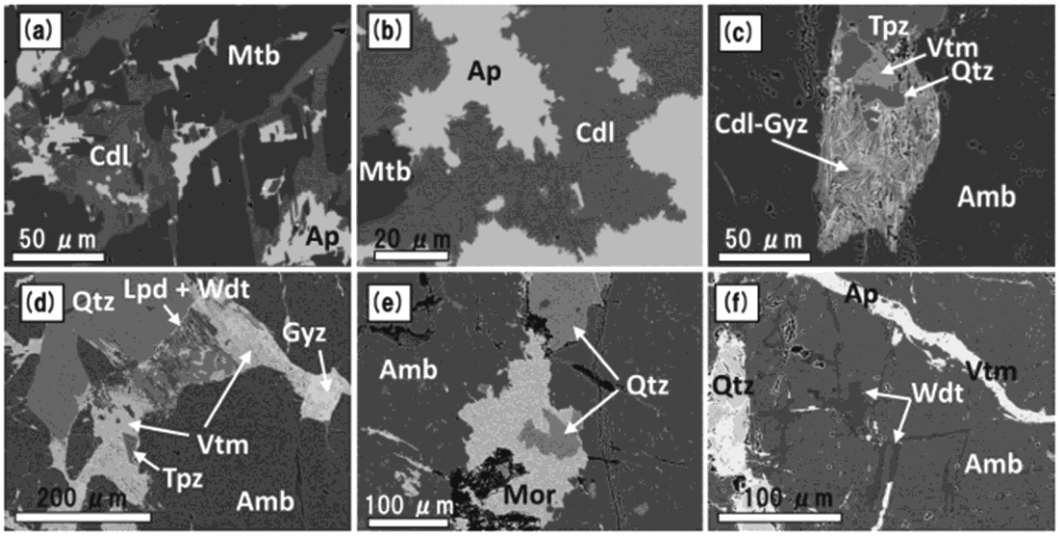

Fig. 27 BSE images of secondary phosphates in the montebrasite and amblygonite (Shirose & Uehara 2014). (a) and (b) Crandallite and apatite forming veinlets along cleavages and composition planes of polysynthetic twins in montebrasite (Ng107). (c) Chemical zoning texture of prismatic crandallite–goyazite series minerals (XN160). (d) Viitaniemiite with high fluorine contents silicates (XN160). (e) Morinite with quartz (XN163). (f) Wardite with veinlets of other phosphates (XN160). Mtb: montebrasite, Amb: amblygonite, Cdl: crandallite, Ap: fluorapatite, Gyz: goyazite, Tpz: topaz, Vtm: viitaniemiite, Qtz: quartz, Lpd: lepidolite, Wdt: wardite, Mor: morinite.

In the Nagatare pegmatite, various Bi phosphates and vanadates occur with the montebrasite-amblygonite series, lepidolite, and albite (Fig. 28). They are considered as same formation stage as Li chloritization. Bi phosphates, including smrkovecite, petitjeanite, and waylandite, were generally confirmed in the montebrasite-amblygonite series with native bismuth, which indicates that Bi phosphates were caused by same formation process as other secondary phosphates except for contribution of Bi from a reaction of native bismuth. The native bismuth is secondary inclusion in the montebrasite-amblygonite series. Bi vanadates occur with cookeite on lepidolite or in voids of albite. Namibite, hechtsbergite, and clinobisvanite were reported in Uehara & Shirose (2013). Furthermore, pucherite and unknown Bi vanadate were also confirmed in this thesis.

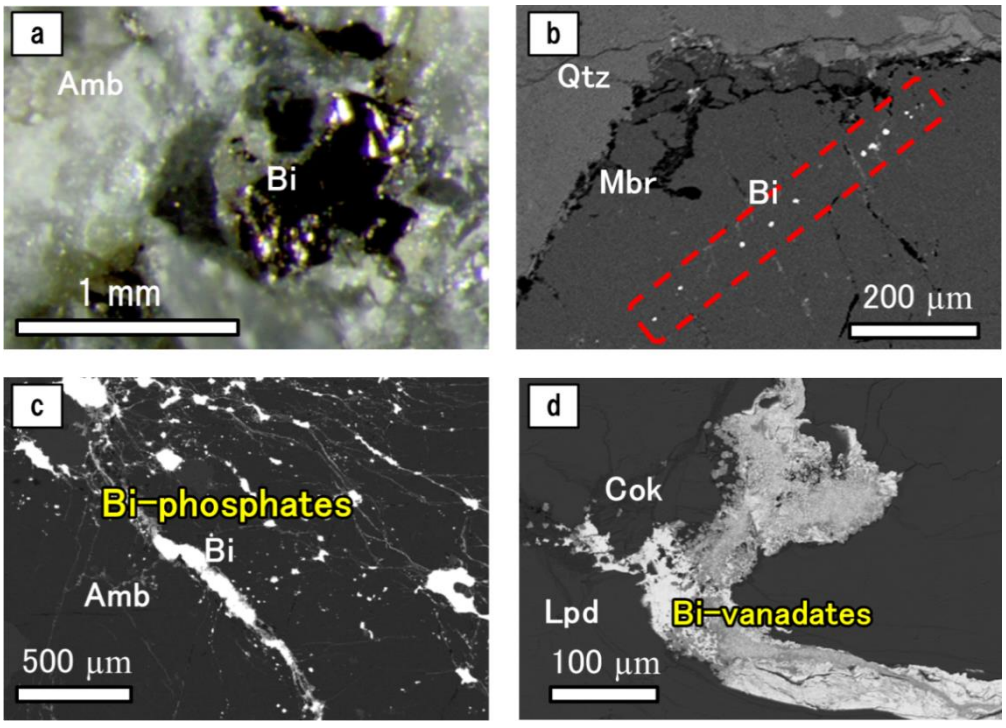

Fig. 28 Appearance and BSE images of Bi minerals. (a) Photomicrograph of native Bi inclusion in amblygonite. (b) Native Bi inclusion in montebrasite as secondary inclusion. (c) Secondary Bi phosphates veinlets around native Bi in amblygonite. (d) Bi vanadates with cookeite on lepidolite.

6.2.3 Sericitization

In the Nagatare pegmatite, the mineral species of pink Li tourmaline are elbaite, fluor-elbaite, and rossmanite (Shirose & Uehara 2013), and often altered to mica partially or perfectly. The aggregates of mica take pseudomorph form of tourmaline as prismatic or radial, and the mica components are fine grains (Fig. 28). Highly altered one is purple to green, dull luster and softer than not suffered tourmaline. In many cases, associated K-feldspar is also altered to mica

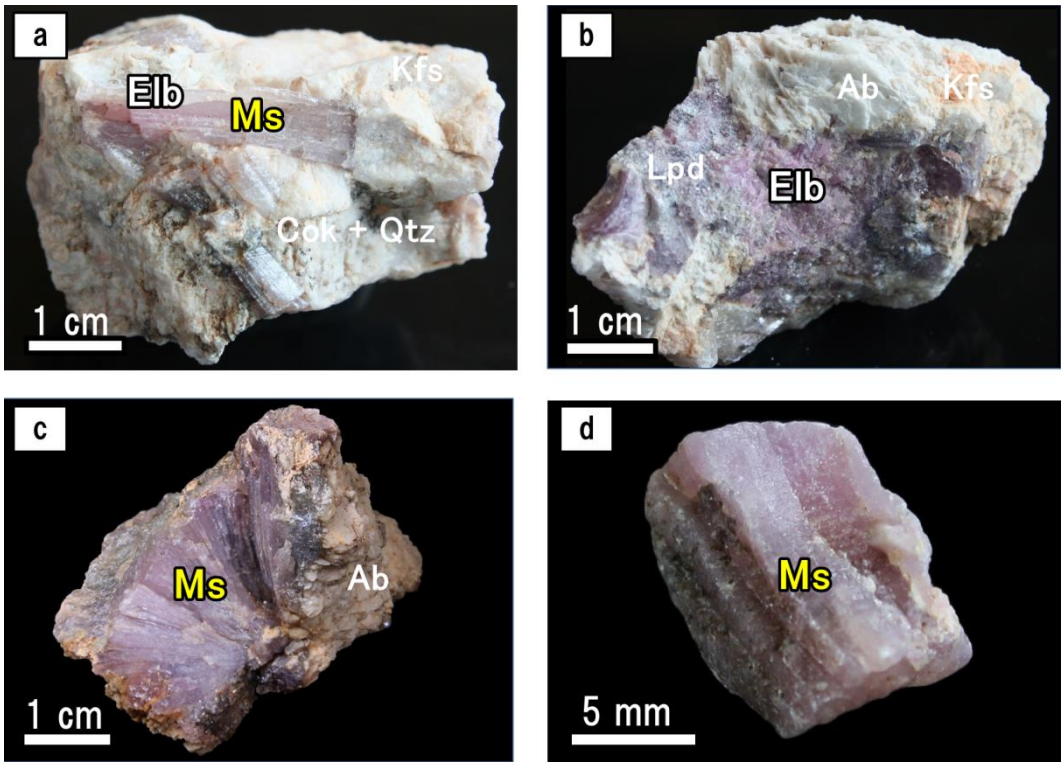

Fig. 29 Appearance of altered Li tourmaline. (a) Partially altered Li tourmaline (Ng10), showing colorless to pale pink and prismatic crystals. The mineral species of Li tourmaline is elbaite. (b) Partially altered Li tourmaline (Ng17), associated with fine lepidolite. The mineral species of Li tourmaline is fluor-elbaite. (c) Perfectly altered Li tourmaline (Ng116), showing radial shape and purple to green color. (d) Perfectly altered Li tourmaline (Ng114), showing prismatic shape and purple color. Ms: muscovite, Elb: elbaite or fluor-elbaite, Kfs: K-feldspar, Cok: cookeite, Qtz: quartz, Ab: albite, Lpd: lepidolite.

In EPMA observation, Li tourmaline were altered to fine grained muscovite, 5-100 μm in width and less than 10 μm in thickness, along fractures with fine grained cookeite, quartz, or topaz (Figs. 30-33). Muscovite sometimes existed with cookeite as fine grained mixtures, and they were confirmed around Li tourmaline relicts in partially replaced specimens (Figs. 30, 31). Associated K-feldspar was also altered to cookeite + quartz, and muscovite + quartz (Fig. 30).

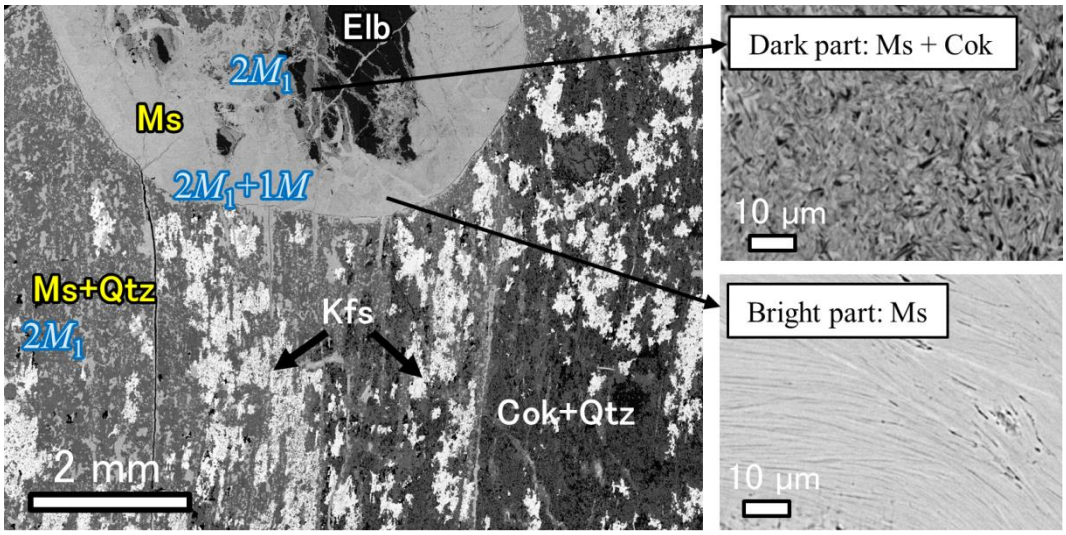

Fig. 30 BSE images of partially altered Li tourmaline with K-feldspar (Ng10). The bright part was composed of coarse muscovite, and the dark part was composed of fine grained muscovite and cookeite, showing that elbaite was undergone multiple alterations. Blue letters show polytypes of muscovite.

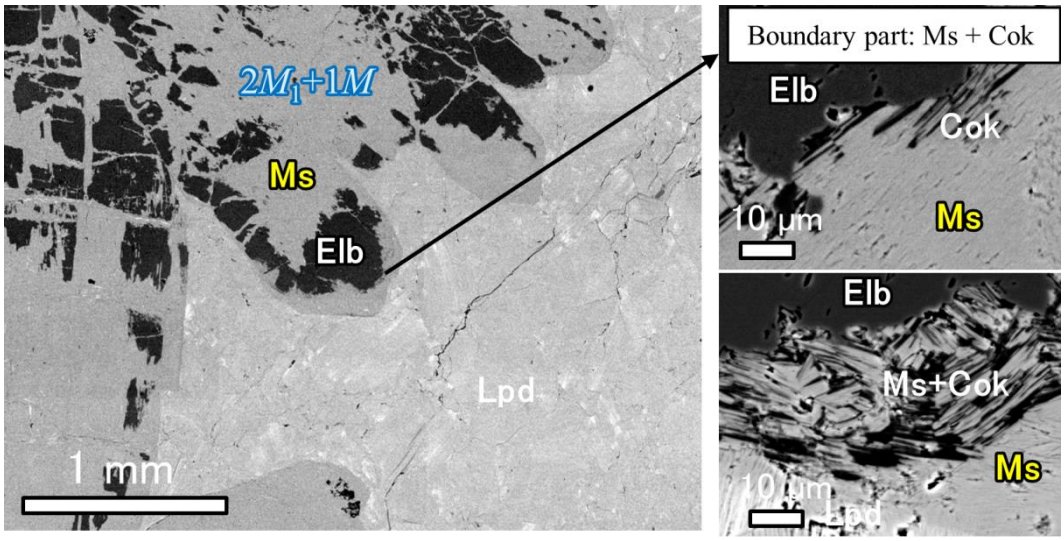

Fig. 31 BSE images of partially altered Li tourmaline with lepidolite (Ng17). There is mixture of muscovite and cookeite around fluor-elbaite relict.

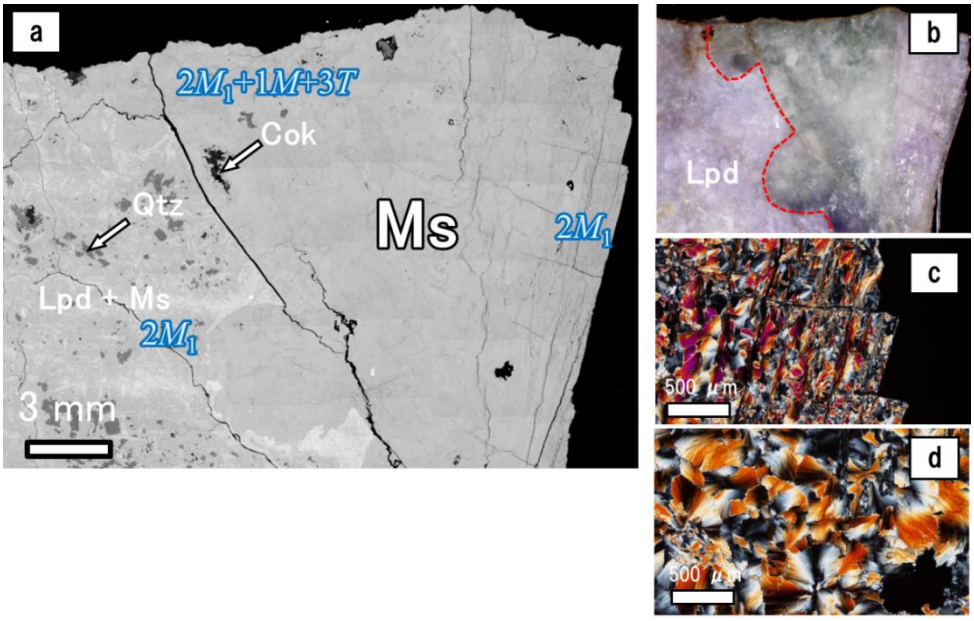

Fig. 32 Photomicrographs of perfectly altered Li tourmaline (Ng116). (a) BSE image of tourmaline pseudomorph. (b) Cross-section of specimen in same area as the BSE image. Red dashed line show boundary of lepidolite and muscovite. (c) Cross-polarized optical photomicrographs of purple part. (d) Cross-polarized optical photomicrographs of green part.

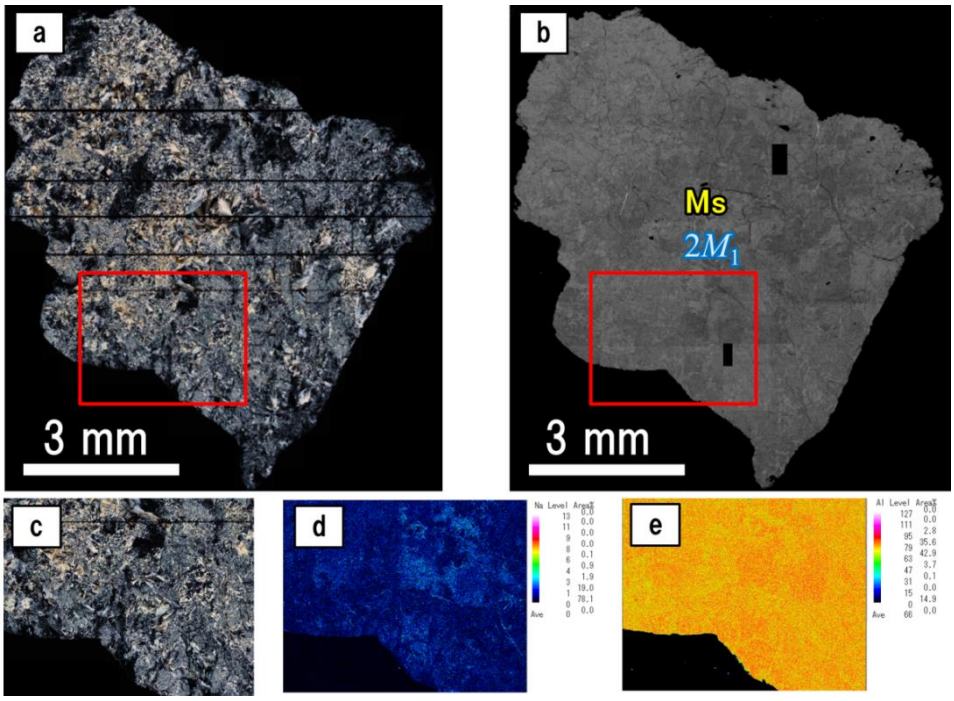

Fig. 33 Photomicrographs of perfectly altered Li tourmaline (Ng114). (a) Cross-polarized optical photomicrographs of specimen. (b) BSE image of same area as Figure 33a. (c) Cross-polarized optical photomicrographs of red frame area in Figure 33a and 33b. (d) X-ray map image of Na *Kα*. (e) X-ray map image of Al *Kα*.

As for perfectly altered Li tourmaline, they were composed of muscovite, and Li tourmaline relict was not confirmed under the EPMA observations (Figs. 32, 33). The macroscopically green part was composed of spherical muscovite aggregates about 500 μm in diameter, without a signature of Li tourmaline fracture observed in the pink part. The representative chemical composition of muscovite in pseudomorph is $K_{0.9}Al_{2.0}(Si_{3.1}Al_{0.9})O_{10}(OH)_{1.9}F_{0.1}$, and the interlayer cations are slightly deficient, which is called as sericite (Fig. 34 and Table 8). However, muscovite after Li tourmaline have inhomogeneous chemical compositions. Some muscovite contain small amount of Na, and they are enriched in Al. Especially for perfectly altered muscovite, they often have inhomogeneous chemical compositions (Fig. 33), and the chemical composition comes up to $Na_{0.60}K_{0.40}Ca_{0.01}Al_{2.0}(Si_{2.74}Al_{1.33})O_{10}(OH)_{1.98}F_{0.02}$ in the highest Na contents part (purple part in specimen Ng114). However, in XRD experiments, Na dominant mica, paragonite or ephesite, was not confirmed.

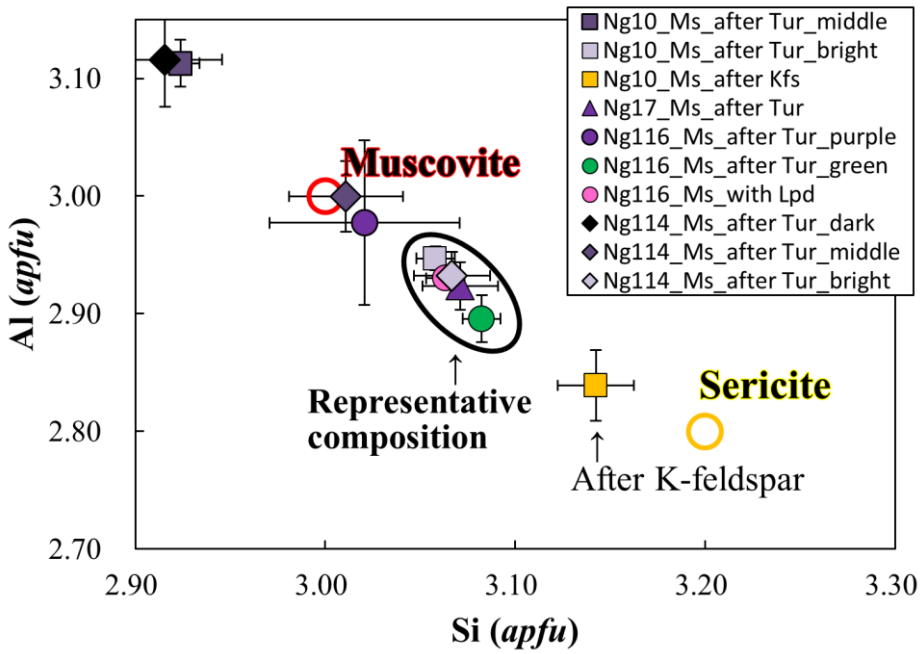

Fig. 34 Chemical compositions of muscovite after Li tourmaline and K-feldspar. Average value and standard deviation are represented by symbols and bars. Colored open circles show ideal value of muscovite and sericite.

Table 8 Average chemical composition of muscovite occurred as pseudomorph from the Nagatare pegmatite by EPMA analyses.

Species	Muscovite In Tur		Muscovite In Kfs		Muscovite In Tur bright		Muscovite In Tur middle		Muscovite In Tur dark	
Sample no.	Ng17		Ng10		Ng10		Ng10		Ng10	
n	8		3		3		2		3	
SiO_2	46.47	(22)	47.33	(31)	46.29	(29)	43.99	(0)	40.37	(53)
Al_2O_3	37.54	(30)	36.28	(30)	37.85	(5)	39.74	(40)	42.87	(82)
MgO	0.00	(1)								
CaO	0.01	(1)	0.01	(1)	0.01	(1)	0.02	(2)	0.04	(2)
MnO	0.10	(3)	0.02	(2)	0.06	(1)	0.02	(1)	0.03	(1)
FeO	0.01	(1)	0.02	(1)	0.02	(2)	0.03	(3)	0.03	(2)
Li_2O*										
Na_2O	0.20	(3)	0.13	(1)	0.29	(4)	0.45	(2)	0.87	(6)
K2O	10.29	(37)	10.33	(5)	10.31	(10)	10.55	(18)	7.40	(38)
Rb2O	0.77	(4)	0.35	(6)	0.22	(3)	0.10	(1)	0.10	(4)
Cs2O	0.15	(2)	0.04	(3)	0.10	(2)	0.06	(4)	0.04	(1)
F	0.47	(11)	0.59	(10)	0.11	(1)	0.16	(5)	0.15	(5)
H_2O*	4.31	(5)	4.24	(5)	4.49	(2)	4.44	(4)	4.35	(3)
O=F	0.20	(5)	0.25	(4)	0.05	(1)	0.07	(2)	0.06	(2)
Total	100.13	(47)	99.09	(6)	99.69	(36)	99.50	(31)	96.17	(33)
Si	3.07	(2)	3.14	(2)	3.06	(1)	2.92	(1)	2.74	(4)
Al(IV)	0.93	(2)	0.86	(2)	0.94	(1)	1.08	(1)	1.26	(4)
Al(VIII)	1.99	(1)	1.98	(1)	2.01	(0)	2.04	(1)	2.16	(3)
Mg	0.00	(0)								
Mn	0.01	(1)	0.00	(0)	0.00	(0)	0.00	(0)	0.00	(0)
Fe	0.00	(0)	0.00	(0)	0.00	(0)	0.00	(0)	0.00	(0)
Li										
Ca	0.00	(0)	0.00	(0)	0.00	(0)	0.00	(0)	0.00	(0)
Na	0.03	(0)	0.02	(2)	0.04	(0)	0.06	(0)	0.11	(1)
K	0.87	(3)	0.87	(0)	0.87	(1)	0.89	(2)	0.64	(3)
Rb	0.03	(0)	0.01	(0)	0.01	(0)	0.00	(0)	0.00	(0)
Cs	0.00	(0)	0.00	(0)	0.00	(0)	0.00	(0)	0.00	(0)
ΣX	0.93	(3)	0.91	(1)	0.92	(1)	0.96	(1)	0.76	(4)
F	0.10	(2)	0.12	(2)	0.02	(0)	0.03	(1)	0.03	(1)
OH	1.90	(2)	1.88	(2)	1.98	(0)	1.97	(1)	1.97	(1)
Cation sum	6.93		6.89		6.93		7.00		6.93	

*H_2O and Li_2O contents were calculated by stoichiometry.
Values in bracket are standard deviations. n: number of analysis spots.

Table 8 (continued)

Species	Muscovite		Muscovite		Muscovite		Muscovite		Muscovite	
	Purple reed shape		Purple coarse		Green coarse		Green prismatic		With Lpd	
Sample no.	Ng116		Ng116		Ng116		Ng116		Ng116	
n	4		4		4		4		3	
SiO_2	45.50	(83)	46.44	(41)	46.51	(34)	46.50	(10)	46.27	(14)
Al_2O_3	38.06	(85)	37.11	(41)	36.94	(49)	37.11	(33)	37.56	(21)
MgO	0.00	(0)	0.00	(0)	0.01	(1)	0.00	(0)	0.00	(0)
CaO	0.01	(1)	0.03	(2)	0.02	(2)	0.02	(1)	0.01	(1)
MnO	0.15	(6)	0.21	(1)	0.21	(7)	0.20	(4)	0.16	(1)
FeO	0.07	(2)	0.13	(6)	0.16	(7)	0.16	(3)	0.06	(1)
Li_2O*										
Na_2O	0.18	(6)	0.17	(1)	0.16	(4)	0.17	(2)	0.16	(4)
K2O	10.74	(17)	10.43	(19)	10.58	(12)	10.35	(16)	10.39	(34)
Rb2O	0.60	(8)	0.71	(7)	0.69	(5)	0.70	(8)	0.73	(10)
Cs2O	0.08	(4)	0.20	(4)	0.13	(4)	0.18	(1)	0.11	(5)
F	0.40	(8)	0.56	(5)	0.65	(7)	0.51	(7)	0.51	(9)
H_2O*	4.33	(5)	4.25	(6)	4.21	(5)	4.28	(6)	4.29	(4)
O=F	0.17	(3)	0.24	(2)	0.27	(3)	0.21	(3)	0.22	(4)
Total	99.93	(21)	100.01	(81)	100.00	(44)	99.96	(57)	100.02	(56)
Si	3.02	(5)	3.08	(1)	3.09	(2)	3.08	(1)	3.06	(1)
Al(IV)	0.98	(5)	0.92	(1)	0.91	(2)	0.92	(1)	0.94	(1)
Al(VIII)	2.00	(2)	1.98	(0)	1.97	(1)	1.98	(0)	1.99	(1)
Mg	0.00	(0)	0.00	(0)	0.00	(0)	0.00	(0)	0.00	(0)
Mn	0.01	(0)	0.01	(0)	0.01	(0)	0.01	(0)	0.01	(0)
Fe	0.00	(0)	0.01	(0)	0.01	(0)	0.01	(0)	0.00	(0)
Li										
Ca	0.00	(0)	0.00	(0)	0.00	(0)	0.00	(0)	0.00	(0)
Na	0.02	(1)	0.02	(0)	0.02	(1)	0.02	(0)	0.02	(0)
K	0.91	(2)	0.88	(2)	0.90	(1)	0.87	(1)	0.88	(3)
Rb	0.03	(0)	0.03	(0)	0.03	(0)	0.03	(0)	0.03	(0)
Cs	0.00	(0)	0.01	(0)	0.00	(0)	0.00	(0)	0.00	(0)
ΣX	0.96	(2)	0.94	(2)	0.95	(1)	0.93	(1)	0.93	(3)
F	0.08	(2)	0.12	(1)	0.14	(2)	0.11	(2)	0.11	(2)
OH	1.92	(2)	1.88	(1)	1.86	(2)	1.89	(2)	1.89	(2)
Cation sum	6.97		6.94		6.94		6.92		6.93	

Table 8 (continued)

Species	Muscovite Dark		Muscovite Middle		Muscovite Bright	
Sample no.	Ng114		Ng114		Ng114	
n	8		3		8	
SiO_2	41.72	(54)	43.11	(41)	43.83	(45)
Al_2O_3	38.13	(54)	36.44	(32)	35.58	(35)
MgO	0.01	(1)	0.01	(1)	0.01	(1)
CaO	0.07	(3)	0.02	(1)	0.01	(1)
MnO	0.06	(2)	0.05	(2)	0.06	(1)
FeO	0.02	(2)	0.04	(1)	0.02	(2)
Li_2O*	0.00	(0)	0.00	(0)	0.00	(0)
Na_2O	1.46	(38)	0.31	(5)	0.26	(6)
K2O	8.52	(58)	9.91	(14)	9.42	(25)
Rb2O	0.30	(6)	0.38	(7)	0.67	(11)
Cs2O	0.02	(2)	0.03	(2)	0.14	(2)
F	0.02	(1)	0.04	(1)	0.04	(2)
H_2O*	4.30	(4)	4.28	(0)	4.27	(3)
O=F	0.01	(0)	0.02	(1)	0.02	(1)
Total	94.63		94.58	5	94.28	64
Si	2.91	(3)	3.01	(3)	3.07	(2)
Al(IV)	1.09	(3)	0.99	(3) 0	0.93	(2) 0
Al(VIII)	2.03	(1)	2.01	(0)	2.00	(1)
Mg	0.00	(0)	0.00	(0)	0.00	(0)
Mn	0.00	(0)	0.00	(0)	0.00	(0)
Fe	0.00	(0)	0.00	(0)	0.00	(0)
Li						
Ca	0.01	(0)	0.00	(0)	0.00	(0)
Na	0.20	(5)	0.04	(1)	0.04	(1)
K	0.76	(5)	0.88	(1)	0.84	(2)
Rb	0.01	(0)	0.02	(0)	0.03	(0)
Cs	0.00	(0)	0.00	(0)	0.00	(0)
ΣX	0.97	(0)	0.94	(0)	0.91	(0)
F	0.00	(0)	0.01	(0)	0.01	(0)
OH	2.00	(0)	1.99	(0)	1.99	(0)
Cation sum	7.01		6.96		6.92	

XRD experiments revealed the polytypes of secondary muscovite to be the combinations of $2M_1$, $2M_1$ + 1*M*, or $2M_1$ + 1*M* + 3*T*, varied with part and specimen (Fig. 35a). The purple part of muscovite after Li tourmaline, sometimes enriched in Al and Na, was $2M_1$ polytype, and muscovite after K-feldspar and the montebrasite-amblygonite series were also $2M_1$ polytype. The polytype of colorless part of muscovite after Li tourmaline was composed of $2M_1$ + 1*M*, whose ratio corresponds to 2:1 (Fig. 35b). The green spherical muscovite after Li tourmaline was the combination of $2M_1$ + 1*M* + 3*T* polytypes with 2:1:1 ratio (Fig. 35b).

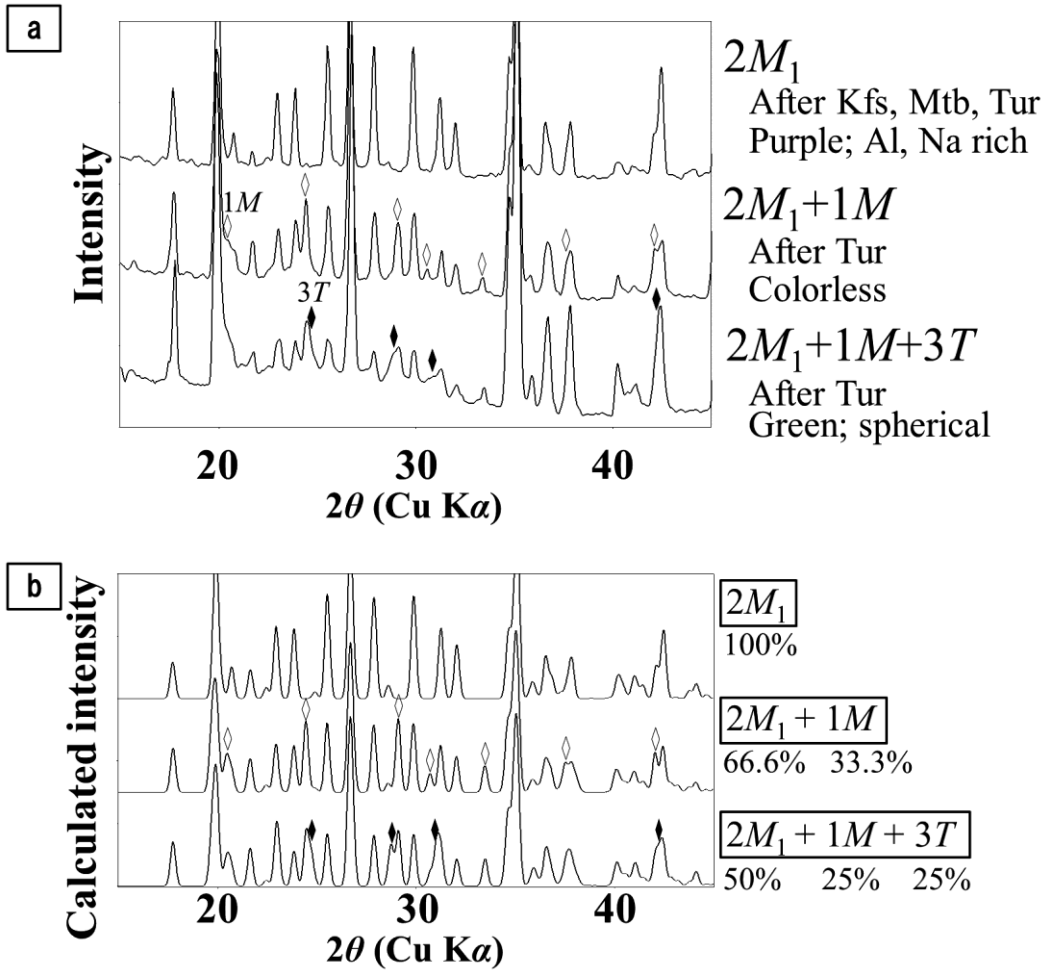

Fig. 35 X-ray diffraction patterns of muscovite composed of different polytypes. Open diamond is characteristic peak of 1*M* polytype, and solid diamond is that of 3*T* polytype. (a) Measured XRD patterns of muscovite with random orientation. Specimens are green part in Ng 114, white part in Ng10 and green part in Ng 116 in descending order. (b) Calculated XRD patterns of muscovite with mixed polytypes, referenced as follows; $2M_1$ (Liang & Hawthorne 1996), 1*M* (Plançon *et al*. 1985), and 3*T* (Güven & Burnham 1967).

In TEM observation, the ion-milled samples of partially altered Li tourmaline were used for investigating microtextures of Li tourmaline and muscovite (Fig. 36a). Figure 37 shows the SAED patterns of muscovite and fluor-elbaite, and they had no orientation relationships. Their grain boundary was clear and corresponding to the planes of Li tourmaline. For muscovite, they formed long sericite packet (>100 nm) along *c* axis with single polytype. Layer-stacking sequences of each polytype (1*M*, 2M_1, 3*T*) in muscovite were directly observed as high resolution TEM images. (Fig. 38). Though stacking disorder was slightly confirmed in some packets, ordered parts were dominant in each polytype.

Li tourmaline mainly had fracture-controlled sericitization, and they were partially or perfectly replaced by muscovite. Ahn & Buseck (1998) observed partially sericitized dark-grey olenite (Al tourmaline) from a pegmatite at the Black Hills using HRTEM, and discussed the formation process. In their observations, tourmaline and muscovite had oriented relationships, that (001) plane of muscovite was parallel to *c* axis of tourmaline. However, no relationship was confirmed in the orientations of muscovite and Li tourmaline in this thesis. Though Al tourmaline and Li tourmaline were very similar that they had fracture-controlled sericitization at early stage of alterations, muscovite after Li tourmaline was different in the variations of texture such as mixture with cookeite, chemical differences, and polytypes. Sericitization of Li tourmaline is described as follow reaction:

$Na_{0.5}Al_{1.75}Li_{1.25}Al_6Si_6O_{18}(BO_3)_3(OH)_3(OH) + 3K^+ + 2SiO_2 + 9H_2O$

Elbaite Quartz

$\rightarrow\ 3KAl_2Si_3AlO_{10}(OH)_2 + 3B(OH)_4^- + 4H^+ + Na^+ + Li^+$

Muscovite

which explains that Li tourmaline reacted with hydrothermal fluids that possess high K^+ activity, weakly acidity, and sufficient silica. The variations of polytype and chemical composition of

muscovite indicate that Li tourmaline had multiple hydrothermal alterations with different temperature and chemical condition. In general, $2M_1$ polytype is formed at higher temperature than 1*M* or 1*M*d polytypes, and the ratio of 1*M* polytype increases in response to a decrease of temperature and a gap from muscovite composition to illite. Green spherical muscovite with 3*T* polytype contained minor amount of Fe in contrast to purple muscovite, which was formed at lower temperature. Besides, the association of $2M_1$ polytype and the sericite composition indicates that the muscovite after Li tourmaline was formed at hydrothermal conditions, not weathering. Cookeite + quartz after K-feldspar were formed in Li rich environment. Cookeite after Li tourmaline was also formed in Li rich environment, or as an intermediate product in sericitization. In the former case, cookeite and muscovite existed in equivalent condition at early stage. The trigger of sericitization for Li-tourmaline is the breakdown of K-feldspar releasing K^+ and increasing $a_{[K^+]/[H^+]}$ of aqueous fluid. In addition, Al-rich and Na-poor pink Li tourmaline is preferentially replaced.

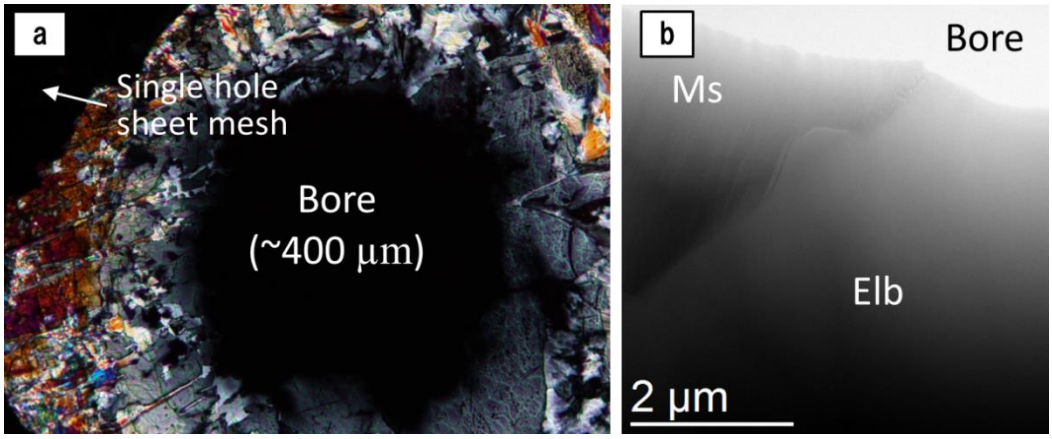

Fig. 36. Photomicrograph of ion-milled sample. (a) Cross-polarized optical photomicrographs of ion-milled area. (b) STEM BF image of muscovite and fluor-elbaite.

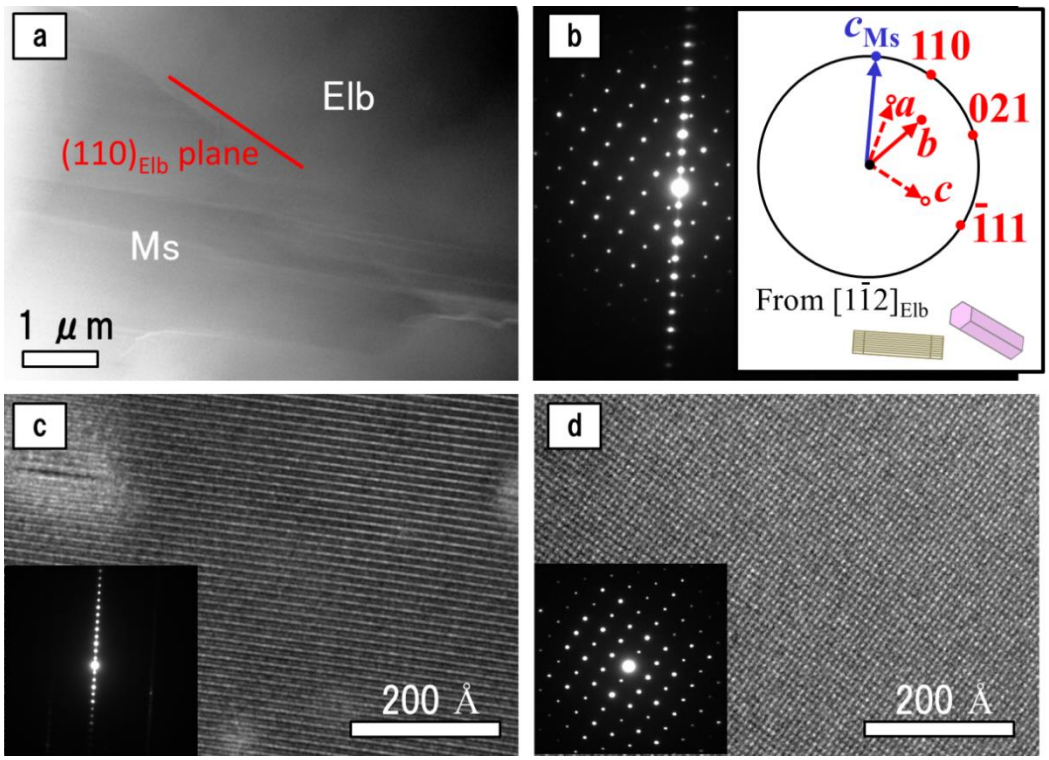

Fig. 37. Orientation relationships of muscovite and fluor-elbaite (Ng17). (a) STEM BF image of boundary are of muscovite and fluor-elbaite. The boundary plane was (110) plane of fluor-elbaite. (b) SAED pattern of boundary area. (c) HRTEM image of muscovite and the SAED pattern. (d) HRTEM image of fluor-elbaite and the SAED pattern.

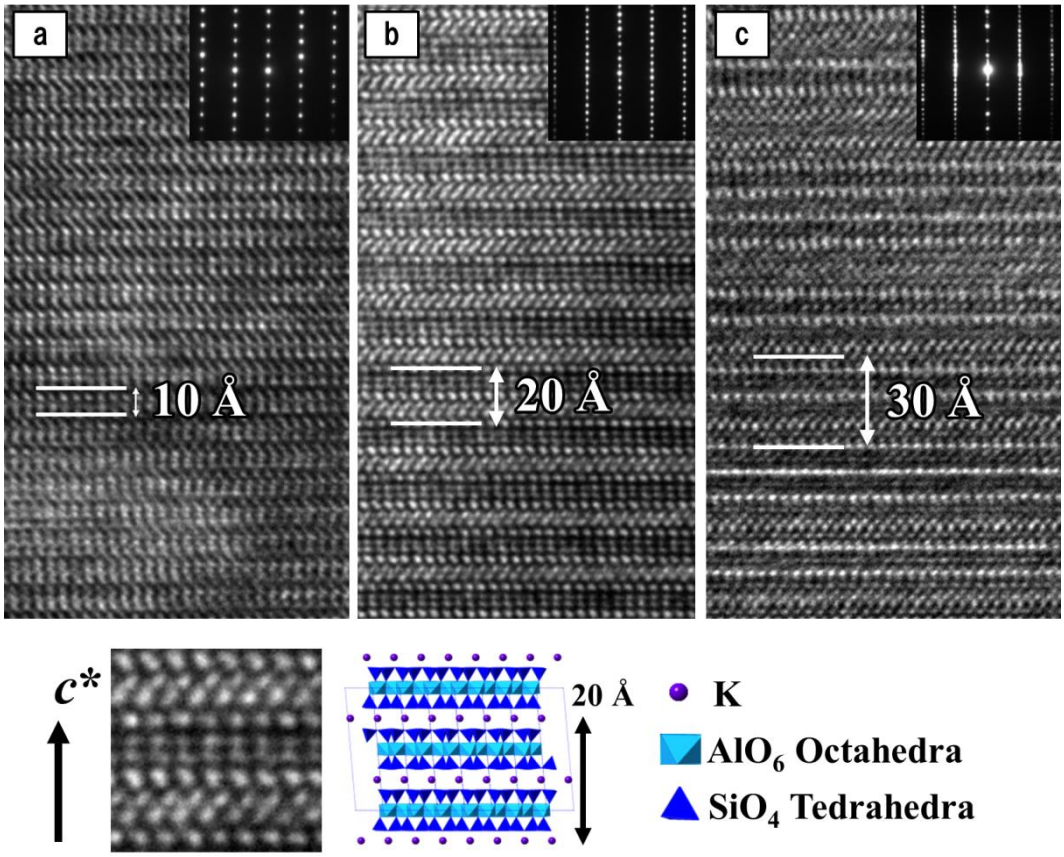

Fig. 38 High resolution TEM images of muscovite after Li tourmaline on each polytype, and the electron diffraction patterns along the *c* axis of muscovite (Ng17). (a) Muscovite 1*M* with 10 Å periodicity. (b) Muscovite $2M_1$ with 20 Å periodicity. (c) Muscovite 3*T* with 30 Å periodicity. Crystal structure data was referenced from muscovite with $2M_1$ polytype (Liang & Hawthorne 1996).

6.2.4 Smectitization

The smectite group minerals are divided to dioctahedral and trioctahedral smectite groups. Beidellite is dioctahedral smectite that the tetrahedral Si^{4+} is partially replaced by Al^{3+}, and montmorillonite is dioctahedral smectite that the octahedral Al^{3+} is partially replaced by Mg^{2+}. They have exchangeable cation such as Ca^{2+}, Na^{+}, and K^{+}. The occurrence of montmorillonite (or beidellite) with red color red was reported from the Nagatare pegmatite by Takimoto (1937). The red montmorillonite occurs in Li rich part of the pegmatite, and has friable and swelling properties. Takimoto (1937) reported that the red clays could be derived from albite based on the occurrence. However, the mineral paragenesis indicates that they are derived from alteration of petalite (Figs. 39a, b), and the associated albite with lath shape has little alteration. In addition to red clay after petalite, pink friable clay occurs as pseudomorph of K-feldspar (Fig. 39d). The red and pink clays have cleavage-like pseudomorph texture (Figs. 39c, d). The texture of red clay was also observed in secondary electron images (Fig. 40). The clays had linear structure like cleavages of petalite (Fig. 40a), which were composed of fine grained wavy plates below 1 μm (Fig. 40d). XRD experiments and EMPA analyses revealed that the red swelling clay minerals were beidellite and montmorillonite after petalite, and pink clay minerals were beidellite associated with cookeite and tosudite after K-feldspar.

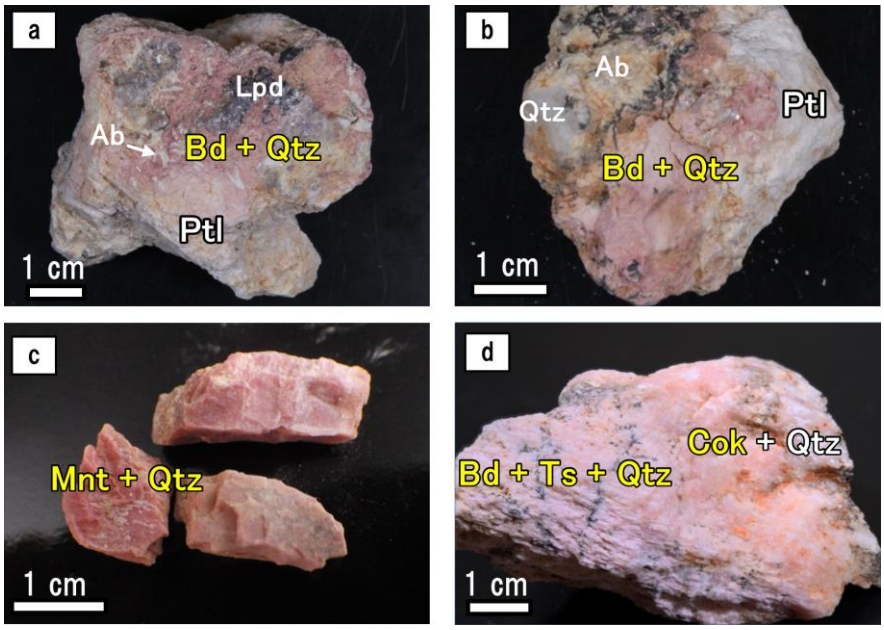

Fig. 39 Appearances of smectite group minerals. (a) Red beidellite-montmorillonite of partially altered petalite, associated with albite and lepidolite (XN350). (b) Red beidellite-montmorillonite of partially altered petalite, associated with albite and quartz (XN351). (c) Perfectly altered specimen composed of montmorillonite-beidellite and quartz (Ng146). (d) Pink beidellite-montmorillonite after K-feldspar associated with cookeite, Li tosudite, and quartz (Ng132). Bd: beidellite, Mnt: montmorillonite, Ptl: petalite, Ab: albite, Ldp: lepidolite, Qtz: quartz, Ts: Li tosudite, Cok: cookeite.

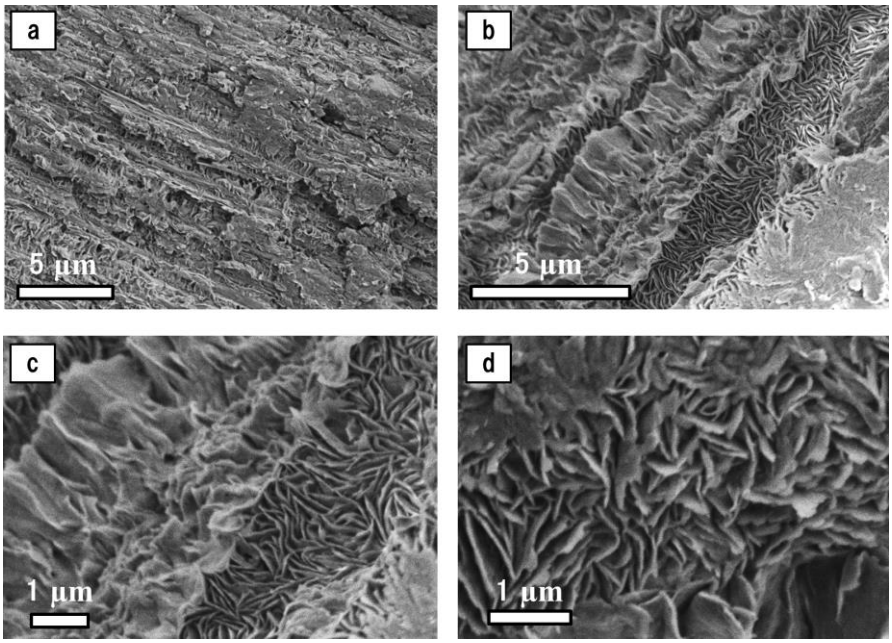

Fig. 40 Secondary electron images of fracture surface of montmorillonite-beidellite (Ng146). (a) Montmorillonite-beidellite showing linear structures like cleavage. (b) The linear structure composed of fine plates. (c) Enlarged image of Figure 40b. (d) The montmorillonite-beidellite was made of fine grained curved plates below 1 µm.

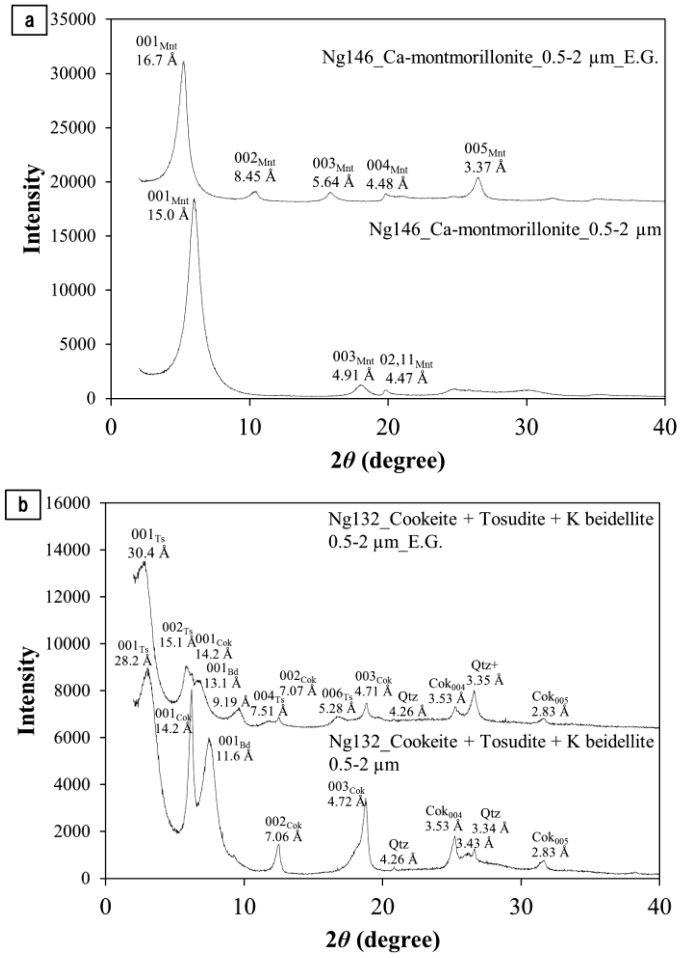

Fig. 41 Powder XRD patterns of the red clay and the pink clay with orientation after the elutriation. (a) Ca montmorillonite with red color (Ng146), shown with the patterns of ethylene glycol treated samples. (b) Association of cookeite, Li tosudite, and K beidellite with pink color (Ng 132), shown with the patterns of ethylene glycol treated samples.

Smectite group minerals generally have basal reflection around 15 Å in an XRD pattern, and the value depends on the interlayer cations and the humidity. The value of basal distance increases by treatment of ethylene glycol. As for the red and pink clay minerals, the basal distances of 15.0, 28.2, and 11.6 Å increased by ethylene glycol treatment (Fig. 41), which indicates they had smectite layer. The 28.2 Å peak derives from mixed layer of cookeite (~14 Å) and smectite layers (~15 Å); it is called as Li tosudite (regular mixed layer mineral with cookeite and smectite). The 11.6 Å peak is considered as the basal reflection of K beidellite, that the interlayer cations are occupied by high charge K^+. However, it is difficult to distinguish high

charge K beidellite and mixed layer minerals of illite and smectite caused by association of Li tosudite and cookeite.

In EPMA analyses, there was difference in alteration texture in each alteration grade. Partially altered petalite had veinlet texture of beidellite-montmorillonite along cleavages of petalite, associated cookeite and quartz (Fig. 42a). The strong altered part of partially altered specimen was composed of the K beidellite veinlet and massive Ca beidellite with quartz. It indicates that K beidellite was formed along fracture and cleavage of petalite at early stage, and the relict of petalite was strongly dissolved with formation of massive Ca beidellite at late stage (Fig. 42b). Perfectly altered aggregate without relict was made of Ca montmorillonite and quartz, with homogeneous chemical composition (Fig. 42c). K beidellite after K-feldspar with 11.6 Å peak was associated with Li tosudite, cookeite, and quartz. The associated pink translucent part was composed of cookeite and quartz written as a cookeite aggregate in section 6.2.1., while pink cloudy part was mainly composed of K beidellite enriched in K and quartz with Li tosudite and cookeite (Figs. 42d, 43). The mineral species of smectite from the Nagatare Li pegmatite were K beidellite, Ca beidellite, and Ca montmorillonite in the average chemical compositions (Figs. 44, 45, Table 9). They were formed at different formation stages or environments, and the alteration reactions were not in equivalent state. K beidellite occurred as veinlet along a fracture of petalite, or replacement aggregate after K-feldspar, while Ca beidellite or Ca montmorillonite occurred as perfectly replacement aggregate after petalite (Fig. 45). The ternary diagram of dioctahedral cations of smectite was characterized by Güven (1988) and divisions were established by Schultz (1969). In the diagram, the chemical compositions of smectite group minerals from Nagatare Li pegmatite correspond to “beidellite” and “Tatatilla-type montmorillonite” (Fig. 46). They generally occur from bentonites derived from alteration of acidic rocks (Christidis 1997).

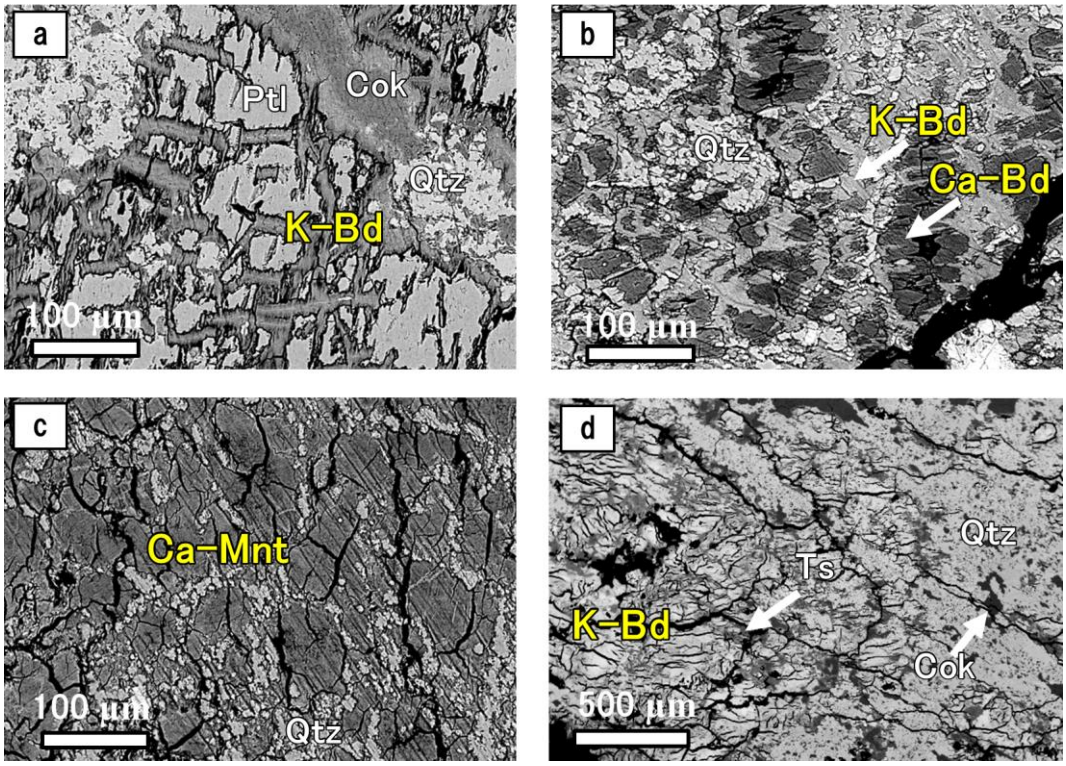

Fig. 42 BSE images of montmorillonite and beidellite. (a) K beidellite veinlets with partially altered petalite (XN350). (b) Two different beidellite in strongly altered part of partially altered petalite (XN351). (c) Perfectly altered specimen composed of Ca montmorillonite and quartz (Ng146). (d) K beidellite after K-feldspar with Li tosudite, cookeite, and quartz (Ng132).

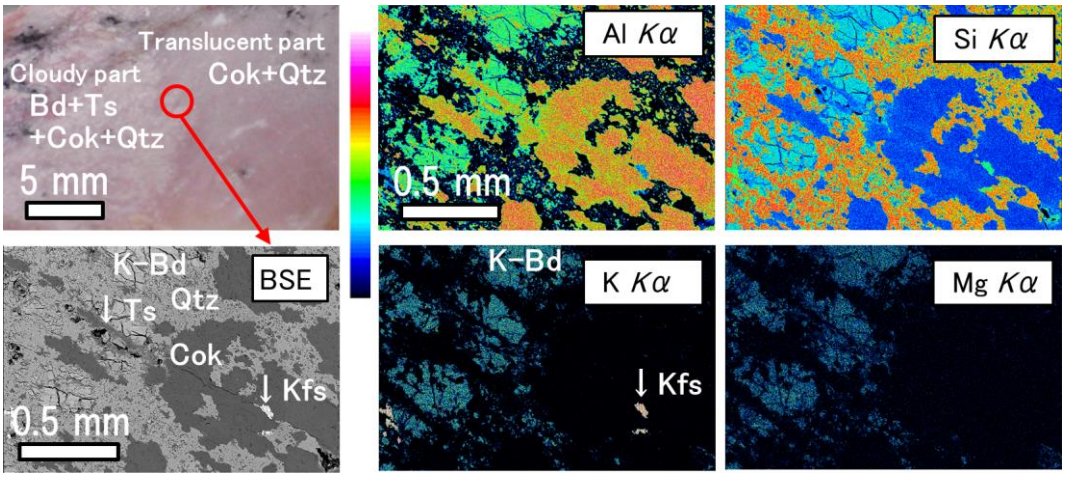

Fig. 43 X-ray map images of K beidellite with Li tosudite, cookeite, and quartz in specimen Ng132 (photograph of section, BSE image, Al*K*α, Si*K*α, K*K*α, and Mg*K*α). Red circle indicates the around part of analytical area.

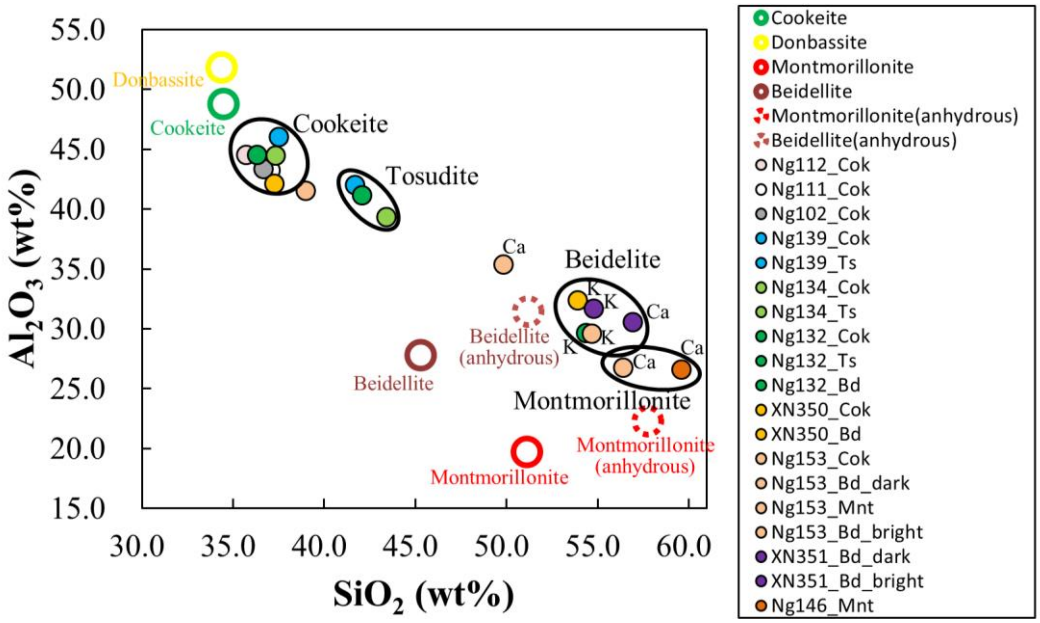

Fig. 44 Chemical compositions of cookeite, Li tosudite, beidellite, and montmorillonite in 10 specimens. Plotted symbol shows average value of minerals in the specimens. Open circle shows ideal value of donbassite, cookeite, beidellite, and montmorillonite. Dashed circle shows the anhydrous value of smectite.

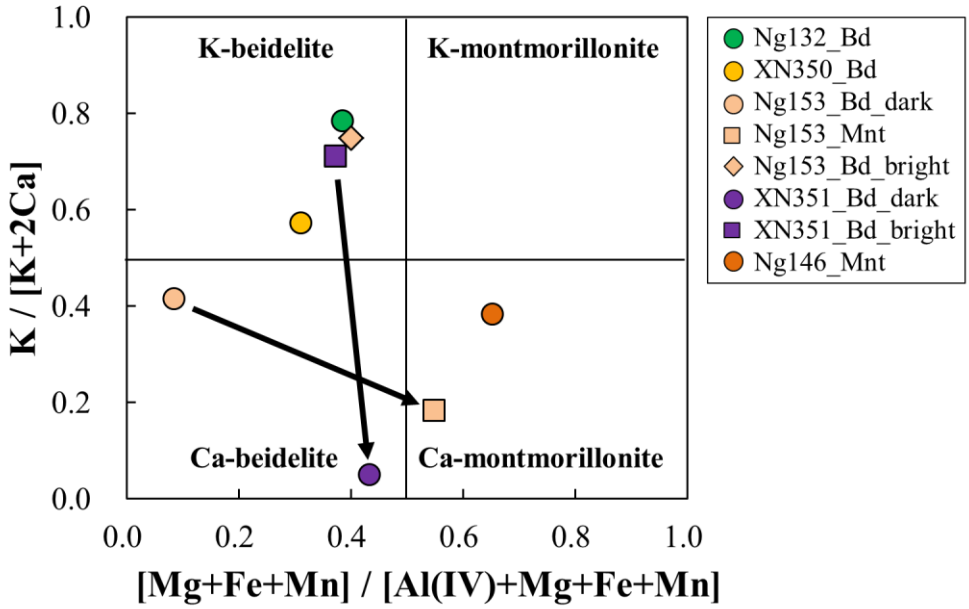

Fig. 45 Chemical compositions of smectite group minerals and the division of the minerals species, based on the interlayer cations, montmorillonite substitution, and beidellite substitution. Average values of each smectite group minerals in the specimens are represented by symbols. Black arrows show the gap from veinlet part to massive part in the specimens. K beidellite occurred as veinlet along a fracture of petalite, or replacement aggregate after K-feldspar, while Ca beidellite or Ca montmorillonite occurred as perfectly replacement aggregate after petalite.

Table 9 Average chemical composition of smectite from the Nagatare pegmatite by EPMA analyses.

Species	K-beidellite	K-beidellite	K-montmorillonite	K-beidellite	Ca-beidellite
Sample no.	Ng132	XN350	Ng146	XN351	XN351
n	5	6	5	3	3
SiO_2	54.40 (47)	53.97 (192)	59.65 (86)	54.85 (24)	56.97 (101)
Al_2O_3	29.64 (53)	32.39 (125)	26.60 (44)	31.67 (79)	30.54 (133)
MgO	2.51 (10)	1.59 (31)	3.45 (24)	1.73 (17)	3.06 (15)
CaO	0.91 (7)	0.57 (15)	0.62 (7)	0.68 (3)	0.87 (5)
MnO	0.44 (5)	1.31 (52)	1.90 (14)	0.88 (17)	0.05 (5)
FeO	0.76 (9)	0.13 (7)	0.60 (7)	1.73 (28)	0.11 (1)
Na_2O	N.D.	N.D.	N.D.	N.D.	N.D.
K_2O	5.57 (22)	1.28 (49)	0.64 (10)	2.79 (27)	0.08 (1)
F	0.31 (7)	0.32 (15)	0.25 (9)	0.22 (5)	0.21 (4)
H_2O*	4.50 (7)	4.49 (18)	4.64 (4)	4.61 (3)	4.63 (11)
O=F	0.13 (3)	0.13 (6)	0.11 (4)	0.09 (2)	0.09 (2)
Total	98.92	95.91	98.25	99.06	96.44
Si	3.51 (2)	3.49 (7)	3.76 (2)	3.49 (2)	3.61 (2)
Al(IV)	0.49 (2)	0.51 (7)	0.24 (2)	0.51 (2)	0.39 (2)
Al(VIII)	1.76 (1)	1.96 (4)	1.73 (2)	1.86 (2)	1.89 (2)
Mg	0.24 (1)	0.15 (3)	0.32 (2)	0.16 (2)	0.29 (2)
Mn	0.02 (0)	0.07 (3)	0.10 (1)	0.05 (1)	0.00 (0)
Fe	0.04 (0)	0.01 (0)	0.03 (0)	0.09 (1)	0.01 (0)
K	0.46 (2)	0.11 (4)	0.05 (1)	0.23 (2)	0.01 (0)
Ca	0.06 (0)	0.04 (1)	0.04 (0)	0.05 (0)	0.06 (0)
F	0.06 (1)	0.07 (3)	0.05 (2)	0.04 (1)	0.04 (1)
OH	1.94 (1)	1.93 (3)	1.95 (2)	1.96 (1)	1.96 (1)
Cation sum	6.59	6.33	6.28	6.44	6.25
Mg+Fe+Mn	0.31	0.23	0.46	0.30	0.30
Mg+Fe+Mn/A	0.39	0.31	0.65	0.37	0.43
K+2Ca	0.58	0.18	0.13	0.32	0.12
K/(K+2Ca)	0.78	0.57	0.38	0.71	0.05

* H_2O contents were calculated by stoichiometry.

Table 9 (continued)

Species	Ca-beidellite	K-beidellite	Ca-montmorillonite
Sample no.	Ng153	Ng153	Ng153
n	10	3	4
SiO_2	49.88 (198)	54.74 (172)	56.45 (106)
Al_2O_3	35.35 (118)	29.57 (385)	26.72 (126)
MgO	0.47 (21)	2.43 (90)	3.25 (52)
CaO	0.28 (11)	0.60 (19)	1.36 (7)
MnO	0.22 (10)	0.48 (4)	0.46 (50)
FeO	0.02 (2)	0.03 (2)	0.04 (3)
Na_2O	N.D.	N.D.	N.D.
K_2O	0.33 (16)	2.92 (32)	0.57 (43)
F	0.46 (32)	0.42 (20)	0.22 (6)
H_2O*	4.25 (26)	4.39 (13)	4.45 (13)
O=F	0.19 (13)	0.18 (8)	0.09 (2)
Total	91.05	95.41	93.44
Si	3.35 (7)	3.58 (15)	3.71 (3)
Al(IV)	0.65 (7)	0.42 (15)	0.29 (3)
Al(VIII)	2.15 (4)	1.85 (13)	1.78 (2)
Mg	0.05 (2)	0.24 (9)	0.32 (6)
Mn	0.01 (1)	0.03 (0)	0.03 (3)
Fe	0.00 (0)	0.00 (0)	0.00 (0)
K	0.03 (1)	0.24 (3)	0.05 (4)
Ca	0.02 (1)	0.04 (1)	0.10 (1)
F	0.10 (7)	0.09 (4)	0.05 (1)
OH	1.90 (7)	1.91 (4)	1.95 (1)
Cation sum	6.26	6.41	6.27
Mg+Fe+Mn	0.06	0.27	0.35
Mg+Fe+Mn/A	0.09	0.40	0.55
K+2Ca	0.07	0.33	0.24
K/(K+2Ca)	0.42	0.75	0.18

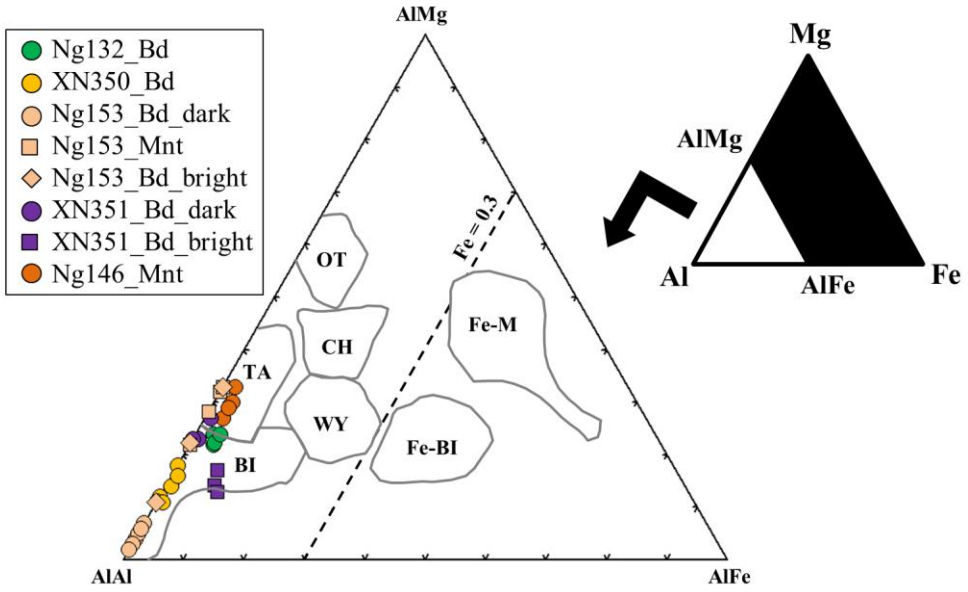

Fig. 46 Ternary diagram of the main octahedral cations in smectite after Güven (1988). The smectites derived from acidic rocks are projected in the fields of beidellite and Tatatilla-type montmorillonite. Abbreviations: Bi: beidellite, TA: Tatatilla montmorillonite, CH: Chambers montmorillonite, OT: Otay montmorillonite, WY: Wyoming montmorillonite, Fe-Bi: Fe-rich beidellite, Fe-M: Fe-rich montmorillonite.

Smectitization of petalite is described as follow reaction:

$2LiAlSi_4O_{10} + 0.4(Mg^{2+},Ca^{2+},K^{+},Fe^{2+},Mn^{2+}) + 2H^{+}$

Petalite

$\rightarrow (Ca, K)_{0.2}(Al, Mg, Fe, Mn)_{2.2}(Si_{3.6}Al_{0.4})O_{10}(OH)_2 + 2Li^{+} + 4SiO_2$

Ca montmorillonite Quartz

which explains that petalite reacted with weakly acidic hydrothermal fluids, and released Li^{+} to the fluids.

Furthermore, smectitization of K-feldspar is described as follow reaction:

$2KAlSi_3O_8 + 0.4(Mg^{2+},Ca^{2+},Fe^{2+},Mn^{2+}) + H_2O$

K-feldspar

$\rightarrow (K, Ca)_{0.5}(Al, Mg, Fe, Mn)_{2.1}(Si_{3.5}Al_{0.5})O_{10}(OH)_2 + 1.5K^{+} + 2.5SiO_2$

K beidellite Quartz

which indicates that weakly acidic hydrothermal fluids altered K-feldspar to K beidellite, and K^{+} was released to the fluid. The fluids described in above reactions are identical in weakly acidity and content of Ca, Mg, Fe, and Mn, leaching Li^{+} and K^{+} from petalite and K-feldspar. In these reactions, silica was released as quartz in the reactions, and consistent with the observed textures.

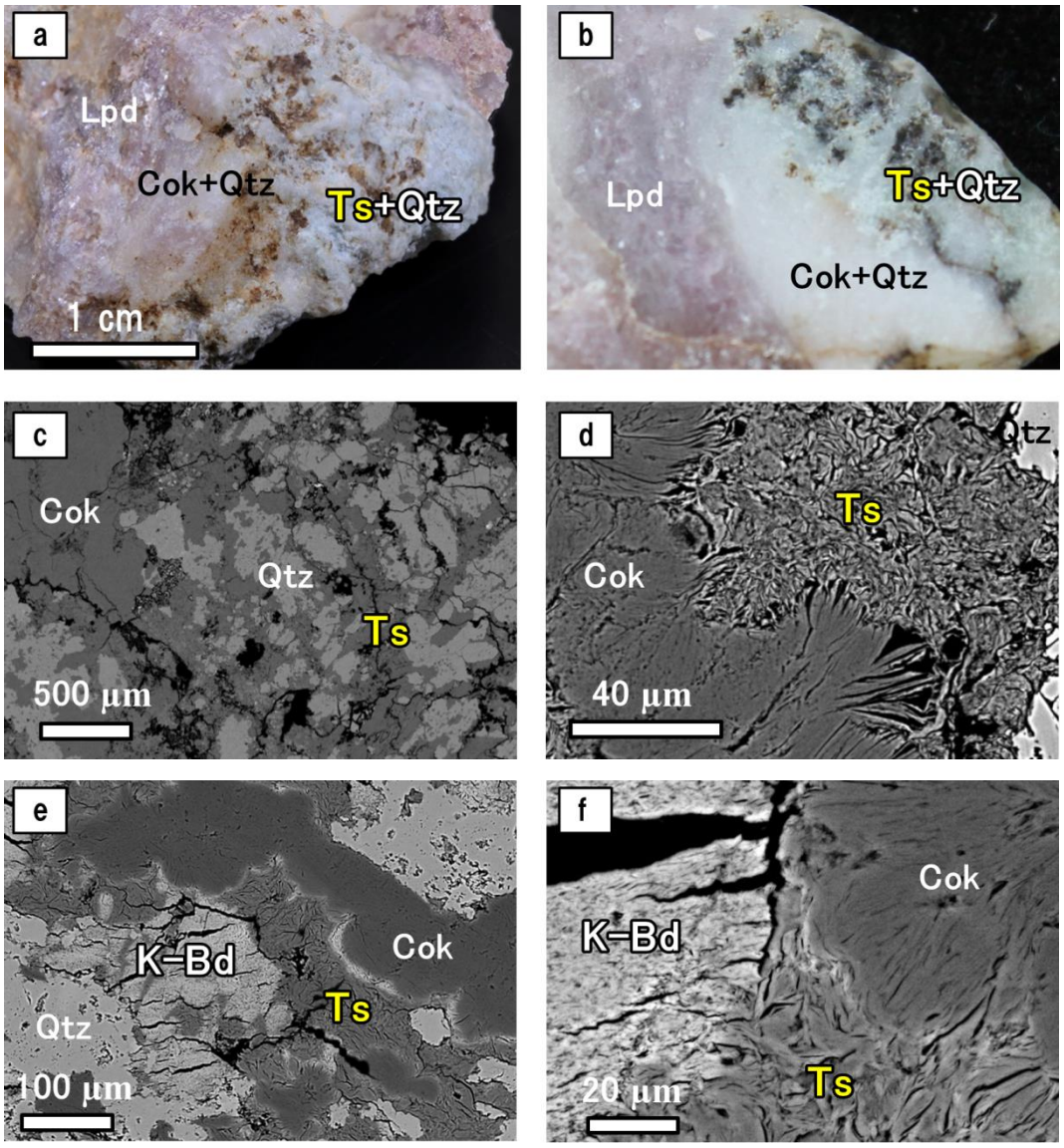

Fig. 47 Appearance and BSE images of Li tosudite. (a) Photograph of light blue Li tosudite with white cookeite + quartz aggregate (Ng134). (b) Section of Figure 47a. (c) BSE image of Li tosudite with cookeite and quartz (Ng134). (d) Enlarged image of Figure 47c. (e) BSE image of Li tosudite with K beidellite, cookeite, and quartz (Ng132). (f) Enlarged image of Figure 47e.

K beidellite after K-feldspar occurred with Li tosudite, cookeite, and quartz. Tosudite is regularly mixed layer mineral composed of dioctahedral chlorite layer and dioctahedral smectite layer, and in this case, it is Li tosudite made of dioctahedral chlorite layer of cookeite layer. In addition to above pink clay mineral after K-feldspar (Ng132), light blue clay minerals also contained Li tosudite (Fig. 47). The light blue clay continuously associated with white

aggregates, composed of cookeite and quartz as in section 6.2.1 (Fig. 47b). Li tosudite was finer grained than cookeite, and massive aggregates with random crystal orientations (Fig. 47d). In pink clay mineral, Li tosudite closely associated with cookeite and K beidellite with continuously grain boundaries. The grain size of Li tosudite was intermediate range of K beidellite and cookeite. Chemical compositions of Li tosudite were shown in Table 10, with intermediate value in smectite and cookeite (Fig. 44), whose smectite layer corresponds to Ca beidellite and Ca montmorillonite. Their appearance colors are derived from minor Fe and Mn contents. The internal texture and chemistry show that Li tosudite was formed from cookeite; they were not directly derived from K-feldspar. Smectitization of cookeite is described as follow reaction:

$$LiAl_2Al_2Si_3AlO_{10}(OH)_2(OH)_6 + 0.6(Mg^{2+},Ca^{2+},K^{+},Fe^{2+},Mn^{2+}) + 4SiO_2$$

Cookeite

$$\rightarrow\ 2(Ca, K)_{0.1}(Al, Mg, Fe, Mn)_{2.2}(Si_{3.5}Al_{0.5})O_{10}(OH)_2 + Li^{+} + 2H_2O$$

Ca beidellite layer in Li tosudite

which explains that cookeite reacted with weakly acidic hydrothermal fluids. This is same reaction as smectitization of petalite and K-feldspar in cation exchange with transition to smectite layer. At early stage, K-feldspar was partially altered to cookeite + quartz in equivalent reaction, and at late stage, the relict of K-feldspar was replaced to K beidellite with partial smectitization of cookeite in pink clay minerals. In the result, the mineral associations as shown in Figure 47e, K beidellite, Li tosudite, cookeite, and quartz, were formed as last products. In the case of light blue clay, the cookeite + quartz aggregate was partially altered to Li tosudite.

Table 10 Average chemical composition of Li tosudite from the Nagatare pegmatite by EPMA analyses.

Species	Li-tosudite Cok/Ca-Bd	Li-tosudite Cok/Ca-Bd	Li-tosudite Cok/Ca-Mnt
Sample no.	Ng132	Ng139	Ng134
n	6	3	5
SiO_2	42.12 (60)	41.74 (54)	43.47 (40)
Al_2O_3	41.15 (73)	42.01 (81)	39.31 (33)
MgO	0.67 (23)	0.45 (4)	1.16 (8)
CaO	0.50 (19)	0.31 (2)	1.07 (6)
MnO	0.34 (18)	0.02 (2)	0.04 (1)
FeO	0.25 (3)	0.50 (9)	1.00 (16)
Li_2O*	1.61 (2)	1.62 (0)	1.63 (1)
Na_2O	N.D.	N.D.	N.D.
K_2O	0.09 (6)	0.02 (1)	0.05 (3)
F	0.36 (36)	0.11 (6)	0.18 (4)
H_2O*	9.56 (28)	9.69 (1)	9.72 (6)
O=F	0.15 (15)	0.05 (3)	0.08 (2)
Total	96.51	96.41	97.54
Cookeite layer			
Si	3.00	3.00	3.00
Al(IV)	1.00	1.00	1.00
Al(VIII)	2.00	2.00	2.00
Al(VIII)	2.00	2.00	2.00
Li	1.00	1.00	1.00
F	0.09	0.03	0.04
OH	1.91	1.97	1.96
OH	6.00	6.00	6.00
Smectite layer			
Si	3.49 (6)	3.42 (10)	3.65 (3)
Al(IV)	0.51 (6)	0.58 (10)	0.35 (3)
Al(Sm)	1.96 (4)	2.04 (3)	1.73 (3)
Mg	0.15 (5)	0.10 (1)	0.26 (2)
Mn	0.04 (2)	0.00 (0)	0.01 (0)
Fe	0.03 (0)	0.06 (1)	0.13 (2)
Ca	0.08 (3)	0.05 (0)	0.17 (1)
K	0.02 (1)	0.00 (0)	0.01 (1)
F	0.09 (9)	0.03 (1)	0.04 (1)
OH	1.91	1.97	1.96

* Li_2O and H_2O contents were calculated by stoichiometry.
Cations in cookeite layer were estimated as ideal chemical composition.

For XRD experiments of cookeite, Li tosudite, and montmorillonite-beidellite, there was difference of the *d* value and full-width at half maximum (FWHM) corresponding to the structure and chemical composition (Fig. 48). The FWHM of cookeite was small and constant, while Li tosudite and beidellite-montmorillonite had larger FWHM. This is derived from the crystallinity and ordering. The 001 value of cookeite was 14.0-14.2 Å, and the 002 value of Li tosudite was 14.1-14.5 Å (001 value was 28.2-29.0 Å) (Fig. 48a). The 001 value of beidellite and montmorillonite was 14.6-15.1 Å, and K-rich K beidellite was 11.6-12.0 Å. The small basal reflection peak of K beidellite is caused by suitability of K^+ for six-membered ring structure working on interlayer to close. However, the 11.6-12.0 Å is also considered as 003 reflection of 35 Å period of IIS (illite/smectite mixed layer mineral, R = 2). The *d* values of 060, generally indicating octahedral composition, increase with Mg contents in octahedral cites (Fig. 48b).

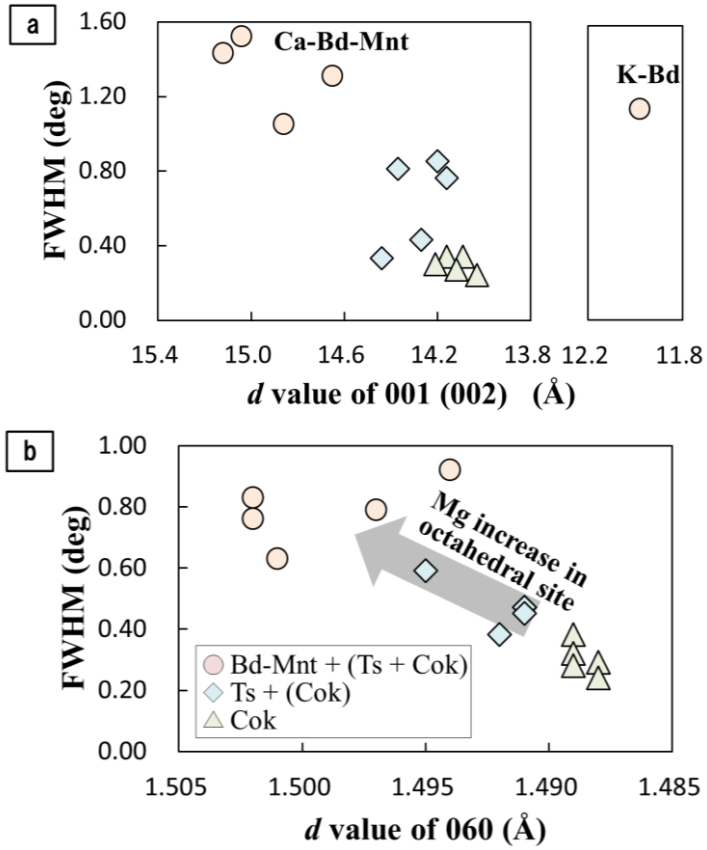

Fig. 48 Peak properties of beidelite-montmorillonite, Li tosudite and cookeite by XRD experiments. (a) *d* value of 001 (or 002) and full-width half maximum (FWHM). (b) *d* value of 060 and FWHM.

Table 11. 001, 060 reflections and the FWHM values with the chemical properties in specimens used in Figure 48.

Specimen No.		001	FWHM	060	FWHM	Clay mineral	Origin	Mg	Fe	Mn	$\Sigma_{Mg+Fe+Mn}$	Al(IV)
Ng132	Cloudy	11.98	1.15	1.502	0.83	Bd+(Ts+Cok)	Kfs	0.24	0.04	0.02	0.30	0.49
Ng146	White	14.86	1.05	1.502	0.76	Mnt	Ptl?	0.32	0.03	0.10	0.45	0.24
Ng130	Red	14.65	1.31	1.501	0.63	Mnt	Ptl?Kfs?Ab?					
XN351	Red	15.12	1.43	1.497	0.79	Mnt	Ptl					
XN351	White	15.04	1.52	1.494	0.92	Mnt	Ptl					
XN350	Red	14.06	0.61	1.488	0.68	Cok+(Mnt?)	Ptl					
Ng145	Grenn	14.37	0.81	1.495	0.59	Ts?	?					
Ng134	Light blue	14.44	0.33	1.492	0.38	Cok+Ts	Kfs	0.13	0.07	0.01	0.20	0.68
Ng132	Tanscelucent	14.27	0.43	1.491	0.47	Cok+(Ts)	Kfs	0.08	0.02	0.02	0.11	0.76
Ng142	Inner	14.20	0.85	1.491	0.47	Cok+Ts?	?					
Ng136	Light blue	14.16	0.76	1.491	0.45	Ts+Cok	Kfs					
Ng139	White	14.16	0.34	1.489	0.38	Cok	Kfs	0.00	0.00	0.00	0.00	0.76
Ng132	Spherical	14.09	0.34	1.489	0.32	Cok	Kfs	0.00	0.00	0.00	0.00	0.76
Ng112	Spherical	14.03	0.24	1.489	0.28	Cok	Kfs	0.00	0.00	0.00	0.00	0.79
Ng142	Pink	14.12	0.27	1.488	0.29	Cok	?					
Ng134	White	14.21	0.30	1.488	0.24	Cok	Kfs	0.00	0.00	0.00	0.00	0.71
XN350	Pink vein in Ptl	14.00	0.40	1.488	0.56	Cok	Ptl					

The TEM observations of K beidellite with Li tosudite, cookeite, and quartz revealed their microtextures (Fig. 49). K beidellite forms aggregates were composed of a few platy grains (1 μm in width and 200 nm in thickness) in a similar shape to montmorillonite observed by SEM (Figs. 49b, 49c, 40b). The basal distance was 10.9 Å, shrinking in vacuum, with frequent stacking faults (Fig. 49d). Li tosudite aggregates consisted of platy grains (1 μm in width and 200 nm in thickness) (Figs. 49a, e). The long period reflection of 25 Å was confirmed. The HRTEM images show that there are cookeite rich layer and smectite rich layer in Li tosudite (Figs, 50, 51).

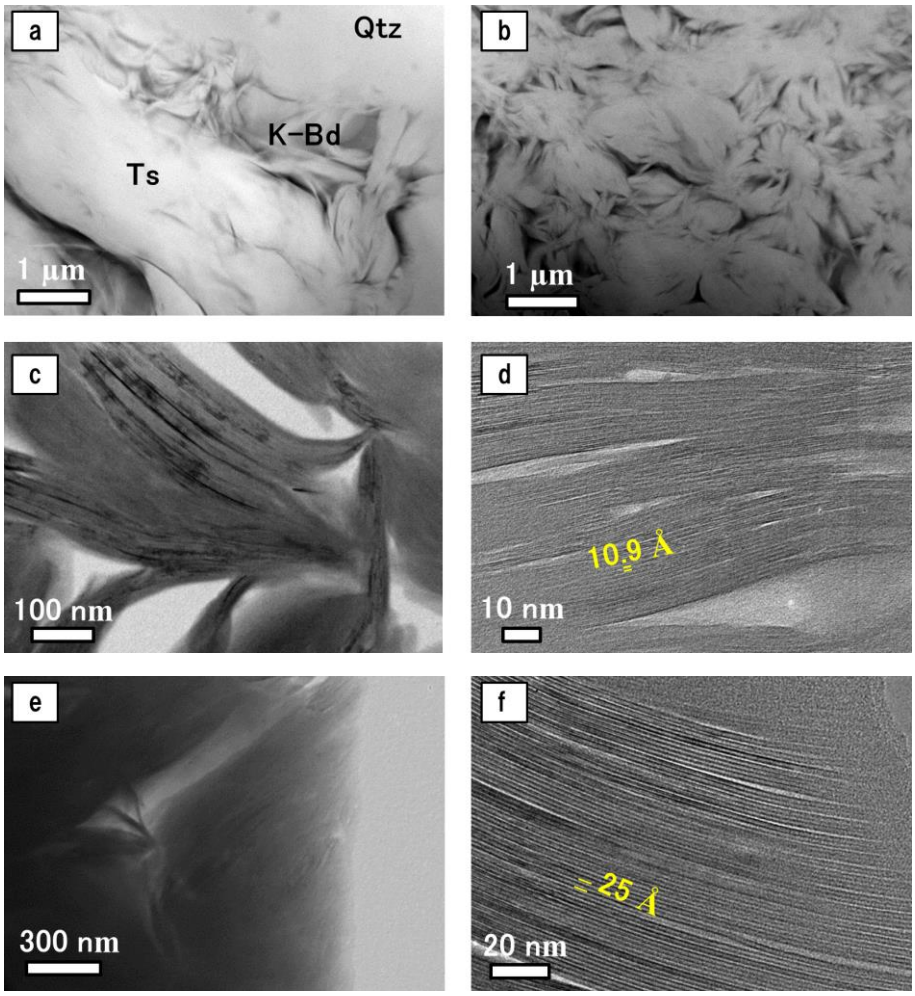

Fig. 49 Microtextures of K beidellite (Ng132). (a) STEM HAADF image of K beidellite with Li tosudite and quartz. (b) STEM HAADF image of K beidellite. (c) TEM image of K beidellite. (d) HRTEM image of K beidellite. The basal layer distance was 10.9 Å. (e) TEM image of Li tosudite. (f) HRTEM image of Li tosudite. The basal layer distance was 25 Å.

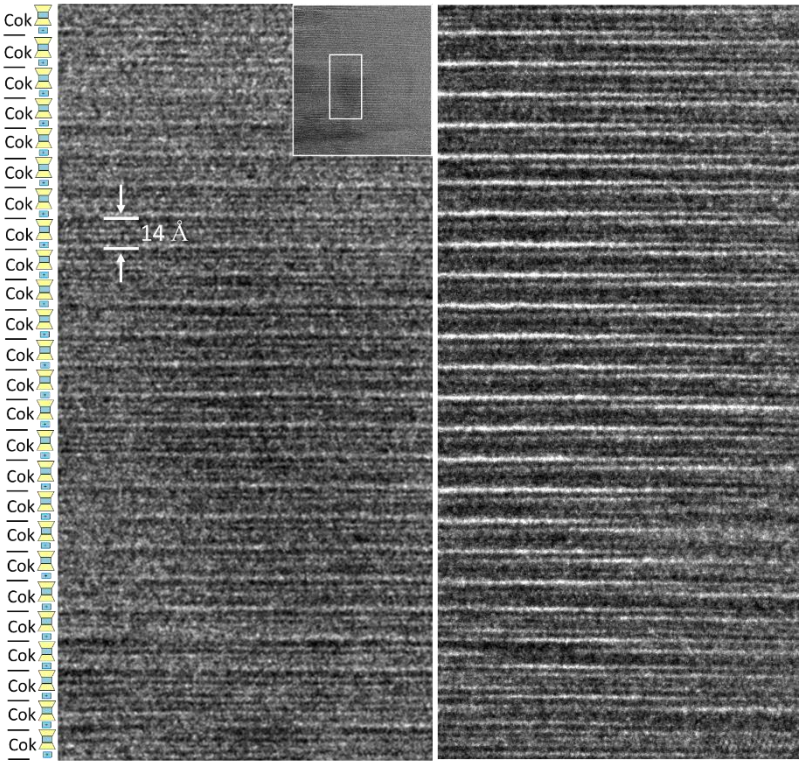

Fig. 50 HRTEM image of cookeite (left) and the defocused image of same area (right).

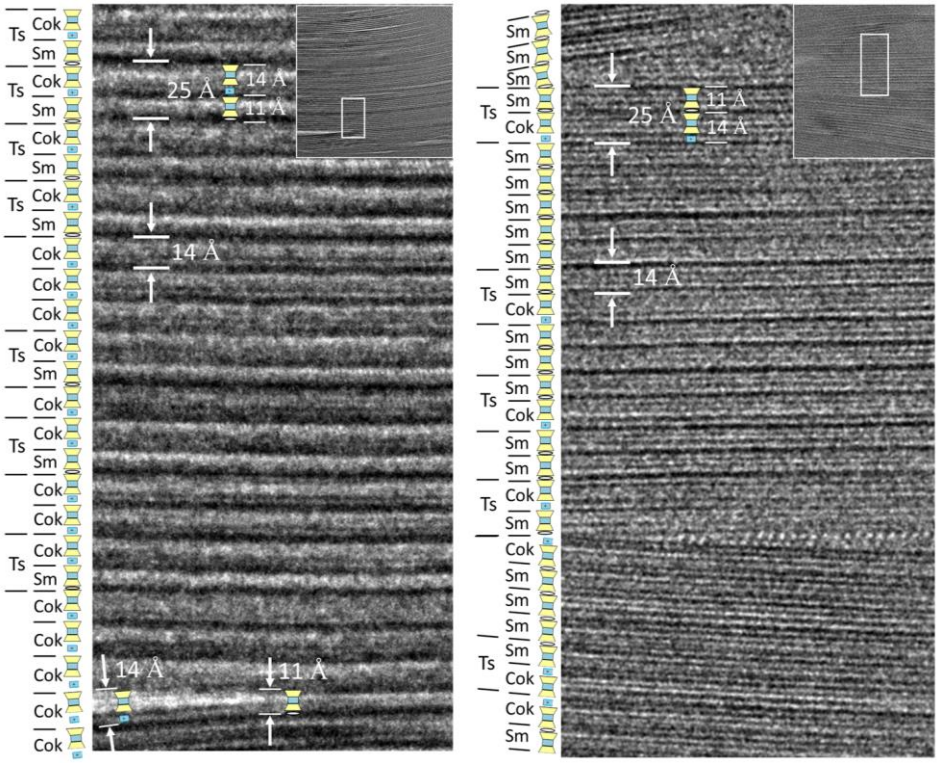

Fig. 51 HRTEM images of Li tosudite in cookeite layer rich area (left) and smectite rich are (right).

The clay minerals after primary minerals from the Nagatare Li pegmatite are generally associated with black Mn aggregates or dendrites (*e.g.*, Figs. 24, 39). The most of them were identified as lithiophorite, $(LiAl_2)(Mn^{4+}{}_2Mn^{3+})O_6(OH)_6$, by XRD, EPMA, and TEM/STEM (Fig. 52). The lithiophorite sometimes associate todorokite. The occurrence of lithiophorite as Mn oxide deposition indicates that all of Li released from dissolution of Li minerals was not escaped from pegmatite; a part of Li is deposited as Mn oxide at late hydrothermal stage. Lithiophorite has similar octahedral layer composed of $LiAl_2(OH)_6$ as cookeite (Fig. 53). The study of their stability and crystallographic property is required to reveal their behaviors.

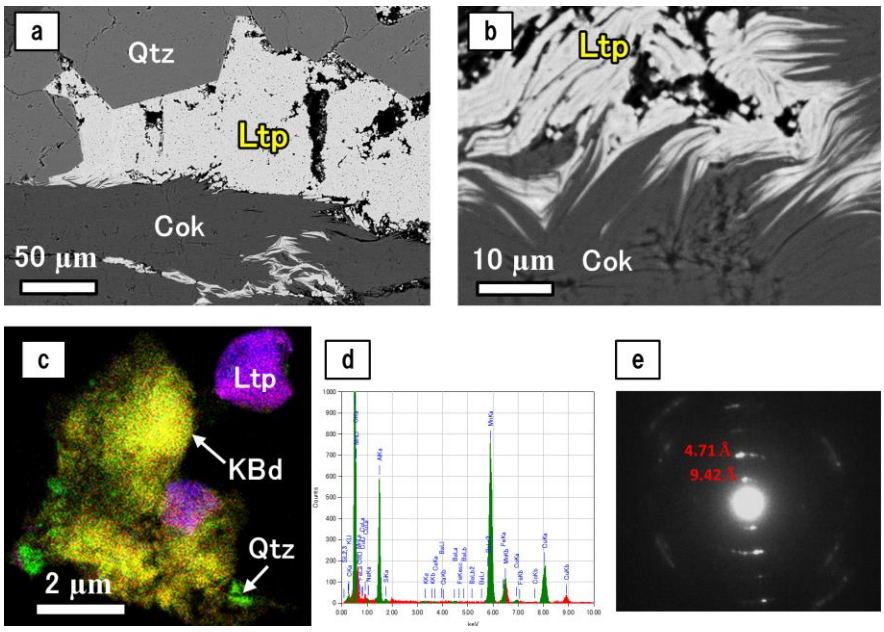

Fig. 52 BSE images and TEM/STEM analyses of lithiophorite. (a) BSE image of lithiophorite on cookeite and quartz (Ng111). (b) Fine grained lithiophorite, showing platy signature. (c) Overlay X-ray map image of lithiophorite (XN350). Red: Al *K*α, green: Si *K*α, blue: Mn *K*α. (d) Energy spectrum of lithiophorite in Figure 52c. (e) SAED pattern of lithiophorite in Figure 52c.

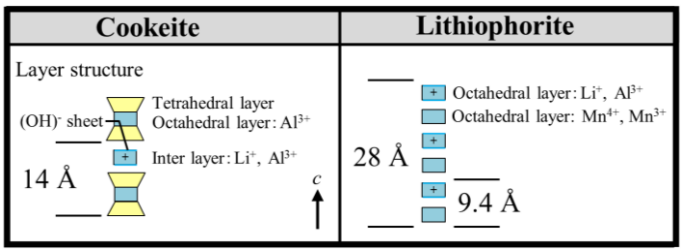

Fig. 53 Layer structure of cookeite and lithiophorite. The chemical composition and crystal structure are referenced by Post & Appleman (1994).

6.3 Hydrothermal alteration process

In the Nagatare pegmatite, primary K-feldspar, petalite, Li tourmaline, and the montebrasite-amblygonite series from Li rich part, were altered to clay minerals along the fractures. K-feldspar was replaced by cookeite, muscovite, and quartz, or minor Li tosudite, K beidellite, and quartz. Petalite was mainly altered to montmorillonite, beidellite and quartz. Li tourmaline had alterations by muscovite and minor cookeite. The montebrasite-amblygonite series was partially altered to various phosphates and muscovite. The detailed properties of each clay mineral formed in alteration are summarized in Figure 54. For their morphological properties, cookeite occurred as spherical aggregates in most cases. This is considered as the result of nucleation and growth in open space after the dissolution of K-feldspar. The green spherical muscovite is formed in a similar way. In addition, the curved shapes of cookeite, Li tosudite, and beidellite-montmorillonite are derived from their stacking disorder structure.

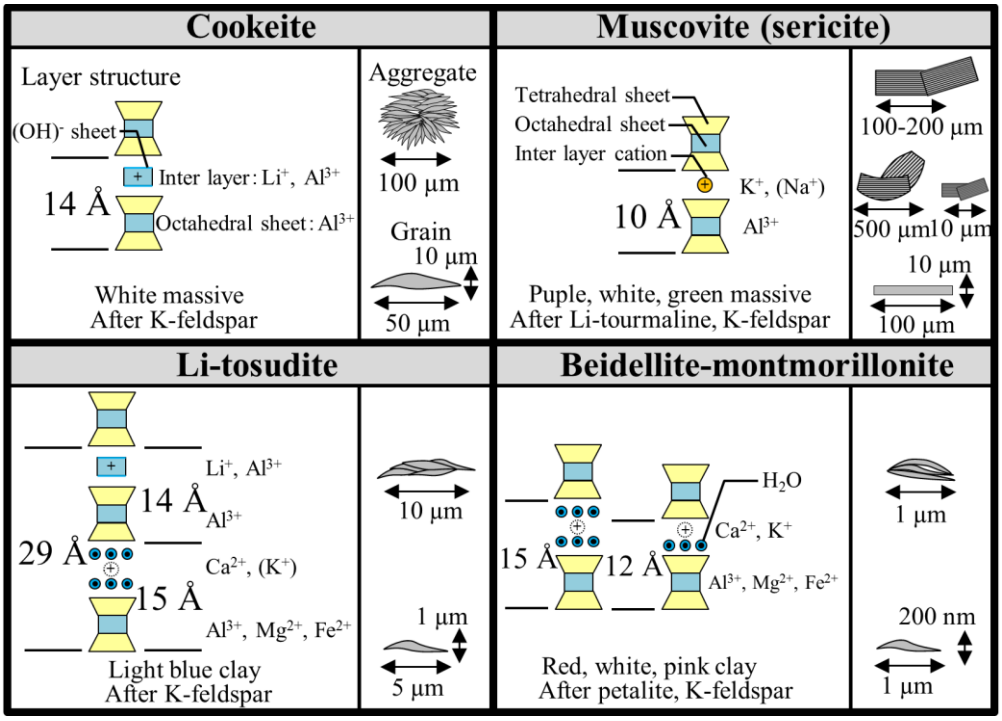

Fig. 54 Detailed mineralogical properties of clay minerals formed by alteration of primary minerals from the Nagatare pegmatite.

As contrasted to cookeite and muscovite, the aggregates of Li tosudite and beidellite-montmorillonite were extremely small, composed of a few grains. The low layer charge of smectite layer causes fine grained structures of Li tosudite and beidellite-montmorillonite consisted of only a few piled platy grains. In any case, primary minerals were altered along the fractures at the early stage. When the reacted fluids are sufficient to rocks, they are completely broken down. The supplied fluid contents are changed at the later stage with transition to an open system. It is supported by the associated texture of veinlet and massive clays. Partially altered Li tourmaline, petalite, and the montebrasite-amblygonite series had inhomogeneous alteration texture even single crystals, which indicates that the alteration process is strongly controlled by water/rock ratio, and permeability. As for K-feldspar, however, there are two cases of highly or no alteration. In other words, K-feldspar with minor veinlet clays as other partially altered minerals was not observed in the Nagatare Li pegmatite. In the case of tourmaline, it has a selectable alteration corresponding to the various chemical compositions, and only Al and OH rich Li tourmaline is suffered alteration. In a similar way, there is a possibility that the selectable alteration occurred corresponding to the chemical composition, crystal structure, or internal texture of K-feldspar.

Based on the mineralogical property of clay minerals and their microtextures, the alteration process of petalite, K-feldspar, Li tourmaline, and the montebrasite-amblygonite series is summarized in Figure 55. With decreasing temperature, Li chloritization, sericitization, and smectitization had occurred at a hydrothermal stage in the Nagatare Li pegmatite. In weakly acidic condition, K-feldspar breaks down with formation of cookeite + quartz releasing K^+ to fluid. The transition to neutral condition from weakly acidic makes Li tourmaline unstable and sericitization. At the late stage, additional alteration occurs by inflow of external fluids, and petalite is unstable in the weakly acidic conditions with low Li^+ and K^+ activity at low

temperature. Finally, Li and B released from minerals escape from the pegmatite rock with the reaction fluids, while a part of released Li precipitated as lithiophorite on the surface of pegmatite minerals. In the southwest part of Mt. Nagatare, the host granite has hydrothermal alteration, and it is related to later alteration of the Nagatare pegmatite (Fig. 56).

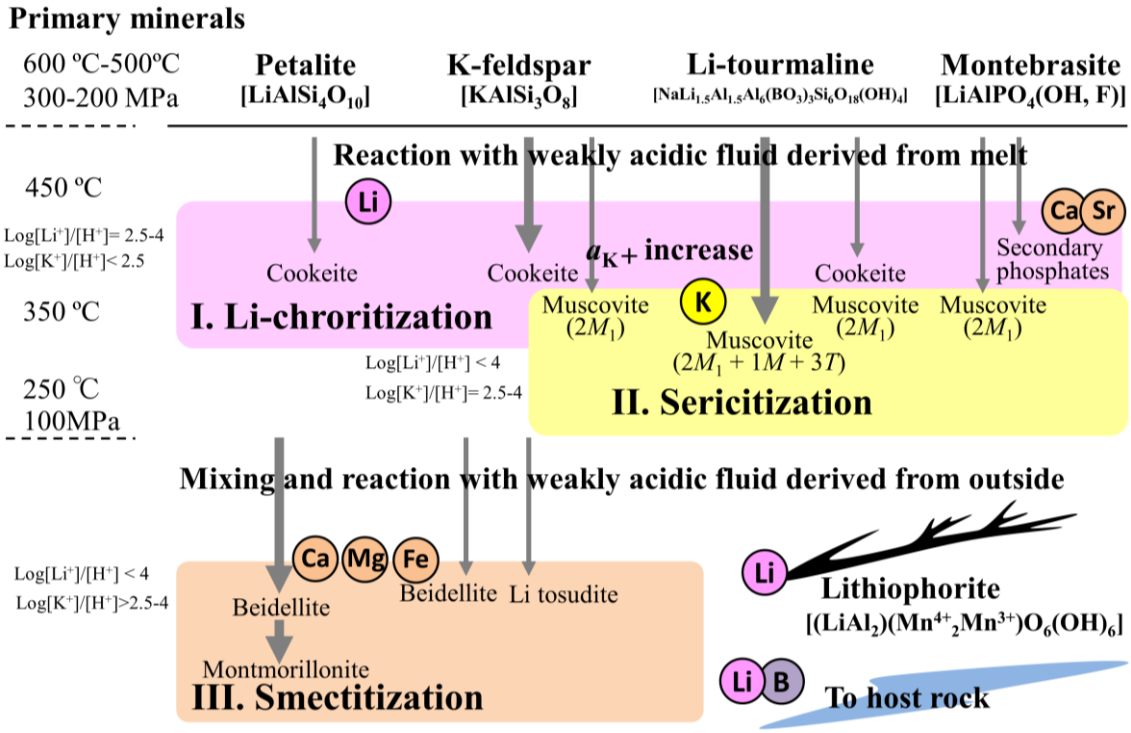

Fig. 55 Hydrothermal alteration process of petalite, K-feldspar, Li tourmaline, and the montebrasite-amblygonite series from the Nagatare pegmatite.

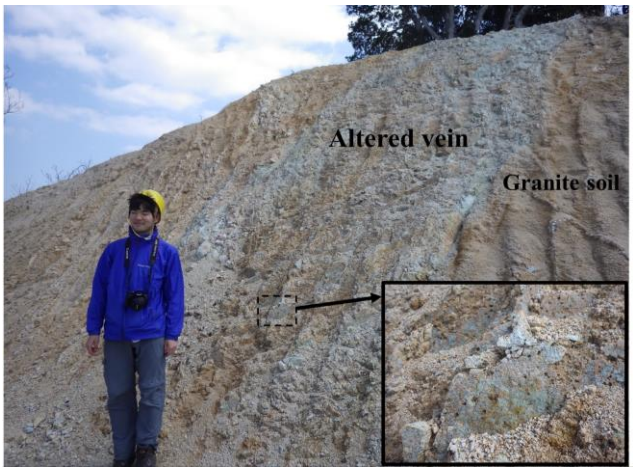

Fig. 56 Hydrothermal vein in host granite with ordinal granite texture from the southwest part of Mt. Nagatare. The veins are enriched in clays and vugs associated with quartz and pyrite.

Mineral paragenesis and alteration texture lead a restriction of Li pegmatite formation conditions. Figure 57 shows the pressure-temperature path of pegmatites from magmatic to hydrothermal conditions. In the case of Tanco pegmatite, Canada, the P-T path was indicated by London (2008), based on occurrence of petalite, spodumene-quartz intergrowth, and eucryptite-quartz intergrowth, and estimated by the conditions of fluid-inclusion entrapment (Fig. 57). Though similar cooling history was expected for the Nagatare pegmatite, the occurrence of petalite without spodumene and eucryptite indicates that the Nagatare pegmatite follow different path, i.e. with lower pressure or different chemical condition.

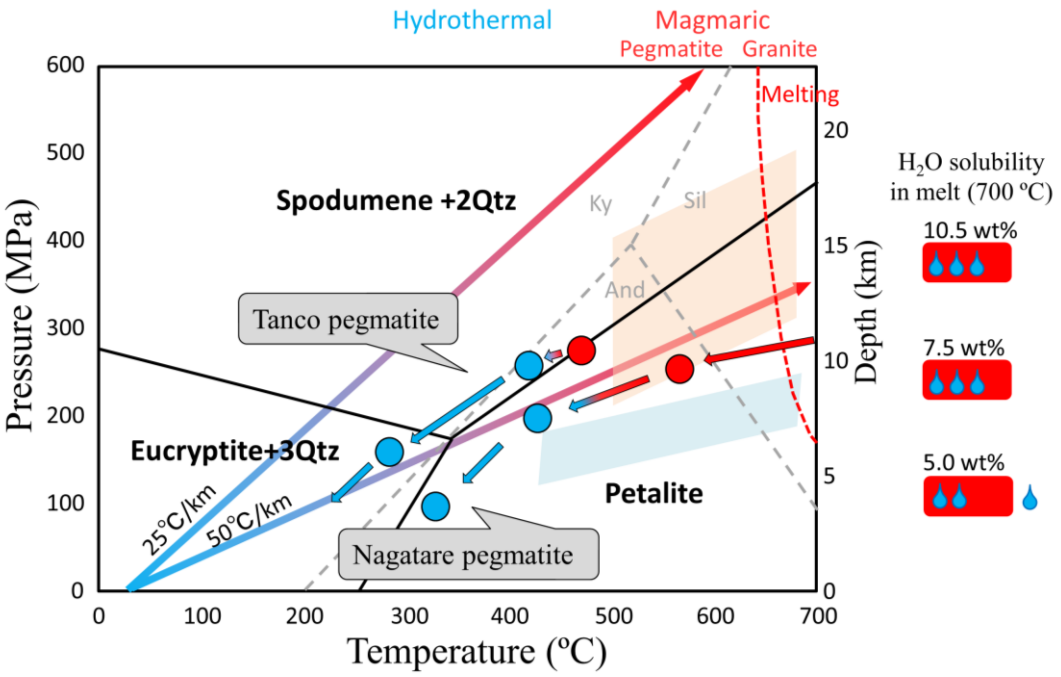

Fig. 57 Pressure-temperature path of pegmatites under the hydrothermal alteration conditions. Stability diagrams in quartz saturated condition were calculated using standard state thermodynamic properties from Vidal & Goffé (1991) and Holland & Powell (1998). The minimum-melting curve of haprogranite in the presence of brines on X_{H_2O} = 1.0 is taken from Aranovich *et al*. (2013). The P-T path of Tanco pegmatite were referenced from London (2008). Thermal gradient and depth are estimated as continental crust (ρ = 2700 kg/m^3). The general P-T range of rare element type and miarolitic type pegmatite are shown as orange and light blue color zones based on Černý (1991). H_2O solubility in a silicate melt was calculated by VolatileCalc (Newman & Lowenstern 2002).

For comparison, the diagrams of log (a_{Li+}/a_{H+}) vs. log (a_{K+}/a_{H+}) corresponding to their P-T condition were calculated (Figs. 58, 59). Li chloritization occurs in the condition of log (a_{Li+}/a_{H+}) = 2.5-4.0 and log (a_{K+}/a_{H+}) < 2.5 at 100-200 MPa and 325-425 °C, and the non-equilibrated reactions leads increase of log (a_{K+}/a_{H+}). The solution composition changes from cookeite stable area to muscovite stable area with increase of log (a_{K+}/a_{H+}). The mixture of cookeite and muscovite after Li tourmaline is the evidence that solution composition stayed at equilibrated area of muscovite and cookeite. Sericitization occurs in the condition of log (a_{Li+}/a_{H+}) < 4.0 and log (a_{K+}/a_{H+}) = 2.5-4.0 at 100-200 MPa and 225-425 °C. Under 100 MPa and 225 °C, solution composition bears in smectite stable area, which is not shown in figure and located between kaolinite and muscovite stable area.

In vein type pegmatite such as Nagatare pegmatite, hydrothermal alterations occur with exsolution of water from hydrosilicate melt, while pegmatites with cavity generally have pocket clays. The pocket formation processes are considered as low pressure and temperature conditions, and “dry” (open-space) cavities are also originally filled by dense clays than water fluids (London 2014). Foord *et al*. (1986) reported the occurrence of cookeite, Li tosudite, and smectite as pocket clays in cavities of complex granitic pegmatites from San Diego County. The occurrence of cookeite as alteration product and pocket clay indicates that hydrothermal fluid containing Li exsolves from hydrosilicate melt in any case. The pocket clays are statically formed on crystals in cavity, while hydrothermal alteration dynamically occurs along fracture of minerals with non-equilibrium reactions.

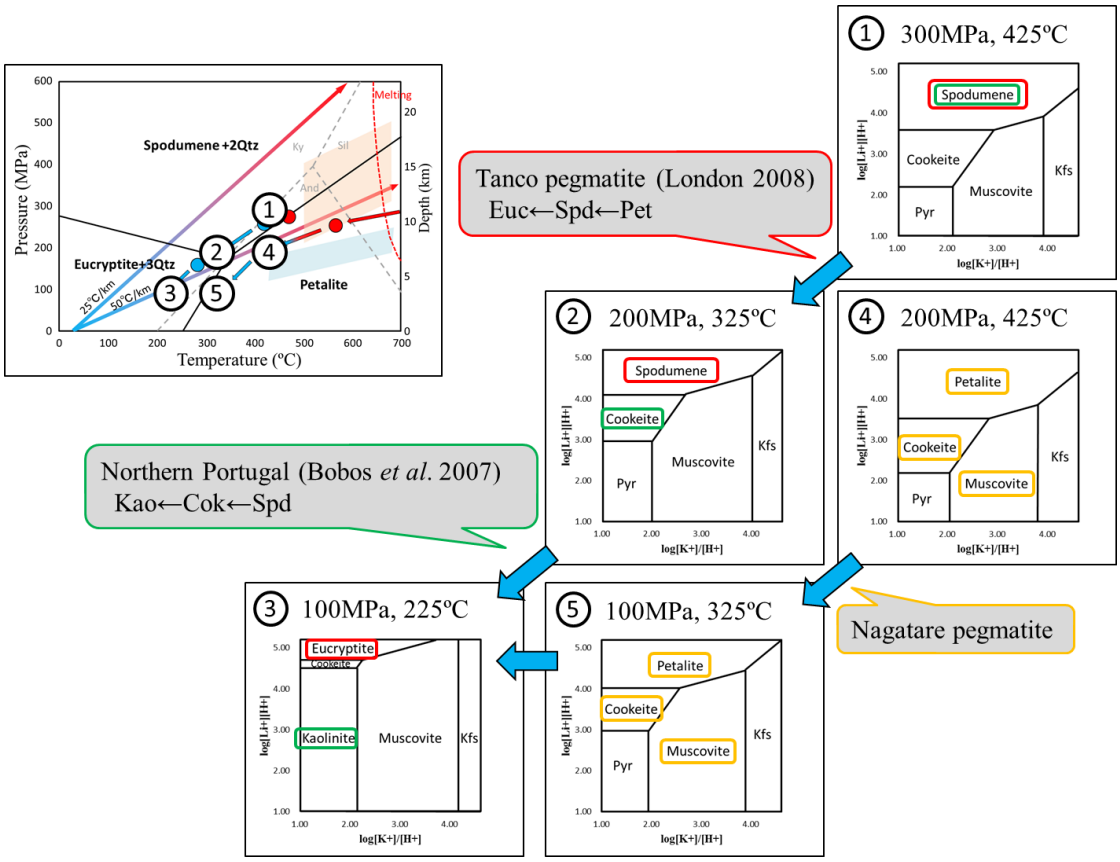

Fig. 58 The diagrams of log (a_{Li+}/a_{H+}) *vs*. log (a_{K+}/a_{H+}), corresponding to the P-T condition of Figure 57. They were calculated using standard state thermodynamic properties from Vidal & Goffé (1991), Holland & Powell (1998), Robie *et al*. (1978), Zotov *et al*. (1998), and Schock *et al*. (1997). Kfs: K-feldspar, Pyr: pyrophyllite.

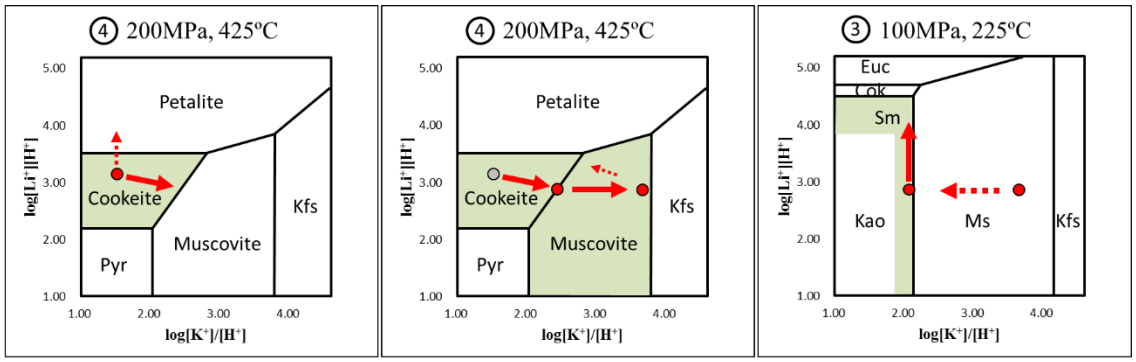

Fig. 59 The diagrams of log (a_{Li+}/a_{H+}) *vs*. log (a_{K+}/a_{H+}). The red arrows show the change direction of solution composition caused by alteration of primary minerals. At 200 MPa and 425 °C, the solution composition changes from cookeite stable area to muscovite stable area with increase of log (a_{K+}/a_{H+}). Under 100 MPa and 225 °C, the solution composition bears in smectite stable area, which is not shown in figure and located between kaolinite and muscovite stable area.

CONCLUSION

The montebrasite–amblygonite series and lacroixite from the Nagatare Li pegmatite had complex microtexture, which was scattered patch or lamella of lacroixite in the montebrasite–amblygonite series like “natromontebrasite” in all specimens. The patch texture was composed of lacroixite and low fluorine contents montebrasite with same crystal orientations to host montebrasite. This texture is a result of an exsolution from high-temperature phase.

The montebrasite–amblygonite series from high temperature Li pegmatite with only petalite as Li-aluminosilicate phase had low to high lacroixite contents, and the montebrasite–amblygonite series from lower temperature Li pegmatite with spodumene had no or low lacroixite contents. Gem-quality montebrasite from drusy vugs formed at low temperature had no exsolution texture or lacroixite. Investigating microtextures of the montebrasite–amblygonite series provides information of thermal and chemical conditions at pegmatite formation. Synthetic experiment of the montebrasite-amblygonite series is required for more quantitative approach.

K-feldspar, petalite, Li tourmaline, and the montebrasite-amblygonite series from the Nagatare pegmatite were partially or perfectly altered to clay minerals such as cookeite, muscovite, Li tosudite, and beidellite-montmorillonite. With decreasing temperature, Li chloritization, sericitization, and smectitization had occurred in the Li rich part of the Nagatare Li pegmatite. In weakly acidic condition, K-feldspar had breakdown, forming cookeite + quartz with releasing K^+ to a hydrothermal fluid. As a result of the change from weakly acidic to neutral condition, Li tourmaline had breakdown, and suffered sericitization. It is estimated that Li and B escaped from pegmatite body with reaction fluids at last, while a part of released Li was precipitated as lithiophorite on the surface of pegmatite minerals.

In Li pegmatites, residual fluids containing Li react with primary minerals in subsolidus conditions, and they make cation exchanges between fluids and solids. The changes of fluid compositions with non-equilibrium reactions and a decrease of temperature controlled hydrothermal alterations in Li pegmatites. Li pegmatites with no druse as the Nagatare Li pegmatite have similarity of clay minerals to Li pegmatites with druse except for alteration of primary minerals. More detailed studies of clay minerals in pegmatites including pegmatites with druse are required. selectable alteration

ACKNOWLEDGEMENTS

The author thanks Dr. Seiichiro Uehara, Assistant Professor of Department of Earth and Planetary Sciences, Faculty of Sciences, Kyushu University, for many instructions and suggestions. The author wish to acknowledgements Dr. Tomoaki Kubo, Associate Professor, and Dr. Takumi Kato, Professor of Department of Earth and Planetary Sciences, Faculty of Sciences, Kyushu University, for many advices. The author is deeply thankful to Dr. Masanori Kurosawa, Associate Professor of Graduate school of Life and Environmental Sciences, Tsukuba University, and Dr. Takeshi Ikeda, Associate Professor of Department of Earth and Planetary Sciences, Faculty of Sciences, Kyushu University, for their constructive and critical comments as Advisory Committee of Front Researcher Program. We appreciate Mr. Kazuhiro Hamasaki and Mr. Kenichi Miyazaki for supplying samples. We thank Engineering Specialist Mr. Kazuhiro Shimada and Assistant Professor Dr. Tomoharu Miyamoto, Department of Earth and Planetary Sciences, Faculty of Sciences, Kyushu University, for technical support with chemical analyses. This work was supported by JSPS KAKENHI Grant Number 6003404. The author thanks the Professor Matsumoto Scholarship Fund.

The special acknowledgement is made to members in the research group of Earth and Planetary Material Sciences Laboratory, and office members in Department of Earth and Planetary Sciences, Faculty of Sciences, Kyushu University, for personal support and encouragement.

REFERENCES

AHN, J.H. & BUSECK, P.R. (1998) Transmission electron microscopy of muscovite alteration of tourmaline. *American Mineralogist* **83**, 535-541.

ARANOVICH, L.Y., NEWTON, R.C. & MANNING C.E. (2013) Brine-assisted anatexis: Experimental melting in the system haplogranite–H_2O–NaCl–KCl at deep-crustal conditions. *Earth and Planetary Science Letters* **374**, 111-120.

BALDWIN, J.R., HILL, P.G., VON KNORRING, O. & OLIVER, G.J.H. (2000) Exotic aluminium phosphates, natromontebrasite, brazilianite, goyazite, gorceixite and crandallite from rare-element pegmatites in Namibia. *Mineralogical Magazine* **64**, 1147–1164.

BANNO, Y., BUNNO, M., HARUNA, M. & OBA, M. (2001) Stibiotantalite-group minerals in a lithium pegmatite from Nagatare, Fukuoka Prefecture, Japan. *Journal of Mineralogical Sciences* **96**, 205-209.

BOBOS, I., VIEILLARD, P., CHAROY, B. & NORONHA, F. (2007) Alteration of spodumene to cookeite and its pressure and temperature stability conditions in Li-bearing aplite-pegmatites from Northern Portugal. *Clays and Clay Minerals* **55**, 295-310

CAMERON, E.N., JAHNS, R.H., MCNAIR, A.H. & PAGE, L.R. (1949) Internal structure of granitic pegmatites. *Economic Geology Monograph* **2**, 115pp.

ČERNÁ, I., ČERNÝ, P. & FERGUSON, R.B. (1973) The fluorine content and some physical properties of the amblygonite–montebrasite minerals. *American Mineralogist* **58**, 291–301.

ČERNÝ, P. (1991) Rare-element granitic pegmatites. Part I: Anatomy and internal evolution of pegmatite deposits. *Geoscience Canada* **18**, 49-67.

ČERNÝ, P. & ERCIT, T.S. (2005) The classification of granitic pegmatites revisited. *Canadian Mineralogist* **43**, 2005–2026.

CHRISTIDIS, G.E. (1997) Compositional variations in smectites. Part II: alteration of acidic precusors, a case study from Milos Island, Greece. *Clay Minerals* **32**, 23-270.

FOORD, E.E., SRARKEY, H.C. AND TAGGART, J.E.JR. (1986) Mineralogy and paragenesis of "pocket" clays and associated in complex granitic pegmatites, San Diego County, California. *American Mineralogist* **71**, 428-439.

FRANSOLET, A.–M. (1989) The problem of Na–Li substitution in primary Li–Al phosphates: new data on lacroixite, a relatively widespread mineral. *Canadian Mineralogist* **27**, 211–217.

FRANSOLET, A.–M., FONTAN, F. & DE PARSEVAL, P. (2007) Natromontebrasite, a discredited mineral species. *Canadian Mineralogist* **45**, 391–396.

GALLISKI, M.Á., ČERNÝ, P., MÁRQUEZ–ZAVALÍA, M.F. & CHAPMAN, R. (2012) An association of secondary Al–Li–Be–Ca–Sr phosphates in the San Elías pegmatite, San Luis, Argentina. *Canadian Mineralogist* **50**, 933–942.

GEOLOGICAL SURVEY OF JAPAN (1977) Radiometric age map of Japan 1) Granitic rocks, 1:2000000 map series 16-1.

GREINER, D.J. & BLOSS, F.D. (1987) Amblygonite–montebrasite optics: Response to (OH^-) orientation and rapid estimation of F from 2*V*. *American Mineralogist* **72**, 617–624.

GROAT, L.A., CHAKOUMAKOS, B.C., BROUWER, D.H., HOFFMAN, C.M., FYFE, C.A., MORELL, H. & SCHULTZ, A.J. (2003) The amblygonite ($LiAlPO_4F$) –montebrasite ($LiAlPO_4OH$) solid solution: A combined powder and single-crystal neutron diffraction and solid-state 6Li MAS, CP MAS, and REDOR NMR study. *American Mineralogist* **88**, 195–210.

GROAT, L.A., RAUDSEPP, M., HAWTHORNE, F.C., ERCIT, T.S., SHERRIFF, B.L. & HARTMAN, J.S. (1990) The amblygonite–montebrasite series: Characterization by single-crystal structure refinement, infrared spectroscopy, and multinuclear MAS–NMR spectroscopy. *American*

Mineralogist **75**, 992–1008.

GÜVEN, N. & BURNHAM, W. (1967) The crystal structure of 3*T* muscovite. *Zeitschrift für Kristallographie Bd* **125**, 163-183.

GÜVEN, N. (1988) Smectite. Hydrous Phyllosilicates (S.W. Bailey, editor) 497-559. *Reviews in Mineralogy* **19**. Mineralogical Society of America.

HOLLAND, T.J.B. & POWELL, R. (1998) An internally consistent thermodynamic data set for phases of petrological interest. *Journal of Metamorphic Geology* **16**, 309-343.

ISHIHARA, S. (1977) The magnetite-series and ilmenite-series granitic rocks. *Mining Geology* **27**, 293-305.

JAHNS, R.H. & BURHAM, C.W. (1969) Experimental studies of pegmatite genesis: I. A model for the derivation and crystallization of granitic pegmatites. *Economic Geology* **64**, 83-864.

KALLIO, P. (1978) A new X-ray method for the estimation of fluorine content in montebrasites. *American Mineralogist* **63**, 1249–1251.

KARAKIDA, Y. (1985) Geological classification of granitic rocks in North Kyushu region. Japan *Society of Engineering Geology Kyushu Branch report* **9**, 99-104 (in Japanese).

KARAKIDA, Y., TOMITA, S., SHIMOYAMA, S. & CHIJIWA, K. (1994) *Geology of the Fukuoka district, Geological Sheet Map 1:50,000, Fukuoka (14) No. 51.* Geological Survey of Japan, Tokyo, 192 pp. (in Japanese with English abstract).

KATAOKA, Y. & UEHARA, S. (2000) Lepidolite in a lithium pegmatite from Nagatare, Fukuoka Prefecture, Japan. *Abstract of 2000 Annual Meeting of the Mineralogical Society of Japan*, 101 (in Japanese).

KO, S. (1933) Pegmatite dykes from Nagatare: Lepidolite and “ceylonite”. *Our minerals* **2**, 1-3 (in Japanese).

KUBO, K., MATSUURA, H., OZAKI, M., MAKIMOTO, H., HOSHIZUMI, H. & KAMATA, K. (1993)

Geological Map of Japan 1:200,000, Fukuoka. Geological Survey of Japan.

LIANG, J-J. & HAWTHORNE, F.C. (1996) Rietveld refinement of micaceous materials; muscovite-2M 1, a comparison with single-crystal structure refinement. *Canadian Mineralogist* **34**, 115-122.

LONDON, D. (1984) Experimental phase equilibria in the system $LiAlSiO_4$–SiO_2–H_2O: a petrogenetic grid for lithium-rich pegmatites. *American Mineralogist* **69**, 995–1004.

LONDON, D. (2008) Pegmatites. The Canadian Mineralogist Special Publication 10, pp. 368.

LONDON, D. (2009) The origin of primary textures in granitic pegmatites. *Canadian Mineralogist* **47**, 697-724.

LONDON, D. (2014) A petrologic assessment of internal zonation in granitic pegmatites. *Lithios* **184-187**, 74-104.

LONDON, D. & BURT, D.M. (1982) Alteration of spodumene, montebrasite and lithiophilite in pegmatites of the White Picacho District, Arizona. *American Mineralogist* **67**, 97–113.

LONDON, D. & MORGAN VI, G.B. (2012) The pegmatite puzzle. *Elements* **8**, 263-268.

LONDON, D., MORGAN, G.B.VI. & WOLF, M.B. (2001) Amblygonite–montebrasite solid solution as monitors of fluorine in evolved granitic and pegmatite melts. *American Mineralogist* **86**, 225–233.

MATSUBARA & KATO (1980) Pegmatite Phosphates from Yukiiri, Ibaraki Prefecture, Japan. *Journal of the Mineralogical Society of Japan* **14**, 269-289 (in Japanese).

MATSUYAMA, F. & KOBAYASHI, T. (1995) The first occurrence of Mn-bearing olenite in Japan. *Chigakukenkyu* **44**, 39 (in Japanese with English abstract).

NAGASHIMA, O. & NAGASHIMA, K. (1960) Rare earth element minerals from Japan. Working Group for commemorating Mr. O. Nagashima, pp. 463 (In Japanese).

NISHIMURA, Y. (1998) Geotectonic subdivision and areal extent of the Sangun belt, inner zone

of Southwest Japan. *Journal of Metamorphic Geology* **16**, 129-140.

NEWMAN, S. & LOWENSTERN, J.B. (2002) VolatileCalc: a silicate melt-H_2O-CO_2 solution model written in Visual Basic for excel. *Computers and Geosciences* **28**, 597-604.

NORTON, J.J. (1983) Sequence of mineral assemblages in differentiated granitic pegmatites. *Economic Geology* **78**, 854-874.

OKAMOTO, Y. (1944) Minerals of Fukuoka Prefecture. Japan hobby group of minerals. pp. 208 (in Japanese).

PAJUNEN, A. & LATHI, S.I. (1985) New data on lacroixite, $NaAlFPO_4$. Part II. Crystal structure. *American Mineralogist* **70**, 849–855.

PLANÇON, A., TSIPURSKI, S.I. & DRITS, V.A. Calculation of intensity distribution in the case of oblique texture electron diffraction. *Journal of Applied Crystallography* **18**, 191-196.

POST, J.E. & APPLEMAN, D.E. (1994) Crystal structure refinement of lithiophorite. *American Mineralogist* **79**, 370-374.

ROBIE, R.A., HEMINGWAY, B.S. & FISHER, J.R. (1978) Thermodynamic properties of minerals and related substances at 298.15 K and 1 bar (10^5 Pascals) pressure and at higher temperatures. United States Geological Survey Bulletin No. 1452, pp. 446.

RONDEAU, B., FRITSCH, E., LEFEVRE, P., GUIRAUD, M., FRANSOLET, A. –M. & LULZAC, Y. (2006) A Raman investigation of the amblygonite-montebrasite series. *Canadian Mineralogist* **44**, 1109–1117.

SAKURAI, K., KATO, A., KUWANO, N. & NAGASHIMA, K. (1972) Chemical studies of minerals containing rarer elements from the far east district. LXV. Pollucite from Nagatare, Fukuoka Prefecture, Japan. *Bulletin of the Chemical Society of Japan* **45**, 812-813.

SAKURAI, K., KATO, A., MIYOKAWA, K. & NAGASHIMA, K. (1973) Chemical studies of minerals containing rarer elements from far east district. LXVI. Cookeite from Nagatare, Fukuoka

Prefecture, Japan. *Bulletin of the Chemical Society of Japan* **46**, 3893.

SCHULTZ, L.G. (1969) Lithium and potassium absorption, dehydroxylation temperature, and structural water content of aluminous smectites. *Clays and Clay Minerals* **17**, 115-149.

SHIROSE, Y., ITO, S. & UEHARA, S. (2015) Rare elements concentration related to behavior of the H_2O, F, B and P, in Nagatare pegmatite, Fukuoka Prefecture. *Abstract of Japan Goscience Union Meeting 2015*, SCG58-P04.

SHIROSE & UEHARA, S. (2012) Comparison of Li-tourmaline composition from Nagatare, Myokenzan, and Okueyama, Japan. *Abstract of 2012 Annual Meeting of the Mineralogical Society of Japan* **48** (in Japanese).

SHIROSE, Y. & UEHARA, S. (2013) Li tourmaline from Nagatare, Fukuoka Prefecture, Japan. *Journal of Mineralogical and Petrological Sciences* **108**, 238–243.

SHIROSE, Y. & UEHARA, S. (2014) Secondary phosphates in montebrasite and amblygonite from Nagatare, Fukuoka Prefecture, Japan. *Journal of Mineralogical and Petrological Sciences* **109**, 103–108.

SHIROSE, Y. & UEHARA, S. (2016) Fine texture of the montebrasite–amblygonite series with lacroixite and their formation process. *Canadian Mineralogist* (*in press*).

SHOCK, E.L., SASSANI, D.C., WILLS, M., & SVERJENSKY, D.A. (1997) Inorganic species in geologic fluids: Correlations among standard molal thermodynamic properties of aqueous ions and hydroxide complexes. *Geochimica et Cosmochimica Acta* **61**, 907-950.

STILLING, A., ČERNÝ, P. & VANSTONE, P.J. (2006) The Tanco pegmatite at Bernic Lake, Manitoba. XVI. Zonal and bulk compositions and their petrogenetic significance. *Canadian Mineralogist* **44**, 599-623.

TAKIMOTO, K. (1937) Geology of Nagatare-Kanatake district, in the suburbs of the city of Fukuoka. *Bulletin of the College of Engineering, Kyushu Imperial University* **12**, 181-197.

UEHARA, S. & SHIROSE, Y. (2013) Namibite and hechtsbergite from the Nagatare mine, Fukuoka Prefecture, Japan. *Mineralogical and Petrological Sciences* **108**, 105–110.

VIDAL, O. & GOFFÉ, B. (1991) Cookeite $LiA1_4(Si_3Al)O_{10}(OH)_8$: Experimental study and thermodynamical analysis of its compatibility relations in the Li_2O-Al_2O_3-SiO_2-H_2O system. *Contributions to Mineralogy and Petrology* **108**, 72-81.

WISE, M.A., FRANCIS, C.A. & ČERNÝ, P. (2012) Compositional and structural variations in columbite-group minerals from granitic pegmatites of the Brunswick and Oxford fields, Maine: Differential trends in F-poor and F-rich environments. *Canadian Mineralogist* **50**, 1515-1530.

ZATOV, A., MUKHAMET-GALEEV, A. & Schott, J. (1998) An experimental study of kaolinite and dickite relative stability at 150–300 °C and the thermodynamic properties of dickite. *American Mineralogist* **83**, 516-524.